ABSTRACT

Title of Dissertation:	Structural Investigation into RioK1 for Cancer Therapeutics
	Daniel Arthur Hunter, Doctor of Philosophy, 2024
Dissertation directed by:	Professor David J. Weber Department of Biochemistry and Molecular Biology

Cancer was the second leading cause of death in the United States in 2020.[1] Cancer shares many similarities with healthy cells, making it a difficult therapeutic target.[2] Current developments of cancer therapeutics are governed by targeting key proteins responsible for distinct features in each type of cancer phenotype. (e.g. decreased apoptosis, metastasis, immortalization, etc.). However, finding a rational therapeutic target, engineering a lead compound, and lead compound optimization is time-consuming and expensive. With the use of high-throughput screens and structure-based drug design it is possible to design lead compounds in a more efficient manner. Techniques such as x-ray crystallography and cryo-electron microscopy are used to observe how compounds interact with the target protein at atomic resolution, which helps facilitate optimization.[2-4] Kinases in particular, have benefitted greatly from these techniques.[5]

Kinases play key roles in signal transduction and its regulation in many cellular pathways. The catalytic active site is highly conserved among many kinase families, so

designing drugs targeting a single enzyme's catalytic site could have potential off target effects as many kinases could be inhibited. Strategies to target kinases therefore use distinct features of each kinase that take both conserved and nonconserved residues into consideration as well as for active and inactive forms of the kinase being targeted, so tailormade therapeutic solutions are derived, as with the case of reading open frame kinase 1 (RioK1).[2, 4, 5] RioK1 was identified as a key enzyme in both lung and colorectal cancer, cancer subtypes with some of the most severe prognoses.[6] In a study done by Kiburu et al., toyocamycin was demonstrated to bind tightly to RioK1 from *archaeoglobus fulgidus* (afRioK1), thereby discovering the first scaffold for RioK1.[7] Toyocamycin is an adenosine analog, commonly used as inhibitor, and thus making this drug scaffold non-specific with off-target effects other than for RioK1.[8-12] To address this issue, computer aided drug design was used to find toyocamycin-like compounds that have improved selectivity for afRioK1 inhibition. A series of these compounds were identified via screening approaches and then co-crystallized with afRioK1 with the goal of elucidating useful structure-activity relationship data for next stage drug-design. Furthermore, one of the most newly studied interactions of RioK1 is with protein arginine methyltransferase type 5 (PRMT5), so understanding the details of this interaction provides yet another means to develop afRioK1 inhibition strategies as part of an approach to block cancer progression.

STRUCTURAL INVESTIGATION INTO RIOK1 FOR CANCER THERAPEUTICS

by

Daniel Arthur Hunter

Dissertation submitted to the Faculty of the Graduate School of the
University of Maryland, College Park, in partial fulfillment
of the requirements for the degree of
Doctor of Philosophy
2024

Advisory Committee
Professor David J. Weber, Chair
Professor Kwaku Dayie
Assistant Professor Jinwoo Lee
Millard and Lee Alexander Professor Pratyush Tiwary
Professor Silvina Matysiak

Acknowledgements

I would like to take the time to acknowledge a few people that helped me throughout my academic journey. I extend my sincere appreciation to Dr. David Weber, the chair of my committee, for his mentorship and welcoming guidance. I am grateful for the ongoing support and patience of my committee members: Dr. Jinwoo Lee, Dr. Kwaku Dayie, Dr. Pratyush Tiwary, and Dr. Silvina Matysiak. I am especially indebted to Dr. Sol Baik for her unwavering support, without which this dissertation would not have come to fruition. Additionally, I extend heartfelt thanks to my parents, Randy and Carmelita Hunter, for fostering my curiosity from a young age and supporting my pursuit of a Ph.D. Their unwavering encouragement has been invaluable. I would like to thank Dr. Nicole LaRonde and fellow colleagues Dr. Nishat Seraj, Dr. Minkyung Kim, Dr. Hongpeng Wang, and Yehnara Ettinoffe, for mentoring me in my early years of the program. Finally, I wish to acknowledge the camaraderie and support provided by Michael & Quynh Capasso, Owen Becette, the Windmill Crew (Kyle Teagarden, Ron Abraham, Jonathan Hampton, Caleb Harris, Shawn Abraham, Tommy Dean, and Rex Davis), the B'more squad (Chen He, Wei Chen, David Porter, Nathan Fenta, Chris Williams, Ngoc Nguyen). Their companionship and shared moments of laughter have been a source of solace amidst the challenges of doctoral studies.

Table of Contents

Acknowledgements ii
Table of Contents iii
List of Tables v
List of Figures vi
List of Abbreviations vii
Chapter 1. Introduction 1
Chapter 1.1. RioK1: an Atypical Kinase with ATPase Activity 5
Chapter 1.2. Role of Dual Function RioK1 in Ribosome Biogenesis 8
Chapter 1.3. Targeting Ribosome Biogenesis for Therapeutics 9
Chapter 1.4. Targeting RioK1 as a Treatment for Colorectal Cancers 15
Chapter 1.5. Toyocamycin, the First Small Molecule Inhibitor for RioK1 16
Chapter 1.6. PRMT5: Another Oncogenic Protein Using RioK1 as an Adaptor Protein 17
Chapter 1.7. Objective 19
Chapter 2. Characterization of Adenosine-like Small Molecules and RioK1 from archaeoglobus fulgidus 20
Chapter 2.1. Introduction 20
Chapter 2.2. Results and Discussion 23
Chapter 2.2.a. Small Molecule Library Generation 23
Chapter 2.2.b. Thermal Shift Assay (TSA) 27
Chapter 2.2.c. Kinase and ATPase activity Assay 28
Chapter 2.2.d. Co-crystallization of afRioK1 with KPSH02 29
Chapter 2.3. Experimental Procedures 34
Chapter 2.3.a. Expression and Purification of afRioK1 34
Chapter 2.3.b. SILCS Simulation 36
Chapter 2.3.c. Thermal Shift Assay 38
Chapter 2.3.c. afRioK1 Co-crystallizations with Adenosine-like Compounds 38
Chapter 3. Characterization of the RioK1-PRMT5 Complex 40
Chapter 3.1. Introduction 40
Chapter 3.2. Results and Discussion 42
Chapter 3.2.a. Overall Structure of ctPRMT5 42
Chapter 3.2.b. Conservation of Residues Within the Yeast Sequences 48
Chapter 3.2.c. Catalytic Activity of ctPRMT5 54
Chapter 3.3. Methods 57
Chapter 3.3.a. Cloning and Purification of PRMT5 57
Chapter 3.3.b. Size Exclusion Chromatography 59
Chapter 3.3.e. Crystallization 60
Chapter 3.3.f. MALDI-MS Detection of ctPRMT5 Mono-/Di- Methylation 60
Chapter 3.3.g. SAM 510: SAM Methyltransferase Assay and SAMfluoro: SAM Methyltransferase Assay 61
Chapter 4. Determining the Structure Activity Relationship of RioK1 as a Kinase and Adaptor Protein 63
Chapter 63
Chapter 4.1. Modification of the 1,2,4-triazole scaffold on KPSH02 63

Chapter 4.2. Crystal Structures in Progress 67
Chapter 4.2.a. afRioK1 and SILCS Screen Compounds 67
Chapter 4.2.b. afRioK1 and Compound 5004 68
Chapter 4.2.c. afRioK1 and Compound 46552 71
Chapter 4.3. Elucidating the PRMT5-MEP50-RioK1 Protein Complex 73
Chapter 5. Conclusion 77
Appendices 80
A. ^{13}C NMR of compound 41000 80
B. ^{13}C NMR of compound 42116 80
C. ^{13}C NMR of compound 42960 81
D. ^{13}C NMR of compound 46336 81
E. ^{13}C NMR of compound 46501 82
F. ^{13}C NMR of compound 46552 82
G. ^{13}C NMR of compound 528300 83
H. ^{13}C NMR of compound 528379 83
I. ^{13}C NMR of compound 528560 84
J. ^{13}C NMR of compound 528578 84
K. ^{13}C NMR of compound 540732 85
L. ^{13}C NMR of compound 541151 85
M. Certificate of Analysis of Compound 5004 86
N. Certificate of Analysis for Compound 18157 87
O. Certificate of Analysis for Compound 21420 88
P. Certificate of Analysis for Compound 29476 89
Q. Certificate of Analysis for Compound 34684 90
R. Certificate of Analysis for Compound 5062 91
S. Certificate of Analysis for Compound 020335 92
T. Certificate of Analysis for Compound 110862 93
U. ^{1}H NMR for compound KPSH02 94
References 95

List of Tables

Table 1. Overview of PTMs: Chemical modifications and biological regulation. 6
Table 2. List of ribosomal proteins involved in tumorigenesis and metastasis..... 13
Table 3. List of ribosomal proteins involved in therapeutic resistances. 14
Table 4. Data processing and refinement statistics for the afRioK1-KPSH02 crystal structure..... 31
Table 5. Table of all unique hydrogen bonds and salt bridge interactions in the Dimer and Tetrameric interfaces..... 46
Table 6. Data collection statistics for the three crystals structures in progress..... 67
Table 7. Interactions between the RioK1-PBM peptide and PRMT5 TIM barrel. 76

List of Figures

Figure 1. PDB entries per year. 2
Figure 2. Human RioK1 crystallized with ADP and Mg^{2+}(PDB: 4OTP). 7
Figure 3. General SN2 kinase mechanism of action for serine/threonine kinases. 8
Figure 5. The three types of methylation performed by the PRMT family. 18
Figure 6. The use of MD simulations and CADD software to facilitate lead compound discovery. 23
Figure 7. Atom labelling of the adenosine backbone. 24
Figure 8. Comprehensive list of the top 21 compounds selected from FragMap guided similarity search. 25
Figure 9. Thermal stability contributions from top compounds from similarity search and synthesized compound KPSH02 with afRioK1 highlighted in green. 27
Figure 10. KPSH02 inhibits afRiok1 similarly to Toyocamycin 29
Figure 11. Structure of the afRioK1-KPSH02 complex and sequence comparison to human enzyme. 32
Figure 12. Occupancy test of the afRioK1-KPSH02 complex. 33
Figure 13. Structure of ctPRMT5. 43
Figure 14. Structure of tetrameric ctPRMT5. 44
Figure 15. Real space refinement of the active site of ctPRMT5. 47
Figure 16. Structure of ctPRMT5 monomer with consurf overlay. 48
Figure 17. Multiple sequence alignment of ctPRMT5 against 11 other fungal homologs. 50
Figure 18. Multiple sequence alignment of ctPRMT5 against 9 other species. 53
Figure 19. Methyltransferase activity of ctPRMT5. 55
Figure 20. Mass Spectra of ctPRMT5 monomethylation. 57
Figure 21. Differences between compound KPSH02 and theoretical compound KPSH06 and their interactions with afRioK1. 65
Figure 22. KPSH02 modelled into NADK (1Z0S) showing the triazole ring occupying the metal cation space. 66
Figure 23. Electron density of afRioK1 + 5004 sample. 70
Figure 24. Examination of unmodelled electron density inside the active site of afRioK1-46552 complex. 72
Figure 25. Interactions between RioK1 PBM sequence (Cyan) and PRMT5 (Green). 74
Figure 26. Docking simulation of wild type and mutant RioK1 PBM to PRMT5. ... 77

List of Abbreviations

RioK1	Rio Kinase I
afRioK1	*Archaeoglobus fulgidus* Rio Kinase I
PDB	Protein Data Bank
NMR	Nuclear Magnetic Resonance
XRC	X-ray Crystallography
Cryo-EM	Cryo-Electron Microscopy
CADD	Computer Aided Drug Design
LBDD	Ligand Based Drug Desing
SBDD	Structure Based Drug Design
QSAR	Quantitative Structure Activity Relationship
PTMs	Post Translational Modifications
ePKs	Eukaryotic Protein Kinases
aPKs	Atypical Protein Kinases
Rio	Right open reading frame
p-loop	Phosphate Binding Loop
c-loop	Catalytic loop
DFG loop	Metal Binding Loop
60SSU	60 Svedberg subunit
40SSU	40 Svedberg Subunit

rRNA	Ribosomal Ribonucleic Acid
rDNA	Ribosomal Deoxyribonucleic Acid
Ncl	Nucleolin
CRC	Colorectal cancer
RNAi	Ribonucleic Acid Interference
MM	Multiple Myeloma
ROS	Reactive Oxygen Species
PRMTs	Protein Methyltransferases
MMA	Mono-methylated arginines
MTAP	Methylthioadenosine Phosphorylase
MTA	Methylthioadenosine
MAT2A	Methionine adenosyltransferase II alpha
SAM	s-adenosylmethionine
Pi	Inorganic phosphate
SILCS	Site Identification by Ligand Competitive Saturation
MD	Molecular Dynamics
Tm	Melting Temperature
ctPRMT5	*Chaetomium thermophilum* Protein Arginine Methyltransferase type 5

ED	Electron Density
SAH	s-adenosyl homocysteine

Chapter 1. Introduction

The field of structural biology has improved significantly over the past few decades as advancements in technology and methodology have made it easier to obtain atomic resolution structures. These structures provide useful information that other researchers can access via the protein databank (PDB). The PDB is a collection of biological structures that were determined using techniques such as x-ray crystallography (XRC), Cryo Electron Microscopy (Cryo-EM), and nuclear magnetic resonance (NMR). Since the inception of the PDB in 1971, the number of entries has increased dramatically in recent years, giving researchers access to a wealth of structural information (Figure 1).[13, 14] The number of pdb entries per year remains relatively constant, however, over time the total entries available accumulates granting users to a wide range of structural information. The information gained by structural biology plays a key role in the drug design pipeline. Designing a therapeutic is a costly process, where drug candidates are often terminated during stage 3 clinical trials. The use of computer aided drug design (CADD) has helped reduce the costs of finding good lead compounds and/or drug scaffolds.[15]

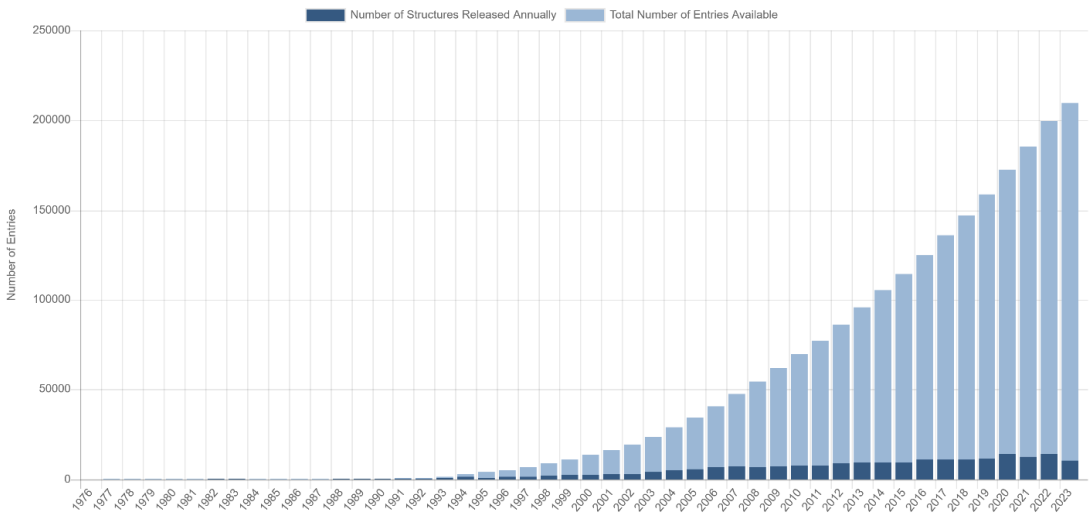

Figure 1. PDB entries per year.

CADD can be broadly separated into two major methods, ligand-based drug design (LBDD) and structure-based drug design (SBDD). In LBDD, the approach is to focus on the structure of the target small molecule and is an alternative route when not much is known about the target protein. LBDD is centered around the hypothesis that similar structural compounds may possess similar biological activities and is widely accepted to predict other physicochemical properties.[16] One of the main techniques of LBDD is termed quantitative structure activity relationship (QSAR). Briefly, QSAR uses structural information and available bioactivity data about the properties of a small molecule for high-throughput screening to identify potential lead compounds that mimic the structure of the target small molecule.[15-17]

On the other hand, SBDD relies heavily on the pre-existing structure of a drug target to engineer an inhibitor. The first step is the identification of a good drug target, which is a protein, enzyme, or other biomolecule that has a significant contribution to a disease phenotype. Secondly, a good drug target should have a structural and/or functional characteristic that can be exploited for therapeutic

development, such as a ligand binding site, allosteric binding site, multiple states of inactivity/activity, or even varying conformations that are important for propagation of the disease state. High resolution structures of the target protein allow for *in silico* high-throughput screening of existing inhibitor libraries to hasten the search for potential lead compounds.[18] Solving the structure between the lead compound(s) and the target protein can result in near atomic resolution structures of protein-drug complexes, that can be used to characterize important interactions or unused spaces within the target protein's ligand binding site for additional engineering of drug affinity. The information from the protein-drug complexes is used to increase the structure activity relationship between the target protein and drug candidate. For example, the catalytic region of the kinase family of proteins is highly conserved; however, researchers have been able to use conserved and non-conserved areas to design tailormade inhibitors specific to a targeted kinase.[2, 4, 5]

Fragment-based drug discovery is a type of SBDD method that uses small molecule fragments, rather than full compounds, to bind to the target protein. Fragment-based screening is a great way to identify fragments that can be modified or combined with other fragments to create drug-like molecules. However, because the energies of fragment binding are low, screening fragments experimentally is time consuming and costly.[19] Site Identification by Ligand Competition Saturation (SILCS) is a computational method that alleviates the problem of detecting and characterizing fragment binding. Unlike other MD simulation methods, SLICS utilizes three core aspects in its simulations: protein flexibility, water, and solutes.[19] Essentially, SILCS submerges the target protein in a concentrated aqueous solution

containing multiple small molecules. Multiple nanosecond-length molecular dynamics (MD) simulations are then run, analyzing the probability of small molecule and water binding around the protein in each simulation. These probabilities are mapped and combined across all simulations to create a single probability map, called FragMap, for each type of fragment.[19] The generated FragMap can be used as a docking grid for high-throughput *in silico* screening. SILCS also uses a modified version of the CHARMM general force field that allows for accurate backbone representation for peptides and proteins in solution.[20, 21] However, the original SILCS MD simulation method had limitations when dealing with macromolecules with deep or totally occluded pockets as well as regions were charged functional groups bind favorably.[22] A new approach was done using the Grand Canonical Monte Carlo Molecular Dynamics (GCMC-MD) that allowed for enhanced sampling of ions and probe molecules around macromolecules. GCMC enhances probe molecule sampling by dynamically inserting and removing probe molecules and water within the simulation system. Additionally, it applies translations, rotations, and torsional rotations to further explore the system's configuration space.[22] Ligands can then simulated for binding once the FragMap has been assembled. Atoms in a target ligand are given a favorable energy score when overlapped with a specific FragMap and a huge energy penalty when outside of the specific FragMap. The sum of the scores for each of the atoms in the ligand give rise to the Ligand Grid Free Energy (LGFE) scores. The better the score the better the affinity the ligand has for the specific FragMap.[22]

Chapter 1.1. RioK1: an Atypical Kinase with ATPase Activity

Post-translation modifications (PTMs) are the process of biologically modifying proteins after ribosomal translation. There are many types of PTMs that can infer different signal transduction cascades within the cell. These signal cascades are responsible for many of the important biological processes necessary for cell survival (Table 1). Phosphorylation in particular plays a key role in cell cycle regulation and the activation and deactivation of certain proteins, regulating activity. Phosphorylation is the transfer of a phosphate group onto a target threonine, tyrosine, serine and/or histidine residue, an action typically seen in a class of enzymes called kinases. There are two classes of protein kinases, eukaryotic protein kinases (ePKs) and atypical protein kinases (aPKs). Despite having low sequence similarity, these classes are structurally conserved, especially in and around the active site. Currently, there are 13 families of aPKs, and one is the RIO (right open reading frame) family. Members of the RIO family include 4 subfamilies Rio1, Rio2, Rio3, and RioB. The Rio1 and Rio2 proteins are present in all organisms from archaea to humans; however, Rio3 is only found in higher order eukaryotes and RioB is an uncharacterized group of bacterial RIO proteins.[23, 24] Rio Kinase 1 (RioK1) is seen as

the head of the Rio family exhibiting dual functionality as a kinase and an ATPase.

Name of PTM	Chemical Modification	Regulated Biological Process
Acetylation	Attaching acetyl group (CH3CO)	Gene Expression
Farnesylation	Adding an Isoprenyl group to a cysteine residue	Intracellular Signal Transduction
Formylation	Addition of a formyl functional group	Gene Expression
Geranylgeranylation	Adding 1 or 2 twenty carbon lipophilic geranylgeranyl isoprene to Cys	Membrane association
Glycosylation	Enzymatically attaching glycans to proteins	Protein structure folding, stability, distribution and activity
Hydroxylation	Introducing a hydroxyl group	Protein-Protein Interactions
Methylation	Adding a methyl group	Gene expression
N-Acetylation	Transfer acetyl group to nitrogen residue on target protein	Genome and chromatin stability, regulating transcription, regulation of cell cycle
Palmitoylation	Covalent attaching fatty acids to cysteine, serine or threonine	Protein regulation, signal transduction, apoptosis
Phosphorylation	Attaching a phosphoryl group	Cell cycle regulation, activation/deacitivation of certain proteins
Ubiquitination	Addition of ubiquitin	Degradation of protein, DNA repair signaling

Table 1. Overview of PTMs: Chemical modifications and biological regulation.

The general structure of RioK1 can be described as a bilobed structure held together by a hinge region and at the interface of these two lobes is the active site (Figure 2).[25] Several studies have elucidated the minimal level of structural subdomains that make up the Rio catalytic domain. These subdomains include a nucleotide binding loop (p-loop) that is responsible for positioning the tri-phosphate group on ATP, a catalytic loop (c-loop) that contains a conserved catalytic Aspartate and Asparagine residue for γ-phosphate transfer, a hinge region that connects both N- and C-terminal lobes making direct interactions with the adenine moiety and a metal-binding loop (DFG loop) that contains a conserved Aspartate residue for metal ion

positioning. What makes the Rio domain unique is that they lack the activation loop and substrate binding loop typically seen in ePKs.[23, 24] This indicates that RioK1 interacts with their substrate in a different manner and that it may be able to bind a diverse range of substrates when compared to canonical ePKs.

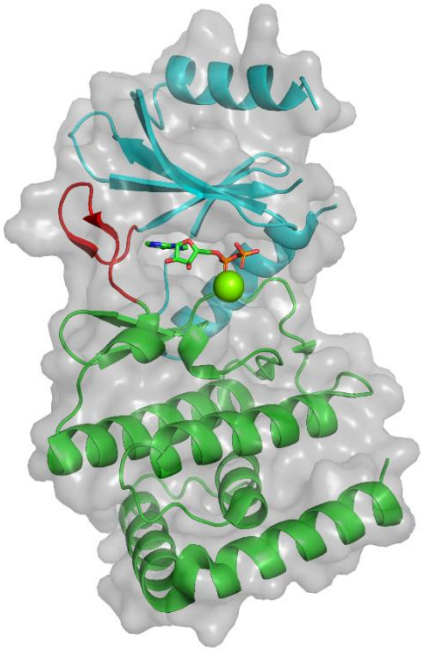

Figure 2. Human RioK1 crystallized with ADP and Mg^{2+}(PDB: 4OTP).

Note. N-terminal lobe is highlighted in blue, C-terminal lobe is highlighted in green, and hinge loop is highlighted in red.

The structure of RioK1 was first solved using the orgainsim *Archaeoglobus fulgidus* using XRC by LaRonde et al.[23] Followed by the structure of human RioK1 (143-494) in complex with ADP and Mg^{2+} (PDB: 4OTP) in 2014.[7] In the truncated human RioK1 + ADP complexed structure, a phosphoaspartate (pAsp) was observed in the active site, something typically seen in p-type ATPases. The serine kinase mechanism starts with the catalytic aspartate acting as a general base activating a substrate serine for attack on the γ-phosphate, causing a temporary intermediate

which will then form a phosphoserine and ADP (Figure 3). However, the catalytic Asp responsible for the kinase mechanism in RioK1, is not the same Asp observed in the ATPase activity, further supporting ATPase activity in RioK1.

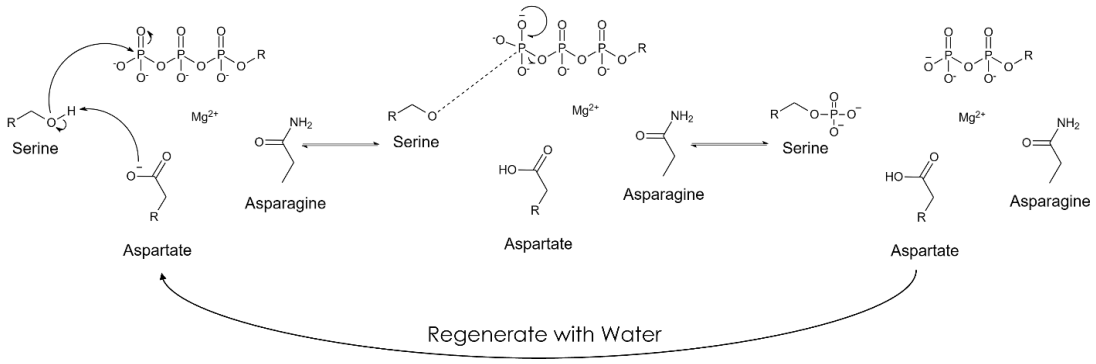

Figure 3. General SN2 kinase mechanism of action for serine/threonine kinases.

Chapter 1.2. Role of Dual Function RioK1 in Ribosome Biogenesis

The Ribosome is a complex macromolecular machine responsible for the translation of mRNA into proteins in both prokaryotes in eukaryotes. In humans, the ribosome is made up of 2 subunits the larger 60S subunit (60SSU) and the smaller 40S subunit (40SSU) and together they make the 80S ribosome.[25-30]

Taking place in the nucleolus, Ribosome biogenesis is a highly regulated complex process involving many steps from ribosomal RNA (rRNA) transcription, maturation of pre-rRNA to rRNA, assembly of pre-ribosomal factors, to late RNA processing.[27, 28, 31, 32] Over 700 proteins ranging from chaperones to ribosomal and non-ribosomal proteins, are responsible for the regulation and assembly of the mature 80S ribosome.

The 40SSU is made up of 33 ribosomal proteins and a strand of rRNA known as the 18S rRNA whereas the 60SSU contains 47 ribosomal proteins and 3 strands of rRNA the 5S, 5.8S, and 25S rRNA.[33] The function of the 40SSU is to bind, unwind,

and decode mRNA's, while the 60SSU is responsible for peptide binding and acts as a quality control for newly synthesized peptides.[26, 34, 35] A review written by Sebastian Klinge and John Woolford Jr (2019), outlines all current knowledge about ribosome biogenesis and created a comprehensive look at the assembly of the 80S ribosome.

The process can be broken down into two main parts the formation of the mature 60S particle and formation of the mature 40S particle. Through numerous immunoprecipitation studies, it has been shown that RioK1 plays a significant role in the late maturation steps of the 40SSU. After sufficient maturation of the pre-40SSU several ribosome assembly factors leave. A mature 60S particle will bind, acting as a quality control check, and successful binding of the 60SSU signals for the cleavage of the 20S pre-rRNA by endonuclease, Nob1, to form mature 18S rRNA. However, pre-40SSU that contain the Nob1 – partner of nob1 (Pno1) complex leads to an accumulation of translation deficient 80S ribosomes. RioK1 has been shown to bind to the pre-40SSU after the formation of the 18S rRNA (post Nob1 cleavage) to release the Nob1-Pno1 complex from the pre-40SSU. Mature 40S particles without the Nob1-Pno1 complex saw a decrease in pre-40SSU and pre 20S rRNA, and an accumulation of mature 80S ribosome. The releasing mechanism of the Nob1-Pno1 complex from the pre-40SSU was also linked with the ATPase activity of RioK1, through ATP depletion studies using RioK1 knockout cell lines and catalytically dead RioK1 mutants.[29, 36]

Chapter 1.3. Targeting Ribosome Biogenesis for Therapeutics

Ribosome biogenesis is responsible for the regulation and assembly of the ribosome, a complex multiunit protein responsible for the assembly of other proteins.

Dysregulation in ribosome assembly can have adverse or even lethal effects to the cell/host. In fact, some studies have shown that hyperactive ribosome biogenesis is linked as a potential initiator of carcinogenesis and/or a byproduct of certain types of cancers. It is generally thought that hyperactive ribosome biogenesis was the result of tumorigenesis, until emerging evidence suggested that hyperactive ribosome biogenesis could be a major driver for tumorigenesis.[37-48] In a study by Bywater et al, it was demonstrated that B-lymphoma cells, when compared to normal B cells, relied heavily on elevated ribosomal DNA (rDNA) transcription making them more susceptible to RNA polymerase I inhibition.[39] As more research is being done to characterize the role ribosome biogenesis plays in cancer, it is becoming evident that alterations at any step in ribosome assembly can drive tumorigenesis. Back in 2002, an article titled "The Ribosome Filter Hypothesis" suggested that the ribosome was heterogeneous, meaning the ribosome could have some variation in its composition (rRNA modifications, post-translational modifications, variation in rRNA and ribosome-associated proteins, etc.) to allow for the assembly of specialized ribosome or in the case of cancer, "onco-ribosomes".[46, 49, 50] Since then there have been many publications showing the involvement of ribosome heterogeneity in cancer.[43, 44, 48] This ribosomal heterogeneity is a mixed blessing for cancer therapeutics. While certain ensembles of onco-ribosomes can be used for structure-based drug design for guided inhibition of select cancers, screening for lead compounds that interact with the target area within the desired onco-ribosome is difficult.

Despite this, selective inhibition of ribosome biogenesis for the treatment of certain cancers and diseases is currently underway as an important strategy for drug

development. Tables 2 and 3 outline some of the ribosomal proteins involved in different types of cancer and diseases.[49] There are many avenues that can be targeted in the ribosome for the selective inhibition of certain cancer and tumor types; however, one of the most targeted aspects of ribosome biogenesis is RNA polymerase I (RNA Pol I). The concept of RNA Pol I inhibition is based around the idea that cancer cells rely on increased RNA Pol I transcription activity than compared to normal cells, sparing them from treatment.

This targeting approach gave rise to the first specific and orally available inhibitor for RNA Pol I, termed CX-5461.[51, 52] CX-5461 works by disrupting Nucleolin (Ncl) or Selective factor I from binding rDNA, reducing recruitment of RNA Pol I to the rDNA promoter.[51] Additionally, there are two small molecule inhibitors that target RNA Pol I, BMH-21 and PMR-116, showing therapeutic promise.[53-55] Success in targeting RNA Pol I for therapeutics has proven that targeting ribosome biogenesis is a viable way to target specific pathways for tumorigenesis, however there are many ribosome assemble factors that comprise of the ribosome biogenesis sphere that have yet to be targeted.

Ribosomal protein	Expression level/status	Cancer type	Phenotype
Ribosomal proteins in tumorigenesis and metastasis			
RPL5	Mutated (missense)	T-ALL, melanoma, and GBM	RPL5 mutations dysregulated the HDM2/p53-mediated ribosome biogenesis checkpoint with subsequent dysregulation in ribosome biogenesis
RPL10	Mutated (missense)	T-ALL	RPL10 R98S mutant leukemia cells showed a ribosome biogenesis defect. RPL10 R98S mutant leukemia cells showed enhanced IRES-mediated translation and high tolerance to high oxidative stress levels
RPL15	Upregulated	Colon cancer	Silencing of RPL15 inhibited cell proliferation and induced apoptosis
	Upregulated	Gastric cancer	Knockdown of RPL13 inhibited cell proliferation, migration, and tumor growth *in vivo*
RPL19	Upregulated	Prostate cancer	Increased RPL19 expression was predictive of shorter patient survival. Silencing RPL19 suppressed tumor growth *in vivo*.
	Upregulated	Hepatocellular carcinoma	Overexpression of RPL19 predicted poor prognosis.
RPL22	Downregulated	Lung cancer (NSCLC)	Downregulation of RPL22 is associated with carcinogenesis.
	Deletions	T-ALL	Haploinsufficiency or monoallelic loss of RPL22 accelerated development of T-ALL.
RPL23	Upregulated	MDS	Silencing RPL23 suppressed cell proliferation and increased apoptosis. RPL23 overexpression was associated with apoptotic resistance and higher risk of MDS
	Upregulated	High-grade serous ovarian carcinoma	Higher RPL23 mRNA levels were associated with worse prognoses.
RPL26	Upregulated	Pancreatic cancer	Knockdown of RPL26 suppressed cell proliferation.
RPL29	Upregulated	Pancreatic cancer	Knockdown of RPL29 suppressed cell proliferation.
RPL34	Upregulated	Glioma	Knockdown of RPL34 suppressed proliferation and migration of glioma cells.
	Upregulated	NSCLC	Knockdown of RPL34 suppressed cell proliferation and enhanced apoptosis in NSCLC cell lines.
	Upregulated	Osteosarcoma	High levels of RPL34 are associated with poor prognosis for patients with osteosarcoma. Knockdown of RPL34 inhibited cell proliferation, induced cell apoptosis.
	Upregulated	Oral squamous cell carcinoma	Knockdown of RPL34 inhibited cell proliferation and migration.
RPL41	Downregulated	Retinoblastoma	RPL41 peptide therapy improved sensitivity to carboplatin. RPL41 peptide therapy induced apoptosis and inhibited cell migration.
	Downregulated	Breast cancer	RPL41 downregulation is associated with malignant transformation.
RPS2	Upregulated	Prostate cancer	Knockdown of RPS2 suppressed cell proliferation and induced apoptosis in malignant prostate cells.

Phospho-RPS6	Upregulated	Lung cancer	High levels of phospho-RPS6 are associated with shorter metastasis-free survival.
RPS15	Mutated (missense)	CLL	RPS15 mutant primary CLL cells showed altered translation efficiency and rewiring of the translational program. Mutant RPS15 caused dysregulation of p53 pathway.
RPS15A	Upregulated	Colorectal cancer	High levels of RPS15A are associated with poor prognosis.
RPS20	Mutated (missense)	Colorectal cancer	RPS20 mutation was associated with a defect in pre-rRNA maturation.
RPS20	Upregulated	GBM	Higher levels of RPS20 are associated with poor prognosis.
RPS27L	Upregulated	Colorectal cancer	Elevated RPS27L expression in either feces or tissues is associated with better prognosis.

Table 2. List of ribosomal proteins involved in tumorigenesis and metastasis.

Ribosomal protein	Expression level/status	Cancer type	Phenotype
Ribosomal proteins in therapeutic resistance			
RPL3	Downregulated	Lung cancer	Overexpression of RPL3 inhibited cell migration and invasion and improved 5-FU efficacy in lung cancer cells.
RPL6	Upregulated	Gastric cancer	Downregulation of RPL6 suppressed cell proliferation. Overexpression of RPL6 promoted multidrug resistance.
RPL13	Upregulated	Gastric cancer	Knockdown of RPL13 suppressed cell proliferation. Overexpression of RPL13 promoted chemoresistance.
RPL23	Upregulated	Gastric cancer	RPL23 overexpression promoted multidrug resistance.
RPL34	Upregulated	Pancreatic cancer	Knockdown of RPL34 suppressed cell proliferation, migration, and drug resistance of pancreatic cancer cells.
RPS6	N/A	Gastric cancer	RPS6 suppression decreased cell proliferation and tumor growth in lapatinib- and trastuzumab-resistant gastric cancer models.
RPS3	N/A	GBM	In radioresistant GBM cell lines, ring finger protein 138 (RNF138) ubiquitinates RPS3 and promotes its degradation, which suppresses radiation-induced apoptosis and confers radioresistance. Silencing of RPS3 enhanced GBM cell tolerance to irradiation *in vitro*.
Phospho-RPS3	N/A	Lung cancer (NSCLC)	In radioresistant NSCLC cells, RPS3 phosphorylation plays a key role in radiation resistance and initiating a prosurvival transcriptional program.
RPS11	Upregulated	GBM	Knockdown of RPS11 impaired apoptosis and led to resistance to etoposide and doxorubicin. Higher levels of RPS11 are associated with poor prognosis.
RPS13	Upregulated	Gastric cancer	RPS13 promotes cell proliferation and multidrug resistance.
RPS27A	Upregulated	CML	Patients with CML-accelerated or blast phase have higher levels of RPS27A compared with chronic phase patients. Knockdown of RPS27A improved therapeutic efficacy of tyrosine kinase inhibitor Imatinib.
RPS27L	N/A		Rps27l deficiency sensitized Trp53 +/− mice to irradiation by inhibiting cell proliferation, impairing DNA damage response, and inducing apoptosis.
RPLP1	N/A	HNSCC	Silencing of RPLP1 promoted apoptosis and decreased radioresistance *in vitro*. Invasive HNSCC showed higher expression levels of RPLP1.

Table 3. List of ribosomal proteins involved in therapeutic resistances.

Chapter 1.4. Targeting RioK1 as a Treatment for Colorectal Cancers

Colorectal cancer (CRC) is described as a cancer that affects the colon or the rectum, and in 2020 accounted for the second largest number of cancer-related deaths in the United States.[56] Despite advancements in screening technology and therapeutics, CRC survival rates remain relatively unchanged at 65%. Taking a closer look at the 65% percent survival rate, when the cancer is localized the survival rate is at 90%, but when the cancer spreads to distant parts of the body via metastasis the survival rate drops drastically to about 14%. Around 22% of patients are diagnosed at the distant CRC stage highlighting the importance of characterizing CRC growth and metastasis to effectively treat CRC.[56]

Recent studies showed that RioK1's plays an oncogenic role in CRC tumorigenesis. RioK1 exhibits a significant increase in expression within CRC cell lines and tissues, with a corresponding 4-fold elevation in CRC and 6-fold increase in metastatic lymph node samples. Furthermore, there is a robust association between RioK1 overexpression and unfavorable prognosis and mortality.[57, 58] Studies using RNA interference (RNAi) via RioK1-specific short hairpin RNAs knockdown in CCK-8 and colony formation assays, showed that downregulation of RioK1 halted the proliferation rate, as well as the migratory and invasive capacities of HCT116 human colon cancer cells. Conversely, RioK1 overexpression into a rectal carcinoma cell line, RKO, substantially enhanced cell viability, migration, and invasion.[58] These findings were corroborated by another study using HCT116 and LoVo (colorectal cancer cell line) cell lines.[57] Chen et al. demonstrated that treating both cell lines with a known RioK1 inhibitor, toyocamycin, resulted in stunted colony growth and tumor

size in a dose-dependent fashion. Interestingly when the toyocamycin group was subjected to IR therapy, it had a synergistic effect in decreasing tumor volume. Targeting RioK1 may prove a viable way to treat certain types of cancer. However, the use of toyocamycin poses certain risks, most notably those arising from "off-target" effects.

Chapter 1.5. Toyocamycin, the First Small Molecule Inhibitor for RioK1

Toyocamycin, 7-cyano-7-deazaadenosine, is an adenine derivative that contains a nitrile group at the N7 position. Toyocamycin was reported as a successful small molecule inhibitor for a large variety of proteins, some of which display anticancer/antitumor activity.[9, 11] In human multiple myeloma (MM) cells, toyocamycin showed synergistic effects with bortezomib for inducing apoptosis in MM cells and bortezomib-resistant MM cells at nanomolar concentrations. Such effects arose by inhibiting the IRE1α-induced XBP1 mRNA cleavage pathway.[11] Furthermore, toyocamycin was shown to induce selective apoptosis towards prostate cancer PC-3 cell lines by targeting reactive oxygen species (ROS) pathways.[10]

While toyocamycin has some promising results, its ability to non-discriminately bind to multiple protein kinases, as well as other proteins, can lead to potential off-target effects and cytotoxicity.[8-12] Furthermore, toyocamycin analogs have only been engineered with minimal success with regard to enhancing selectivity and reducing cytotoxicity.[12, 59, 60] In one study, Wang et al. were able to show that the toyocamycin analog, 4-Amino-7-(/3-D-ribofuranosyl)pyrrolo[2,3-(i]pyrimidine-5-car-boxamidrazone changed Type 1 and Type 2 cytokine levels with the goal of combating autoimmune disease.[60, 61] More recently, toyocamycin was found to bind

atypical Rio (right open reading frame) kinases, a key regulator of ribosome biogenesis and cell cycle progression.[7, 24, 62]

Chapter 1.6. PRMT5: Another Oncogenic Protein Using RioK1 as an Adaptor Protein

Like phosphorylation, methylation is another type of post-translation modifier involved in many cellular processes involving gene regulation.[63-66] Enzymes responsible for catalyzing methyl group transfer onto a target substrate are known as a methyltransferase. There are different types of methyl transfers based on the target residue, arginine methylation being one of the more prominent types of methylation. Protein arginine methyltransferases (PRMTs) are responsible for catalyzing arginine methyl transfers. There are only 9 mammalian methyltransferases identified, to date, and they are categorized by their methylation capabilities. There are three types of methylation: type I and III methylate arginine at one of the guanidinium nitrogen's (ω-N^G) on the arginine side chain forming monomethylarginines (MMA), unlike type III, type I is able to go a step further by methylating the same ω-N^G forming asymmetric dimethylarginines (ω-N^G, N^G), lastly types II methyltransferases are capable of ω-N^G, N'^G-symmetric dimethylarginines (Figure 4). PRMT type 5, PRMT5, is one of the most studied type II methyltransferases and is involved in mono- and symmetric demethylation of histones. Known histone substrates of PRMT5 include H3R2, H3R8, and H4R3. Additionally, PRMT5 has non-histone substrates including p53, N-MYC, SmD3, Ncl and RNA polymerase II.[63-68] Similar to RioK1, dysregulation of PRMT5 have been linked to various types of cancers. PRMT5 has been shown to be overexpressed in lymphomas, lung cancer, breast

cancer, and colorectal cancer.[69-75] As a result of, PRMT5 a great therapeutic target with several inhibitor already in development, two of which are currently in clinical trials EPZ015938 and JNJ-64619187.[71, 75, 76]

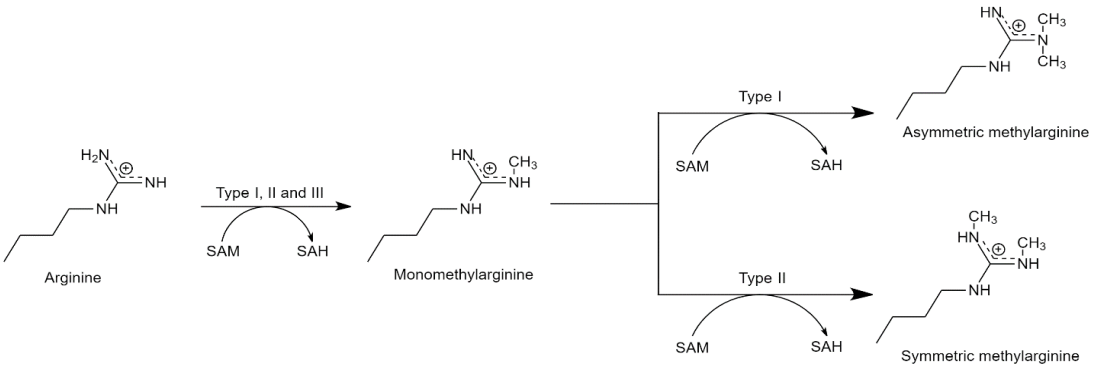

Figure 4. The three types of methylation performed by the PRMT family.

In 2010, RioK1 was identified as a binding partner of PRMT5 by Guderian *et al.*[68] It was found in these studies that that RioK1 competes with the methylosome subunit, PICln, for the same binding site on PRMT5. Later in 2016, it was found that methylthioadenosine phosphorylase (MTAP) deleted cancers create vulnerabilities in PRMT5 that extends to upstream and downstream interactors. Depletion of MTAP results in the accumulation of the MTAP substrate, MTA, which at increased concentrations inhibits PRMT5 activity. This vulnerability extends to upstream effector methionine adenosyltransferase II alpha (MAT2A), which is responsible for using MTA to generate PRMT5 substrate s-adenosylmethionine (SAM), and downstream effector RioK1 used to recruit substrates to PRMT5. Uncovering RioK1 involvement with PRMT5 and MTAP depleted cancers led to the discovery of the first PRMT5 substrate adaptor protein inhibitor, BRD0639.[77] BRD0639 targets the PRMT5-RioK1 complex and disrupts this interaction, reducing substrate methylation.

Chapter 1.7. Objective

The objective of this work is to characterize RioK1 with respect to small molecule inhibition and to better understand who it regulates PRMT5 with an overall goal of contributing to the development of selective Rio inhibitors. In chapter 2, the methodology to search, screen, and characterize lead compounds for afRioK1 will be explained, which includes providing a structure of a promising inhibitor bound to afRioK1. Chapter 3 will illustrate the interaction between RioK1 PRMT5 in detail as well as introduce the structure of PRMT5. Chapter 4 will present the future directions on the ongoing research projects towards elucidating the structure activity relationship of RioK1 as a kinase and adaptor protein, and Chapter 5 will summarize the findings and discuss overall implications of this research.

Chapter 2. Characterization of Adenosine-like Small Molecules and RioK1 from archaeoglobus fulgidus

Chapter 2.1. Introduction

RioK1 stands at the forefront within the Rio kinase family, representing an aPK that diverges from canonical ePK due to distinct sequence similarity and the absence of key structural subdomains, including VIII, X, and XI.[24] RioK1 is unique for its dual functionality, encompassing the canonical kinase role of transferring the γ-phosphate from ATP to a target substrate, along with its distinct capacity to cleave the γ-phosphate from ATP, yielding ADP and inorganic phosphate (Pi).[7, 23, 24, 62] Functioning as a post-translational modifier, RioK1 is involved in several cellular pathways, ranging from ribosome biogenesis to cell cycle progression and chromosome maintenance.[78-81] RioK1 is known to play an important role in 40S ribosomal subunit maturation and participates in mature 60S subunit binding and pno1 release. Pno1 liberation is crucial, as without this release, the nascent 40S subunit remains unable to mature.[29, 36, 82]

Significant dysregulation of RioK1 activity is discernible across a spectrum of cancers, including breast, lung, and colorectal cancers, with marked prominence in specific cancerous genotypes such as Ras-driven and MTAP-deleted cancers.[72, 83-85] Given RioK1's intricate involvement in both cancer and ribosome biogenesis, it emerges as an alluring therapeutic target.[8-12] The identification of Toyocamycin in 2012 as an adenosine analog capable of nanomolar-range inhibition of RioK1 further underscored its therapeutic potential.[7]

Toyocamycin's efficacy as a small molecule inhibitor, spans an array of proteins, some of which exhibit antitumor activities.[9, 11] Particularly intriguing is Toyocamycin's synergistic action with bortezomib in human multiple myeloma (MM) cells, inducing apoptosis in both MM cells and bortezomib-resistant MM cells at nanomolar concentrations, an effect attributed to its inhibition of the IRE1α-induced XBP1 mRNA cleavage pathway.[11] Furthermore, Toyocamycin's capacity to selectively induce apoptosis in prostate cancer PC-3 cell lines by targeting reactive oxygen species pathways augments its pharmacological appeal.[10] However, the compound's propensity for non-specific binding to multiple protein kinases, along with other proteins, raises concerns regarding potential off-target effects and cytotoxicity.[8-12] In response, researchers have undertaken the synthesis and screening of Toyocamycin analogs and adenosine derivatives to enhance selectivity and diminish cytotoxicity.[12, 59-61]

Site-Identification by Ligand Competitive Saturation (SILCS), a variant of Structure-Based Drug Design, offers a methodology to generate functional group free energy maps, referred to as FragMaps (Figure 5A). Employing molecular dynamics (MD) simulations to accommodate protein flexibility and solvent-solute interactions, FragMaps provides insight for initial lead compound screening.[86] An in silico investigation of Toyocamycin within the RioK1 protein structure (PDB: 4OTP) reveals an unoccupied space proximal to the ribose 5'-end, indicative of a potential binding site (Figure 5B).[87]Utilizing insights from the RioK1-ADP-Mg FragMap (Figure 5A, 5C), a similarity search identifies a comprehensive repertoire of compounds with potential affinity for RioK1. Aiming to identify inhibitors emulating

Toyocamycin's tight binding while affording increased selectivity, the adenosine backbone was used.

Parallel to the similarity-based screening approach, deliberate synthesis of specific compounds, such as KPSH02, was also employed, seeking to enhance RioK1 selectivity. KPSH02, a synthesized Toyocamycin analog, exhibits promise as a RioK1 inhibitor. Sharing structural similarities with Toyocamycin, KPSH02 diverges through the incorporation of a 1,2,4-triazole ring anchored to the 5'-ribose carbon via a thiol group, replacing the hydroxyl group.[25] Evaluation of KPSH02's potential as a therapeutic for RioK1-associated cancers necessitates structural biology and enzymology techniques to illuminate its interaction with afRioK1.

This chapter presents a 2.0 Å resolution structure of archaeoglobus fulgidus RioK1 complexed with KPSH02. The complex reveals intricate interactions established between KPSH02 and the catalytic pocket of afRioK1. Subsequent basic enzymatic profiling of KPSH02 unveils its inhibitory impact on afRioK1 ATPase activity, though not rivalling the efficacy demonstrated by Toyocamycin.

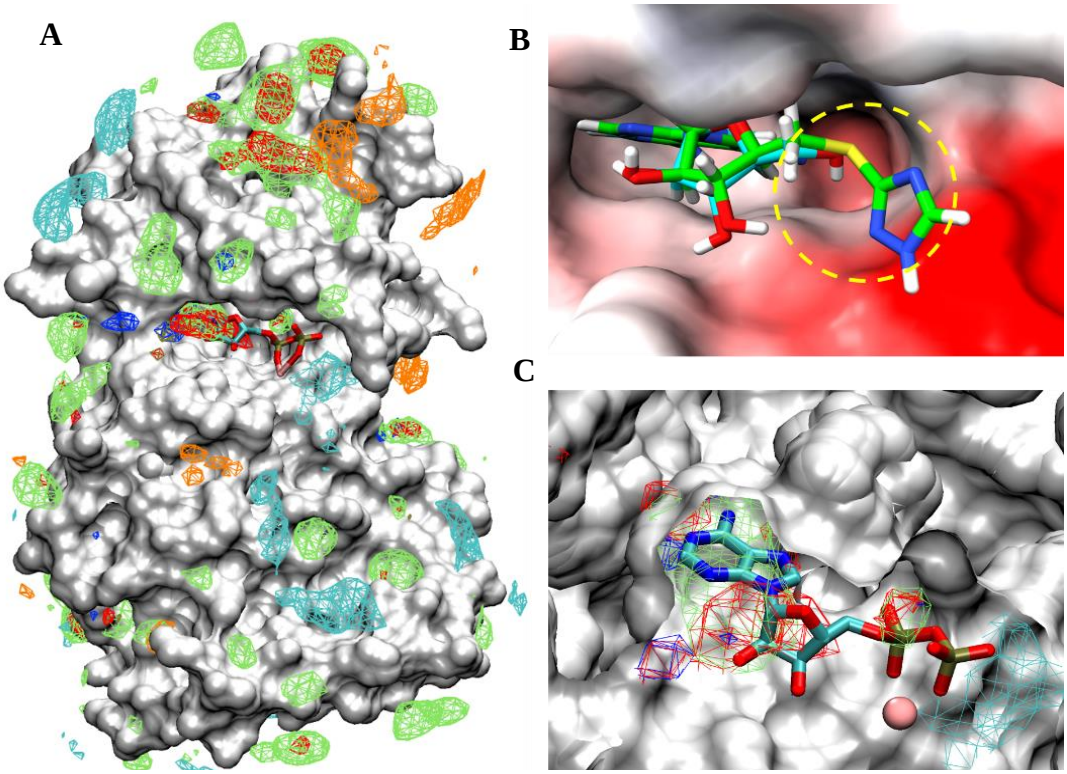

Figure 5. The use of MD simulations and CADD software to facilitate lead compound discovery.

(A) FragMap generated using SILCS with RioK1-ADP-Mg^{2+} complex (PDB: 4OTP). Color scheme is as follows apolar: Green, -0.9 kcal/mol; H-bond Acceptor: Red, -0.9 kcal/mol; H-bond Donor: Blue, -0.9 kcal/mol; Positively charged: Cyan, -1.5 kcal/mol; Negatively charged: Orange, -1.5 kcal/mol.. (B) MD simulations of toyocamycin (blue) and KPSH02 (green) replacing ADP, displaying unutilized space. (C) Close-up view of the generated RioK1 FragMap with ADP and Mg^{2+} inserted into active site, showing SILCS was successful in identifying functional groups.

Chapter 2.2. Results and Discussion

Chapter 2.2.a. Small Molecule Library Generation

To search for purchasable compounds which are analogs to the known RioK1 ligands, a similarity search was conducted against the Molport and Enamine libraries. Through visual inspection on the crystal binding mode of Toyocamycin with afRioK1 (Figure 5B), cavity at the binding site near the binding position of sugar pucker can be utilized to introduce additional functional groups to the adenosine-based scaffold

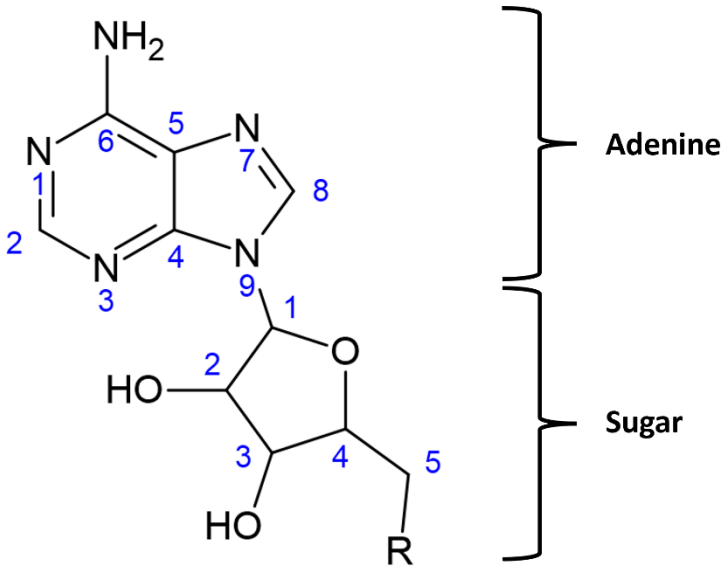

Figure 6. Atom labelling of the adenosine backbone.

to explore more binding possibilities. Thus, a similarity search was performed to request commercially available compounds that have additional substituents at the sugar pucker 4' position. 21 compounds including 5 from Enamine and 20 from Molport database were located (Figure 6). They all retain the adenosine scaffold with different functional groups attached to the 4' position of sugar pucker. Since the commercial compounds that are available for substitutions at ribose 4' position, are few. Another round of similarity searches was also conducted to search for compounds that maintain adenosine scaffold but have additional functional groups attached to the 8th position on the adenine ring. Based on visual inspection of the crystal binding mode of Toyocamycin with afRioK1 (Figure 5B), attachment at this position can also be accommodated by the binding pocket. As a result, 17 compounds were located from the Molport database. Extra efforts were also made to look for purchasable compounds which maintain the adenine scaffold while the ribose portion being replaced by some similar chemical functional groups. 69 Enamine compounds

were found from this effort, and they all retain the adenine scaffold with different functional groups attached to the 8th position on the adenine ring.

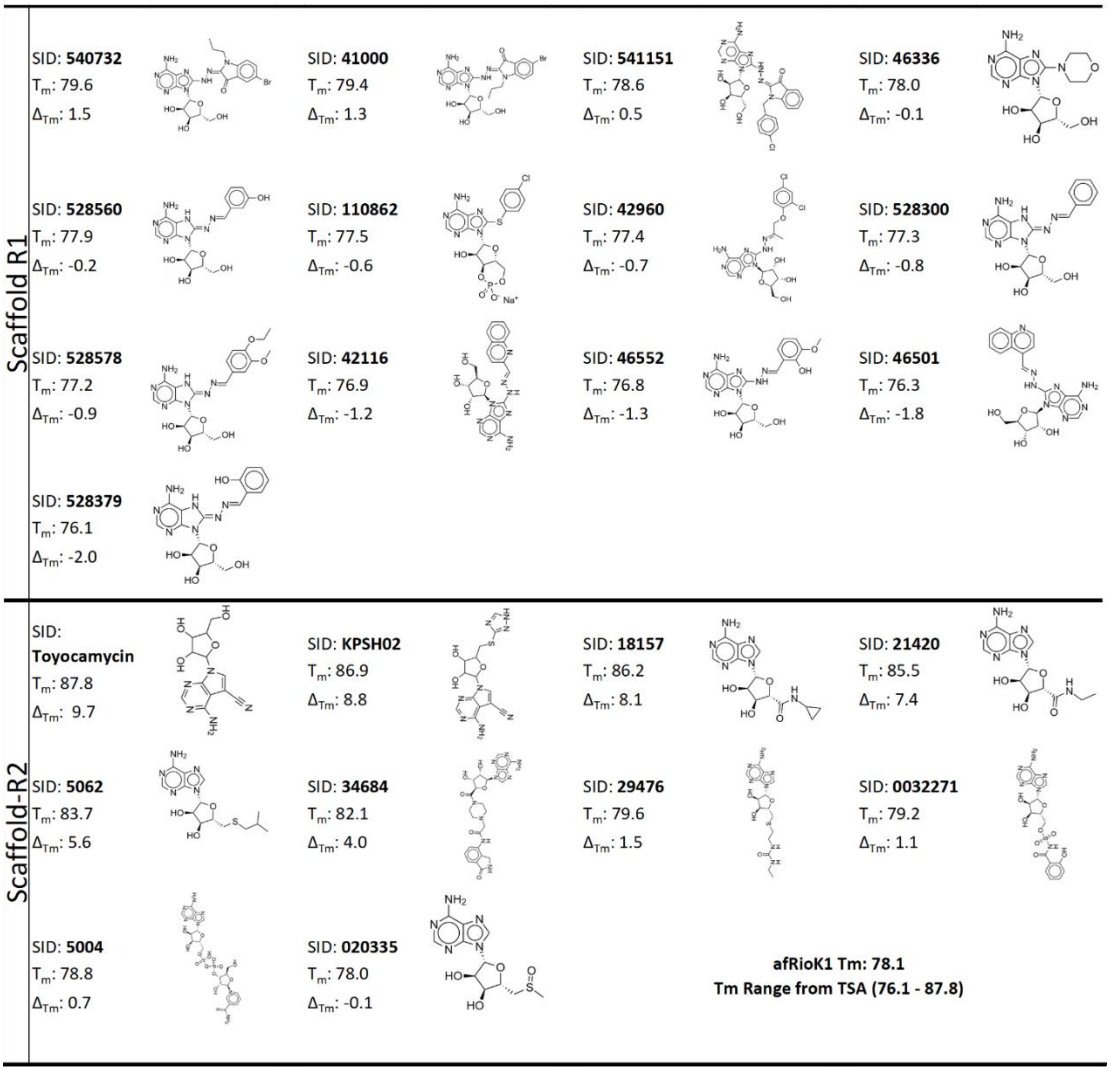

Figure 7. Comprehensive list of the top 21 compounds selected from FragMap guided similarity search.

The list provides Sample ID, the category and subcategory, MolPort ID (MPID), as well as the melting temperature from the Thermal Shift Assays. The list also includes the synthesized compound, KPSH02.

To prioritize the obtained compounds for purchasing, binding strengths of all hit compounds from similarity search was predicted. The SILCS method is used to explore binding patterns on RioK1. The SILCS method involves molecular dynamics

(MD) simulations of the target protein immersed in an aqueous solution that contains additional organic solutes of different chemical classes.[19] The solutes and water then compete for binding sites on the protein surface during the simulation, yielding a free energy fragment competition assay from which 3D fragment probability distributions of the solutes are used to define affinity patterns, termed FragMaps, encompassing a dynamic protein surface. As a summary, 111 compounds were located from Molport and Enamine catalog searches (data not shown) that have similar scaffold to the known RioK1 ligands.

The obtained adenosine analogs from similarity searches were further categorized according to the size and chemistry of substituents to facilitate the selection for assay testing. Five categories including short chain, long chain, sulfonamide containing chain, branched substituent and others, were established. The short chain category includes analogs with chain substituents at the 5'C position on the sugar that has less than 6 atoms while long chain category covers the remaining chain substituents that have more than 5 chain atoms. Sulfonamide category covers chain substituent that has sulfonamide group while branched category has analogs with substituent in branched structures. Any analogs that cannot be put into the first four categories, will be saved into the 'others' category. For each category, SILCS ligand grid free energy (LGFE) docking scores were analyzed and several top ranked analogs from each category were selected for purchasing for further testing (Figure 6).

Chapter 2.2.b. Thermal Shift Assay (TSA)

Thermal shift assays were used to screen compounds from CADD for a positive stabilizing effect on afRiok1 in vitro to validate that the compounds bind to the enzyme and have potentia for further study. Using a fluorescent dye as a marker to measure unfolding, the melting temperature (T_m) of afRioK1 was monitored. At saturating conditions of compound(s), Toyocamycin proved to contribute a highest thermal stability (87.8ºC) of afRioK1 followed by KPSH02 at 86.9ºC (Figure 7). Interestingly, only the ribose 4p compounds under the "short chain" subcategory had the greatest effect on afRioK1 stability, specifically compounds 21420, 18157, and 5062. Interestingly, compound 5062 is the only other compound that has a noticeable stabilizing effect that is in a different sub-category.

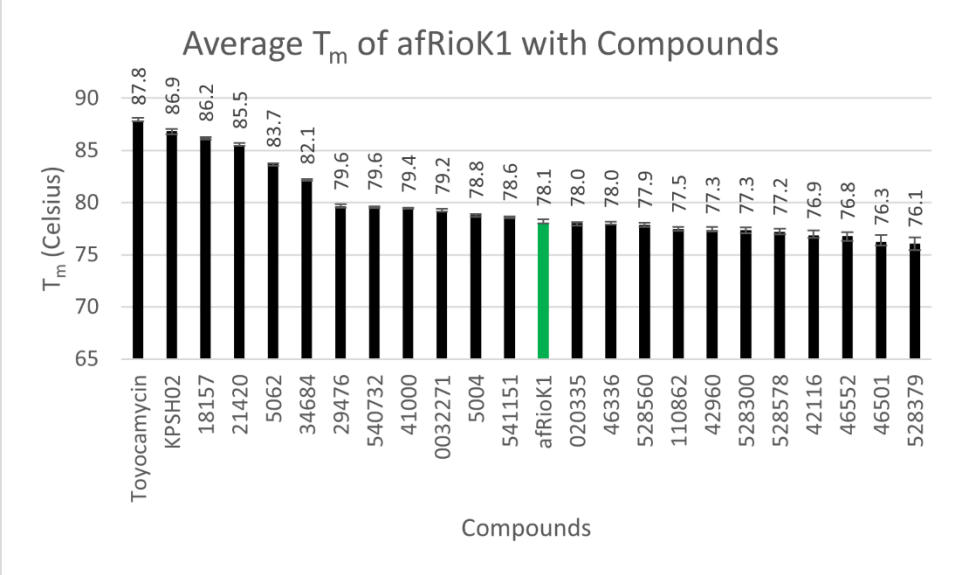

Figure 8. Thermal stability contributions from top compounds from similarity search and synthesized compound KPSH02 with afRioK1 highlighted in green.

Chapter 2.2.c. Kinase and ATPase activity Assay

To determine the inhibitory effect of the compounds on afRioK1, Kinase activity and ATPase activity of afRioK1 was monitored with the ADPase Glo assay from Promega. The assay is straightforward, by directly monitoring ADP generated from the following processes, activity of the enzyme can be determined. To determine the inhibitory effects of the compounds on afRioK1, the ATPase activity of afRioK1 was monitored with the ADPase-Glo assay from Promega. ADP generation can be measured directly from the following processes and the activity of the enzyme can be determined by monitoring luminescence output. Previous studies have indicated that afRioK1 has near zero activity when not auto phosphorylated. To address this issue, afRioK1 samples were incubated in 1 μM ATP and purified via Ni-NTA column. Due to solubility issues with some of the compounds, compounds were dissolved in DMSO; therefore, the control reaction contained the same amount of DMSO. Using a derivative of the Michaelis-Menten equation, under steady-state approximations ($V_0 = \frac{k_{cat}[E_t][S]}{K_m+[S]}$), enzyme activity ($k_{cat}$) was calculated using the previously determined K_m value for ATP (Figure 8).[7] When in the presence of either toyocamycin or KPSH02 the ATPase activity of afRioK1 is lower than the DMSO control; however, the activity overall is nearly zero regardless of the presence of inhibitors.

A

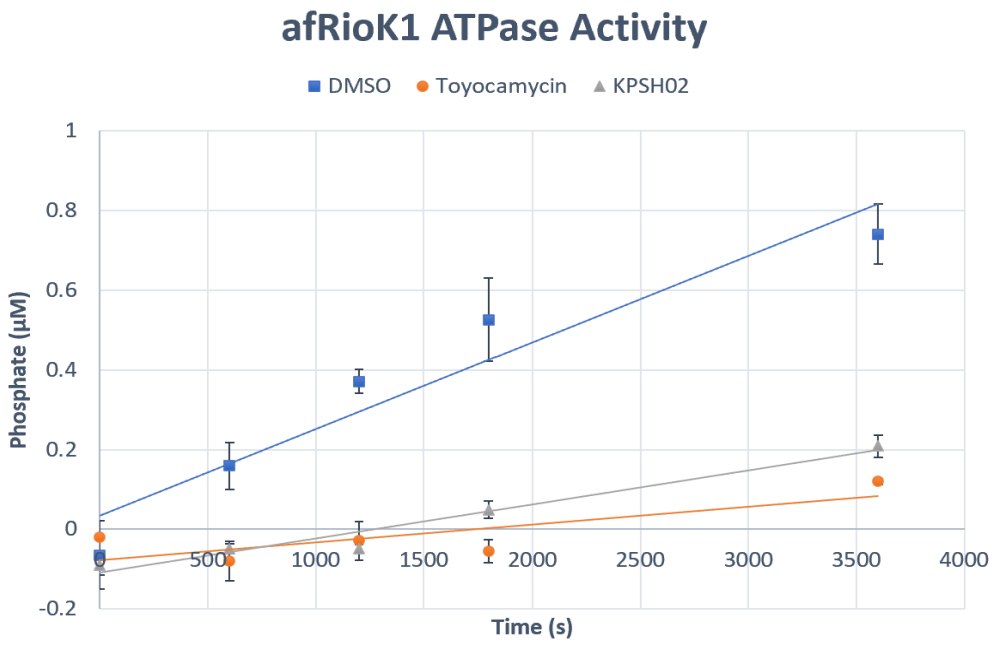

B

	DMSO	Toyocamycin	KPSH02
V_0 (µM*s^{-1})	2.17E-04	4.46E-05	8.51E-05
k_{cat} (s^{-1})	9.03E-05	1.86E-05	3.54E-05

Figure 9. KPSH02 inhibits afRiok1 similarly to Toyocamycin

(A) Plot of afRioK1 free phosphate generation over time. (B) Initial Velocity (V_0) and k_{cat} values for the enzyme in the absence (DMSO control) and presence of Toyocamycin, and KPSH02 samples.

Chapter 2.2.d. Co-crystallization of afRioK1 with KPSH02

To visualize the binding between the various compounds with afRioK1, the drugs were co-crystallized with afRioK1. The afRioK1-KPSH02 crystals diffracted at a resolution of 2.0 Å (Table 4). Molecular replacement was used to solve the phase problem, using the crystal structure of afRiok1 bound to toyocamycin (PDB: 3RE4) to provide the phases. The 3RE4 PDB file was edited so that molecular replacement and model building was done in the absence of toyocamycin, water, and any metal cations. In line with literature, the structure has a bilobed appearance with the N- and

C-terminal lobes held together by a hinge region. The compound, KPSH02, is nestled at the interface between the two lobes inside the catalytic pocket (Figure 9B). KPSH02 makes considerable hydrophobic interactions with residues Val 63, Ile 55, and Ala 78 from the N-lobe; Pro 156, Met 147, Phe 149, and Ile 150 from the hinge region; Met 203 and Ile 211 from the C-lobe (not shown). Additionally, KPSH02 contains several hydrogen bond interactions inside the catalytic pocket of afRioK1. The ribose 3' hydroxyl forms water mediated interactions with the side chain of Glu 162 and the peptidyl carbonyl of Tyr 200. The ribose 2' hydroxyl group also forms a water mediated interaction with the side chain of Glu 162 and the peptidyl carbonyl of Ala 157. One interaction of considerable interest is the hydrogen bond between the N7 cyano group and a water molecule that interacts with the side chain of Glu 120 and the peptidyl amine of Asp 212. This hydrogen bond interaction is found in all structures of afRiok1 with ATP, ADP, and toyocamycin structures.[7, 25] The primary amine off the 6'-Carbon in adenine makes hydrogen bonding contact with peptidyl carbonyl of Glu 148. The ribose 5' sulfur makes a water mediated interaction with the peptidyl amine of Asp 212. The secondary amine on the triazole side chain makes a direct hydrogen bonding interaction with the side chain of Asp 212 (Figure 9A).

DATA COLLECTION:	AFRIOK1/KPSH02
Space Group	P21
Cell Dimensions:	
a, b, c (Å)	53.3, 75.2, 60.9
α, β, γ (°)	90.0, 90.2, 90.0
Molecules/Asym. Unit	2
Wavelength (Å)	0.92009
Resolution (Å)	40.06-2.00
Refinement:	
R_{work}	1.995
R_{free}	2.609
Bond RMSD	0.14
Angles RMSD	1.532
I/σ	4.3
Completeness (%)	80.77
Redundancy	4.7
Rpim	0.103
$CC_{1/2}$	0.987
Ramachandran plot:	
Favored	95.74
Additional Allowed	4.26
Disallowed	0

Table 4. Data processing and refinement statistics for the afRioK1-KPSH02 crystal structure.

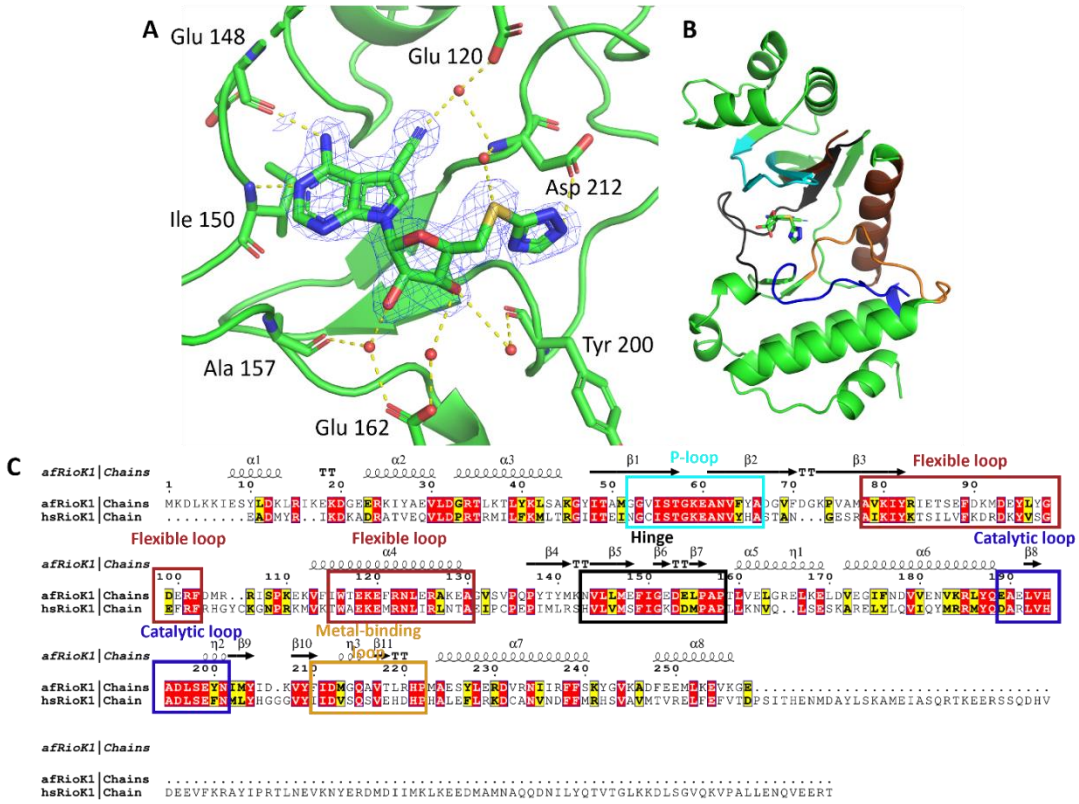

Figure 10. Structure of the afRioK1-KPSH02 complex and sequence comparison to human enzyme.

(A) Close up of the interaction KPSH02 has with afRioK1 residues overlaid with the electron density map at a contour level of 1 RMSD. (B) General structure of afRioK1 with key structures highlighted and color coded to match the multiple sequence alignment. (C) Multiple sequence alignment of our structure with that of human RioK1 (PDB:4OTP).

Early refinement cycles introducing compound KPSH02 into the active site produced three positive locations, in the omit map, where the 1,2,4-triazole ring could reside. According to the coordination and restraint files of KPSH02, by the Grade 2.0 web server, the optimal torsion angle of atoms C5, C6, S7, and C8 is -79.5º. A series of refinements was done with the triazole moiety refined at each of the three locations and the location that produced a similar dihedral angle was the metal ion binding site at -79.5º (Figure 9A). However, at this location the electron density (ED) around N1, N4 and C5 of the 1,2,4 triazole ring was not visible during standard refinement,

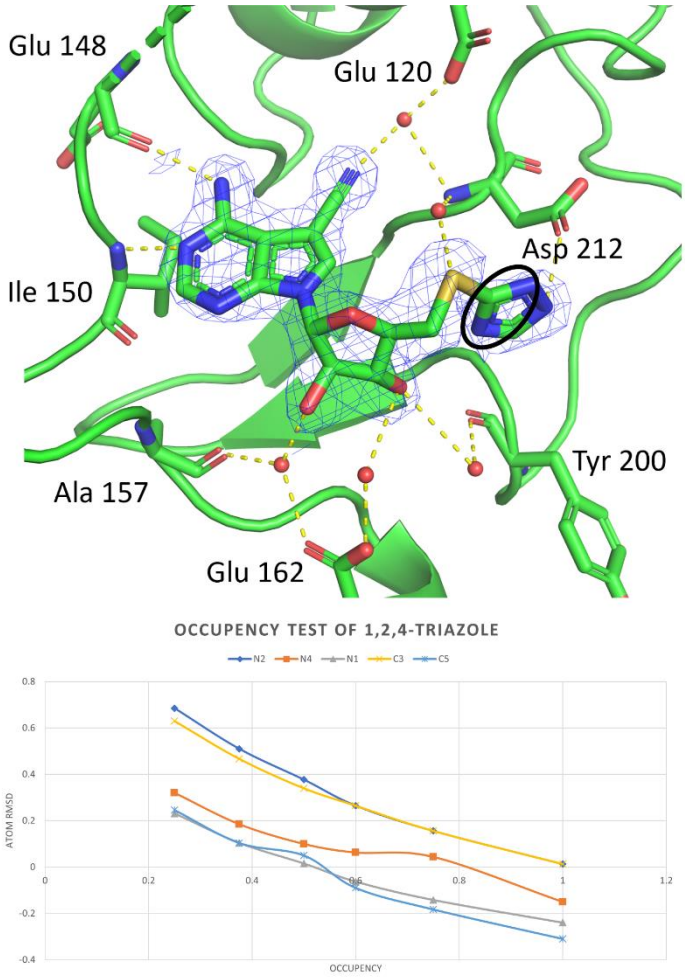

Figure 11. Occupancy test of the afRioK1-KPSH02 complex.

(A) KPSH02 located inside the active site with electron density mesh at occupancy = 1. (B) Occupancy test by analyzing RMSD values for each triazole atom at different occupancies.

occupancy equals 1 (Figure 10A). Furthermore, the B factors for N1 and C5 were high at around 50, indicating partial occupancy. To determine the occupancy of the 1,2,4-triazole ring, an occupancy test was done. A series of refinement cycles was done where each subsequent refinement cycle had the occupancy around the compound reduced and the contour levels of the omit map were adjusted to determine the RMSD of inclusion or exclusion of the atoms in questions. It was determined that

at 50% occupancy, all the atoms in the triazole ring had a positive RMSD (Figure 10B).

Chapter 2.3. Experimental Procedures

Chapter 2.3.a. Expression and Purification of afRioK1

The plasmid of full length afRioK1, containing a T7 promoter and N-terminal 6X histidine tag (His tag) followed by a tobacco etch (TEV) protease cleavage site, was acquired from GeneScript and transformed into Rosetta^{TM} DE3 pLysS *E.coli* cells (Novagen). The freshly transformed cells were plated on Luria Broth (LB) agar plates containing 100ug/mL Ampacilin and 34ug/mL Chloramphenicol and incubated, usually overnight, until the colonies were of sufficient count and size. Single colonies were picked and streaked onto a separate agar plate, identical in composition. Streaks were grown overnight to sufficient count and size. The streaks were used to inoculate 8L of freshly autoclaved LB (100ug/mL Ampicilin, 34ug/mL Chloramphenicol) that has been cooled to about 37^{o}C. Liquid cultures were incubated at 37^{o}C at 250 rpm until OD_{600} reached 0.6-0.8. At the desired OD, 1mM of Isopropyl β-D-1-thiogalactopyranoside (IPTG) was added to the culture for induction and expression of afRioK1 proceeded at 37^{o}C for 3-4 hours. Cells were centrifuged at 5,000 rpm and 4^{o}C for 25 minutes. The bacterial pellet was collected into a 50mL conical tube and stored in -80^{o}C.

Bacterial cell pellet was thawed and resuspended in 50ml of lysis buffer (per 4L bacterial pellet) containing 50mM Tris pH 8.0, 200mM NaCl, 10% Glycerol, 0.2% BME, 0.8X Bugbuster (Novagen), 0.1mg/mL DNAse (Roche), 0.1mg/mL

RNAse (Roche), a small amount of lysozyme and one pill of protease inhibitor (complete^{TM} protease inhibitor cocktail from Roche). Mixture was incubated on ice for 45 minutes at 60 rpm. Lysate was then spun down at 13k rpm in 4^{o}C for 50 minutes. Supernatant was filtered using a 0.22 um sterile syringe filter and loaded (1ml/min) onto a 5ml HiTrap HP Column (Cytivia, formerly GE Healthcare), that was pre equilibrated with 5 column volumes (CVs) of afRioK1 buffer (AFRB, 50mM Tris, pH 8.0, 150mM NaCl, 0.2% βME and 10mM $MgCl_2$). His-tagged afRioK1 was eluted using AFRB + 1M Imidazole (EB, elution buffer) using the following protocol at 4ml/min flowrate: 5CV of 100% AFRB, 5CV to adjust to 80 AFRB and 20% EB, 10CV of 80% AFRB and 20% EB, 5CV to adjust to 0% AFRB to 100% EB, 10CV of 100% EB lastly followed by 10CV of 100% AFRB. Fractions were collected for the entire elution process and each fraction contained 4ml of afRioK1 elution sample. According to the UV/Vis readout, samples were pooled together and reloaded into the 5ml HiTrap Column for a second round of His-tag purification following the same elution protocol. Second round His-trap fraction were collected and dialyzed overnight in 3L of AFRB with TEV protease at 4^{o}C using 10k MWCO dialysis tubing.

The following day the pooled fraction was loaded onto a pre-equilibrated HiTrap Column to elute out TEV cleaved afRioK1. TEV-cleaved afRioK1 was then concentrated to 5ml, careful to not exceed 15mg/ml, and loaded onto Superdex^{TM} 200 column, pre-equilibrated with AFRB, for SEC purification. The protein was eluted with a 1ml/min flowrate and fractions were monitored with SDS-PAGE to check for purity.

Chapter 2.3.b. SILCS Simulation

The current SILCS run was performed using the Grand Canonical Monte Carlo (GCMC)/MD protocol for SILCS.[88] The crystal structure of RioK1 (PDB entry 4otp) was used to initialize the SILCS simulation with removal of crystal ligands. The protein was solved in a water box, the size of which is determined to have the protein extrema separated from the box edge by 12 Å on all sides. Eight representative solutes with different chemical functionalities (benzene, propane, acetaldehyde, methanol, formamide, imidazole, acetate, and methylammonium) were added into the system at ~0.25 M concentration, to probe the functional group requirements of the protein.

Ten such systems with different fragment positions were created to expedite the convergence of the simulations. Each system was minimized for 5000 steps with the steepest descent algorithm in the presence of periodic boundary conditions and was followed by a 250 ps MD equilibration. During SILCS simulations, weak restraints were applied on the backbone Cα carbon atoms with a force constant (k in $1/2\ k\delta x^2$) of 0.12 kcal/mol/Å to limit large conformational changes in the protein and to prevent the rotation of the protein in the simulation box. CHARMM36 protein force field, CHARMM General Force Field (CGenFF) and modified TIP3P water model were used to describe protein, fragments, and water during the simulation, respectively.[20, 89-91] GCMC was performed by an in-house code and MD was conducted using the GROMACS program.[92] Ten GCMC/MD simulations were run for 100 cycles where each cycle has 200,000 steps of GCMC and 0.5 ns of MD, yielding a cumulative 200 million steps of GCMC and 500 ns of MD.

3D probability distributions of the selected atoms from the small molecules, called “FragMaps”, from the SILCS simulations were constructed and combined to obtain both specific and generic FragMap types as previously described.[93] Atoms from snapshots output every 10 ps from each SILCS simulation trajectory were binned into 1 Å × 1 Å × 1 Å cubic volume elements (voxels) of a grid spanning the entire system to acquire the voxel occupancy for each FragMap atom type being counted. The voxel occupancies computed in the presence of the protein were normalized and converted to grid free energy (GFE) based on a Boltzmann transformation for quantitative use.[93]

Monte Carlo (MC) sampling using SILCS FragMaps (SILCS-MC was performed to dock adenosine analogs from the similarity searches and predict their binding energies to RioK1.[93] 3D structures of all adenosine analogs were prepared using the MOE software with their dominant protonation states being determined at PH 7.0 condition. Conformations of all adenosine analogs were randomized at the ADP binding site of RioK1 initially and energy minimized before MC sampling. SILCS-MC was conducted in the exhaustive sampling mode that each cycle involves 10,000 steps of MC followed by simulated annealing (SA) from 300 to 0 K over 40,000 MC steps.[22] Five independent simulations were conducted for each molecule up to 250 MC-SA cycles. For every 50 MC-SA cycles, convergence criterion of 0.5 kcal/mol difference among the top three most favorable LGFE values was checked for termination purpose. The best LGFE for each adenosine analog was obtained from the SILCS-MC runs for final compound ranking.

Chapter 2.3.c. Thermal Shift Assay

Purified afRio1 was used to perform the thermal shift assay using a ViiA 7 Real-time PCR system. Protein unfolding was monitored using the fluorescent SYPRO® Orange dye (5000X), from Sigma Aldrich. Each well contained 0.3mg/ml of afRioK1 in afRioK1 buffer (AFRB), 50mM Tris pH 8.00, 200mM NaCl, 1mM MgCl2, 0.2% BME and 5X dye. Compounds were added into each protein sample from yielding a final concentration of 1mM in 2% (v/v) DMSO. Reactions were incubated for 1hr at rt for afRioK1. The fluorescence intensity data was acquired with excitation and emission wavelengths of 470 and 570nm, respectively. The change in fluorescence was monitored as the temperature increased from 4^{o}C to 99°C at a rate of 0.02°C per second, with an initial equilibration step to get the microwell plate to 4^{o}C. Raw data was fit to an algorithm using Nelder-Mead optimization to minimize the influence of a nonlinear baseline, Tm's were determined from this fit. All measurements were carried out in triplicate and the average Tm values, the inflection points of the sigmoidal denaturation curves, were reported with standard deviation and Z-score relative to the lead parent compound Toyocamycin.

Chapter 2.3.c. afRioK1 Co-crystallizations with Adenosine-like Compounds

To determine the interactions between afRioK1 and adenosine-like compounds, afRioK1 was expressed and purified as previously explained and concentrated to 10mg/ml for crystallography. High-throughput screens were used to screen for potential crystal conditions, using the sitting drop method. The Morpheus® screen from Molecular Dimensions yielded a consistent afRioK1 crystal with

formulation A1 (MDSR-46-1-1; 0.06 M Divalents ($MgCl_2$/$CaCl_2$), 0.1M Buffer system 1 (Imidazole and MES monohydrate), pH 6.5 and 30% (v/v) Precipitant mix 1 (40% v/v PEG 500 MME, 20% w/v PEG 20000). Crystallography afRioK1 samples were prepared by mixing afRioK1 (10mg/ml) with drug compounds (1-2mM) for 1 hour at room temp and all crystal trays were set up using Mosquito® LCP from SPT Labtech using different ratios of afRioK1/drug samples with mother liquor at 1:2, 1:1 and 2:1, respectively. Trays were incubated at room temperature and monitored periodically with a light microscope for crystal growth.

Chapter 3. Characterization of the RioK1-PRMT5 Complex

Chapter 3.1. Introduction

The enzyme family of arginine methyltransferases have several types, which plays pivotal roles in cellular biology by facilitating methyl transfer onto arginine residues of substrate proteins. The catalytic activity of PRMT5 is mostly recognized as a component of the methylosome, an intricate ensemble comprising of PRMT5, MEP50, and an assortment of adapter proteins, responsible for the recruitment of diverse substrate proteins to the active site of PRMT5 for arginine methylation. Among the recognized adapter proteins are pICln (responsible for Sm protein recruitment), CopR5/Menin (associated with histones), and RioK1 (facilitating nucleolin and other substrates).[65, 68, 94] Importantly, these adapter proteins vie for binding to PRMT5's N-terminal domain, a competitive process that governs the selective recruitment of distinct substrates.[64, 68, 75] As a consequence, the PRMT5-MEP50 core complex is subjected to regulatory mechanisms that ensure the precise methylation of various substrates, including histones, splicing Sm proteins, and Nucleolin, among others.

PRMT5 is classified as a type II arginine methyltransferase, possessing the ability to monomethylate or symmetrically dimethylate substrates, and this catalytic activity is conserved across all eukaryotic species for which data is accessible. Dysregulation of PRMT5 or the methylation process has been implicated in various cancer-related phenotypes.[72-75] Despite current literature on PRMT5, there remains a substantial need to characterize its structural attributes. A deeper understanding of its

mechanism of action could potentially open avenues for its application in cancer therapeutics.

To date, several structural investigations have provided insights into PRMT5, originating from humans, C. elegans, and X. laevis.[67, 95, 96] In the C. elegans structure, PRMT5 assumes a dimeric configuration, whereas it adopts a tetrameric form in both the Xenopus and human structures. Within these tetrameric complexes, PRMT5 is invariably bound to MEP50 in a 1:1 stoichiometric ratio, indicating the MEP50 component has an indispensable role as a co-factor in the PRMT5 complex. Experimental studies have underscored the need of MEP50 for PRMT5 to exhibit appreciable methyltransferase activity.[67, 95] Current structural data reveal a conservation of tertiary and quaternary architecture, notably within the TIM barrel, which is responsible for MEP50 binding, and the catalytic Rossman fold, which facilitates substrate interaction. While one half of the tetrameric assembly in the human and Xenopus structures exhibits homology to the C. elegans dimeric form, it's worth noting that structures of the PRMT5 homolog (Hsl-7) from yeast remain elusive, and S. cerevisiae lacks a homolog of MEP50.

In the yeast counterpart of PRMT5, known as histone synthetic lethal 7 or Hsl7, its discovery emerged from a screen for synthetic lethality in the presence of mutated histones. Notably, despite its apparent inability to catalyze GST-GAR or bovine brain myelin methylation in vitro, Hsl7 has demonstrated its capacity for in vitro mono- and di-methylation utilizing calf thymus histones H2A.[97, 98] Recent research has elucidated Hsl7's capability to induce symmetric di-methylation of histone H4 arginine 3 in vivo, a modification intricately linked to transcriptional

repression.[99] These findings further suggest a conserved catalytic activity shared with its human homolog. In a cellular context, the active form of Cyclin B-associated Cdc28, required for the transition from G2 to M phase, undergoes inhibition via phosphorylation of Tyr19 in cDc28 by Swe1. Hsl7 plays a pivotal role by recruiting Swe1 to Hsl1 (histone synthetic lethal 1) for phosphorylation, which subsequently downregulates Swe1, thereby alleviating the inhibition of Clb-bound Cdc28 and facilitating G2-M transition.[100] In Xenopus laevis, the Hsl7 homolog appears to be implicated in the control of DNA replication checkpoints, underscoring the versatility of the Hsl7-Swe1/Hsl7-Wee1 module in responding to various checkpoint signals across different organisms.[101]

Chaetomium thermophilum, a thermophilic fungus that has a PRMT5 homolog (ctPRMT5) that shares substantial sequence and structural similarity with the human homolog. In this study, we present the crystallographic elucidation of the ctPRMT5 structure, obtained through X-ray crystallography techniques, adding a critical piece to the puzzle of PRMT5 structural diversity and evolutionary adaptation.

Chapter 3.2. Results and Discussion

Chapter 3.2.a. Overall Structure of ctPRMT5

Largely based on the work done by fellow colleague Hongpeng Wang, characterization of the RioK1-PRMT5 complex, started with crystallizing full length ctPRMT5 at 2.4 Å resolution. This structural analysis reveals the assembly of ctPRMT5 as a tetrameric unit, consisting of two dimers. Within this assembly, a single asymmetric unit comprises a dimer, comprising of a Chain A and Chain B monomers, and the complete ctPRMT5 tetramer arises from the association of these

two dimers (Figures 11, 12). Within the structure there exists regions of disorder, in Chain A, residues 1-10 at the N terminal end and residue 786-793 at the C-terminal end are disordered. Furthermore, within chain A, there are 3 gaps of disorder: residues 203-225, 326-354, 393-409. Chain B with slightly different regions of disorder: residue 1-13, 203-226, 326-354, 392-408,787-793.

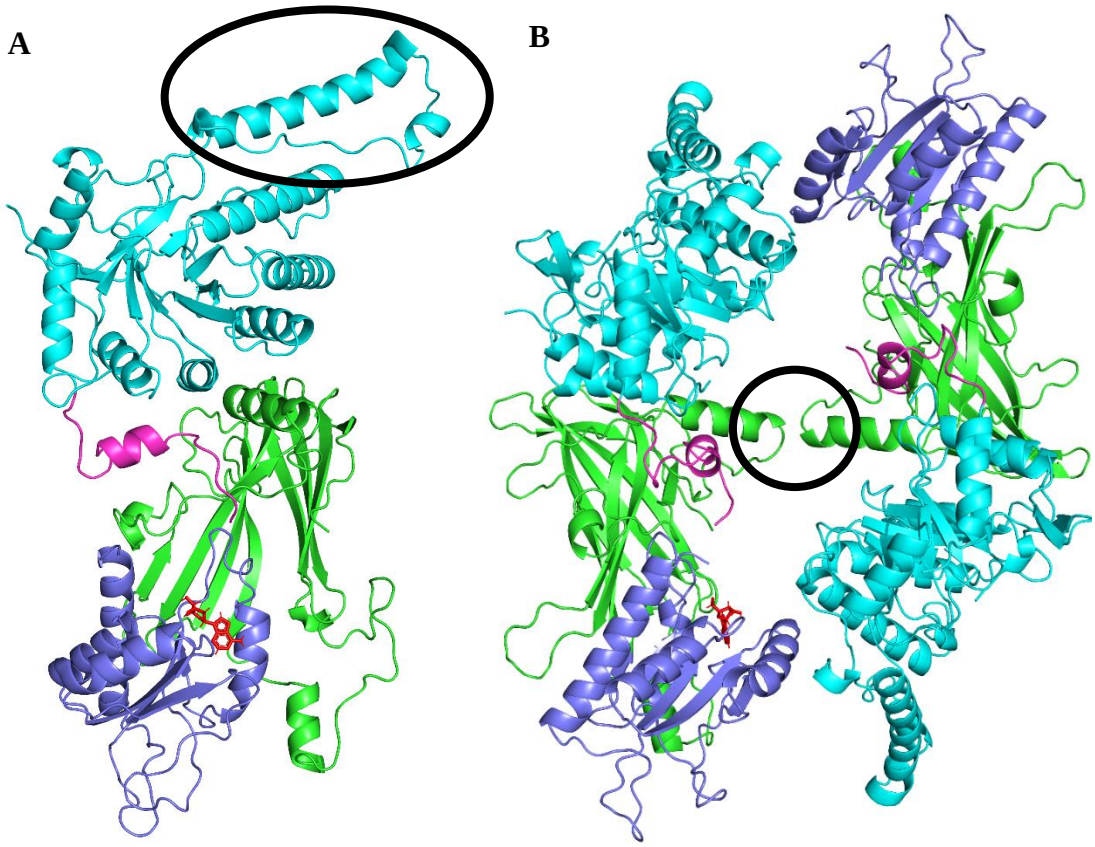

Figure 12. Structure of ctPRMT5.

Note. (A) One protomer of the ctPRMT5 tetramer with key domains highlighted: (Cyan) TIM barrel domain, (Magenta) N-terminal-to-C-terminal linker, (Green) Beta sandwich, (Purple) Rossman fold and (Red) adenosine. (B) ctPRMt5 dimer where the monomer (A) is rotated about the y-axis by 90^{o} to show the dimerization arm interface (circled) and the head-to-tail assembly.

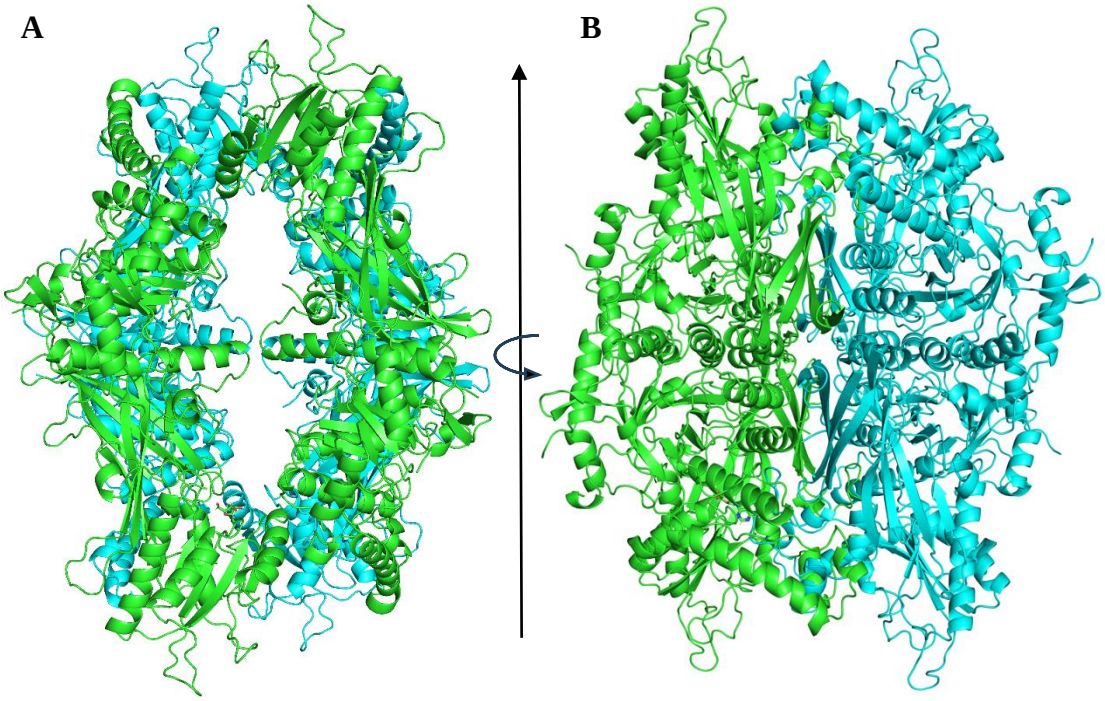

Figure 13. Structure of tetrameric ctPRMT5.

Note. (A) View of ctPRMT5 tetramer that displaying the hollow cavity of the protein with dimerization arms from both dimers (Green and Blue). (B) Rotating the view from A by 90^{o} displays the tetramer interface between the two dimers.

In the asymmetric unit, two subunits are observed to interact with each other in a head-to-tail fashion, with the N-terminal TIM barrel domain engaging with the C-terminal Rossman fold. (Figure 11A). Additionally, the β-sandwich domain, situated between two monomers, further strengthens their association via dimerization arm interactions (Figure 11B). In total, the dimeric interaction between Chain A and Chain B results in a substantial buried surface area measuring 1147.5 Å2 which includes 4 unique hydrogen bond interactions and 2 unique salt bridges. Further enhancing the assembly, an array of 11 unique hydrogen bonds 3 unique salt bridge

interactions emerge at the interface between Chain A and Chain C within the tetramer, encapsulating a buried surface area spanning 3134.5 Å2 (Table 5).

While the ctPRMT5 structure contains a lot of the key features present in other PRMT5 orthologs, there are some clear differences that set ctPRMT5 apart. PRMT5 needs to be able to dimerize to be functional and typically this is done by TIM barrel interactions of one monomer with the Rossman fold of the other monomer, but also with the dimerization arms of each monomer forming salt bridges between the dimer protomers.[67, 95, 102] However, the key residues in dimerization arm salt bridge formation, Lys and Asp, are replaced with Thr and Gly, respectively. Lack of this key salt bridge could be offset by the extension of one of the α-helices (circled in Figure 11A) in the TIM barrel. In hsPRMT5 (PDB: 4GQB), α2 is not a helix, but a random coil. This helix is unique to ctPRMT5 and creates significant tetrameric interactions not seen in other orthologs, notably a small pocket of hydrophobicity created by W72 and L78 of chain A and V629 in chain C.

Tetramer Interface Hydrogen Bonds		
Chain A	**Distance (Å)**	**Chain C**
Arg 631	1.92	Glu 68
Arg665	2.08	Ser 87
Arg654	2.01	Glu 175
Asn 85	2.13	Val 624
Arg 76	2.14	Asp 634
Arg 76	1.6	Asp 634
Thr 95	2.32	Gly 648
Asn 138	2.27	Gly 651
Asn 138	2.27	Ala 652
Ser 87	3.16	His 662
Arg 171	1.94	Glu 756

Tetramer Interface Salt Bridges		
Chain A	**Distance (Å)**	**Chain C**
Arg 631	3.5	Glu 68
Arg 76	2.8	Asp 634
Arg 171	3.1	Glu 756

Dimer Interface Hydrogen Bonds		
Chain A	**Distance (Å)**	**Chain B**
Lys 493	2.02	Asp 98
Arg 490	2.00	Thr 101
Thr 101	1.90	Arg 490
Leu 103	2.39	Arg 490

Dimer Interface Salt Bridges		
Chain A	**Distance (Å)**	**Chain B**
Lys 493	3.64	Asp 98
Arg 493	2.89	Asp 98

Table 5. Table of all unique hydrogen bonds and salt bridge interactions in the Dimer and Tetrameric interfaces.

A closer look at the catalytic pocket, ctPRMT5 contains the conserved catalytic double-E loop, E531 and E540. The residues are essential in the alignment of target substrate arginine's. In the case of ctPRMT5, the E531 side chain adopts a different rotamer conformation, burying itself deeper into the Rossman fold away from catalytic pocket, compared to the human homolog the distance shifted by the carboxy group carbon is about 4.4Å. In support of this, ctPRMT5 was co-crystallized in the presence of SAM and H4 peptide. Interestingly, in the active site the missing electron density was observed. SAM was fit into the missing density in the subsequent rounds of refinement; however, lack of density for most of SAM indicated SAM was only partially occupying the active site in our structure. Instead, adenosine was fit into the missing ED and a series of refinements was performed by changing

the local occupancy of the active site, to see if the subsequent omit maps highlighted any positive density that would fit SAM. The lowest local occupancy refinement was done at 0.1, and no extra density was observed that could accommodate SAM. In hsPRMT5, the COOH- group of SAM is stabilized by direct interaction with K333 and Y334 and water-mediated interactions with R368 and E328. The ctPRMT5 equivalent of E328 in humans, is E406. However, residues 390-406 are absent from the ctPRMT5 structure and within this stretch of residues lies a key phenylalanine residue responsible for directing dimethylation.[95] In the absence of a proper peptide and co-factor, this stretch of residues may have a degree of flexibility, which could explain the absence of density in the ED map and why E531 of the double E-loop in ctPRMT5 is in a different conformation.

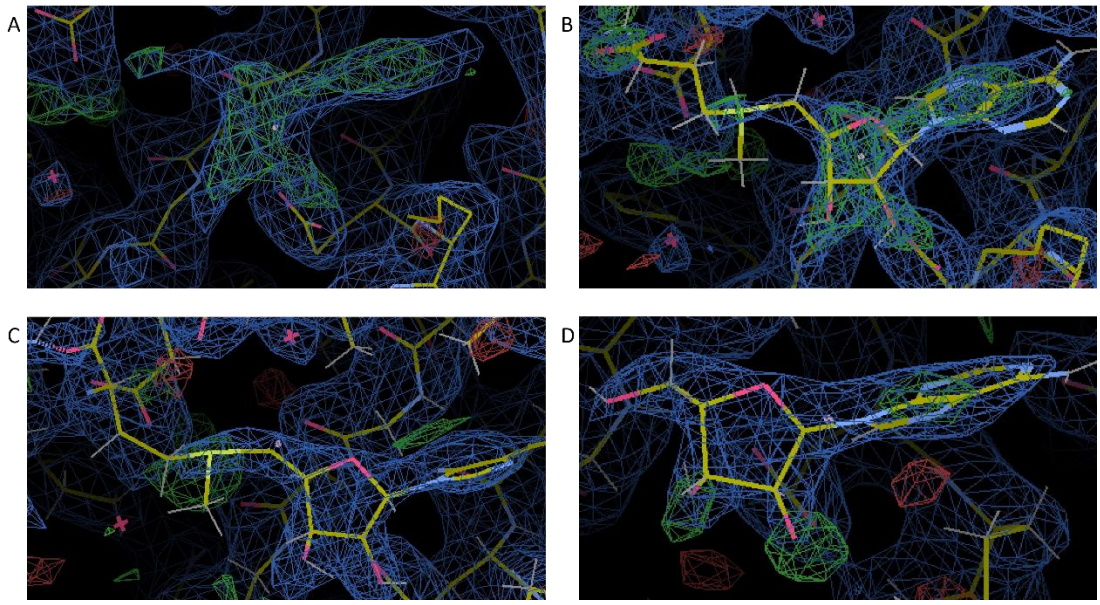

Figure 14. Real space refinement of the active site of ctPRMT5.

Note. (A) Initial ED map of ctPRMT5 with missing density vaguely resembling adenosine. (B) SAM was inserted into the missing density where most of the adenosine moiety of SAM fit nicely. (C) Refinement with SAM in the missing density from (A) did not improve the local ED map. (D) Refinement done with adenosine resulted in lowered r-values and local b-factors.

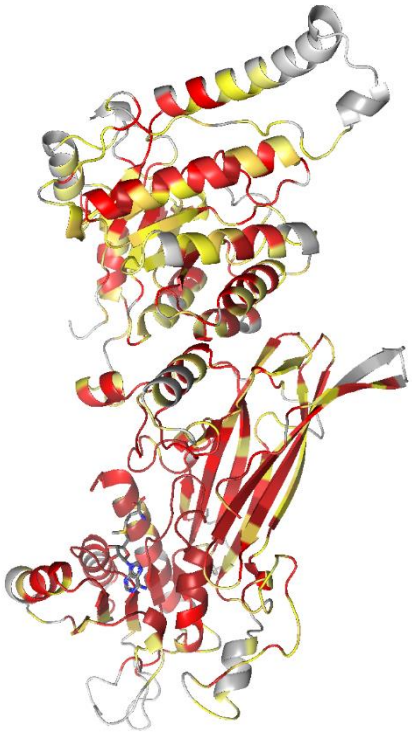

Figure 15. Structure of ctPRMT5 monomer with consurf overlay.

Note. The consurf overlay is color-coded by conservativity of over 600 fungal species. With red regions indicated high conservativity, yellow, moderate conservativity, and white with little to no conservativity.

Chapter 3.2.b. Conservation of Residues Within the Yeast Sequences

The structural homogeneity observed in ctPRMT5 across other PRMT5 orthologs underscores a high degree of conservation within this protein family. A series of multiple sequence alignments (MSA) was performed. Figure 14 encompasses a consurf map of ctPRMT5 using an MSA of over 600 diverse fungal species, and the results revealed a noteworthy preservation of the β-sandwich region (residues 551-783) and high conservativity of the catalytic Rossman fold (residues 388-550). In contrast, the TIM Barrel domain (residues 11-370) exhibited a moderate

level of conservation, as illustrated in the multiple sequence alignment featuring 11 different fungi species (Figure 15).

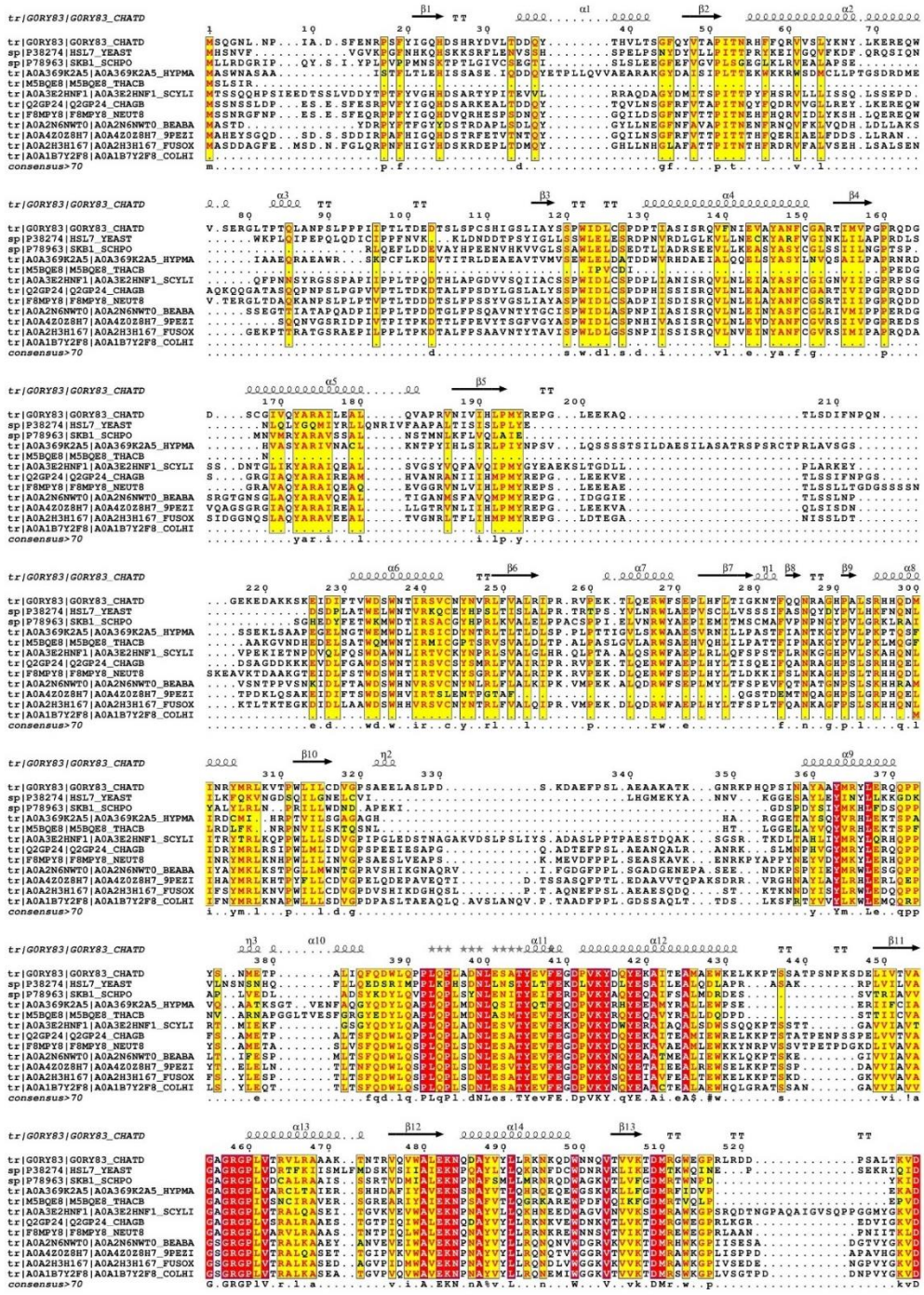

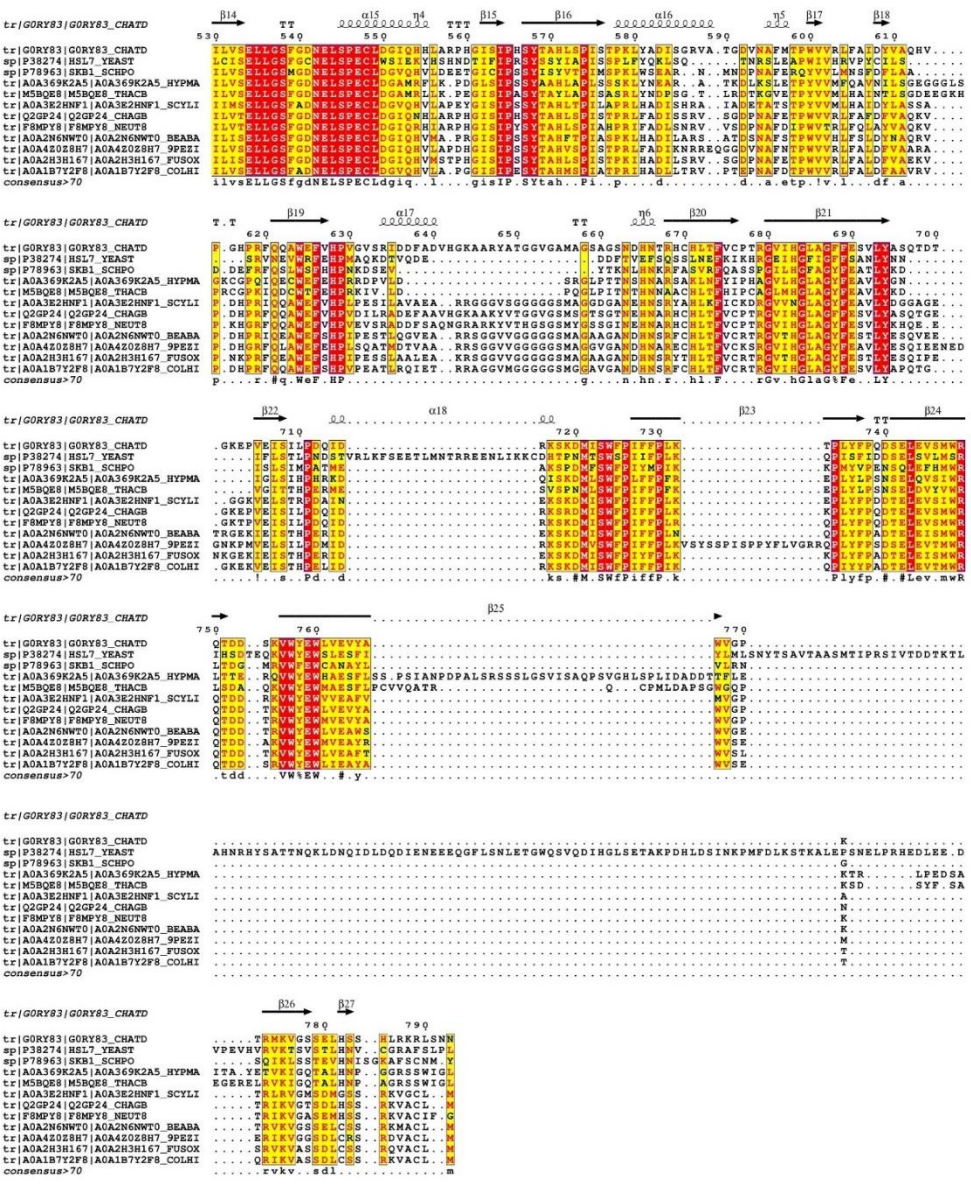

Figure 16. Multiple sequence alignment of ctPRMT5 against 11 other fungal homologs.

Note. From top to bottom the Uniprot entry and associated origin species is as follows: G0RY83 (Chaetomium thermophilum), P38274 (Yeast), P78963 (Schizosaccharomyces pombe), A0A369K2A5 (Hypsizygus marmoreus), M5BQE8 (Thanatephorus cucumeris), A0A3E2HNF1 (Scytalidium lignicola), Q2GP24 (Chaetomium globosum), F8MPY8 (Neurospora tetrasperma), A0A2N6NWT0 (Baeuveria bassiana), A0A4Z0Z8H7 (Xylaria hypoxylon), A0A2H3H167 (Fusarium xysporum), A0A1B7Y2F8 (Colletotrichum higginsianum). MSA uses the secondary structure of ctPRMT5 for the analysis, highly conserved residues are highlighted in red, followed by semi-conserved residues in yellow.

A distinguishing hallmark of the PRMT5 dimer structure lies within the dimerization arms (residues 574-597). Despite their presence in other PRMT5 crystallographic structures, these dimerization arms exhibited only a moderate level of conservation among fungal PRMT5 variants. Notably, prior crystal structures (i.e., 6CKC, 4G56, 3UA3) documented the formation of a dual salt bridge between conserved arginine and aspartic acid residues within the dimerization arms; however, in ctPRMT5 these specified residues are replaced with a threonine and glycine, respectively. It has been reported that the dimerization arms across different species do exhibit a small degree of variability, and it appears this trend holds true to fungi as well.

Expanding the conservation of structure to include other species, aside from fungi, the results remain relatively unchanged. There continues to be a moderate preservation of the β-sandwich region (residues 551-783) and a high conservativity of the catalytic Rossman fold (residues 388-550). Whereas the TIM barrel domain (residues 11-370) was still observed to have a moderate level of conservation. The moderate level of N-terminal conservation corroborates the fact that many PRMT's contain non-catalytic N-terminal domains that act as adaptors or co-factors in aiding in the activity of the enzyme (Figure 16).[102, 103]

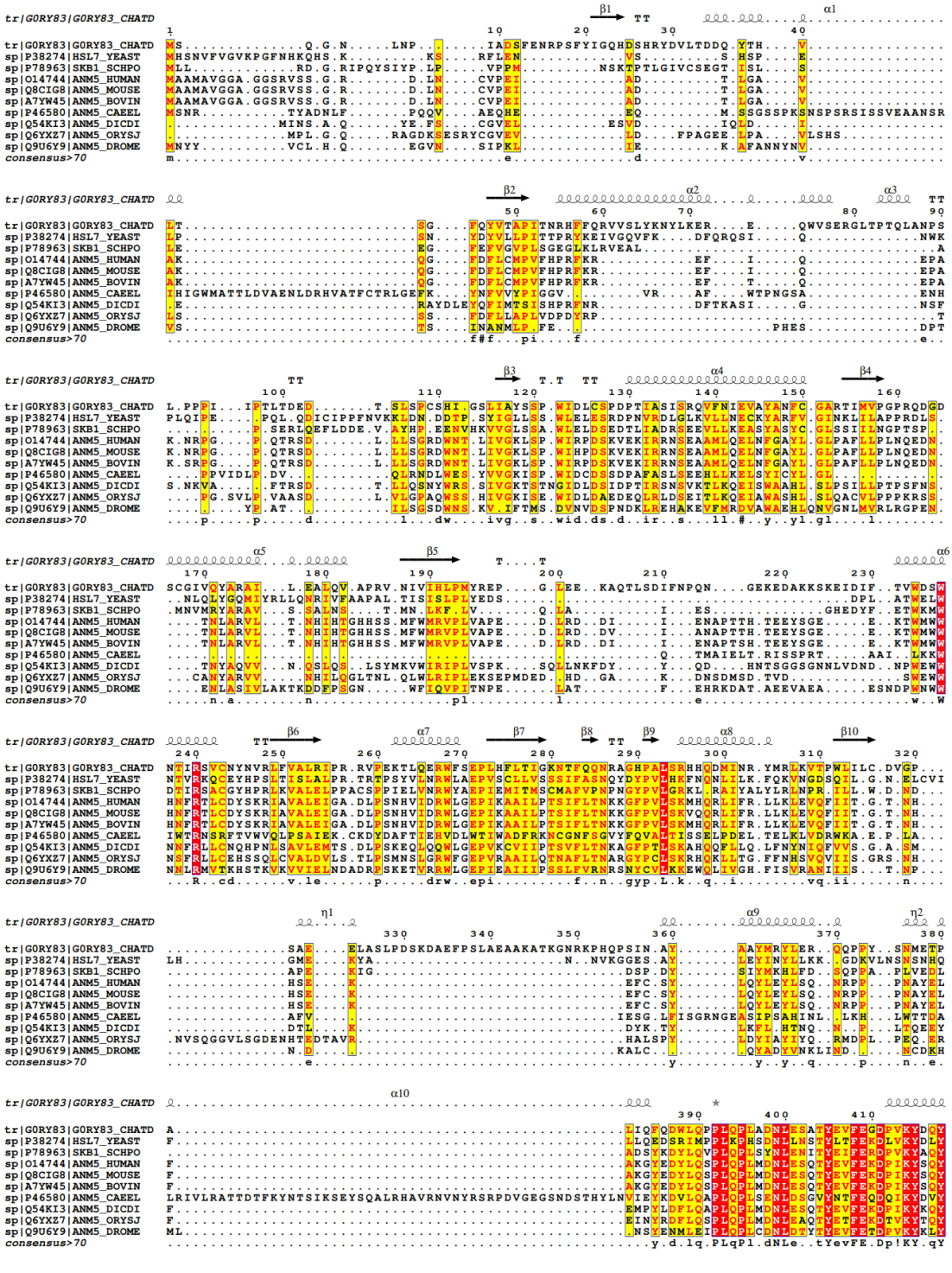

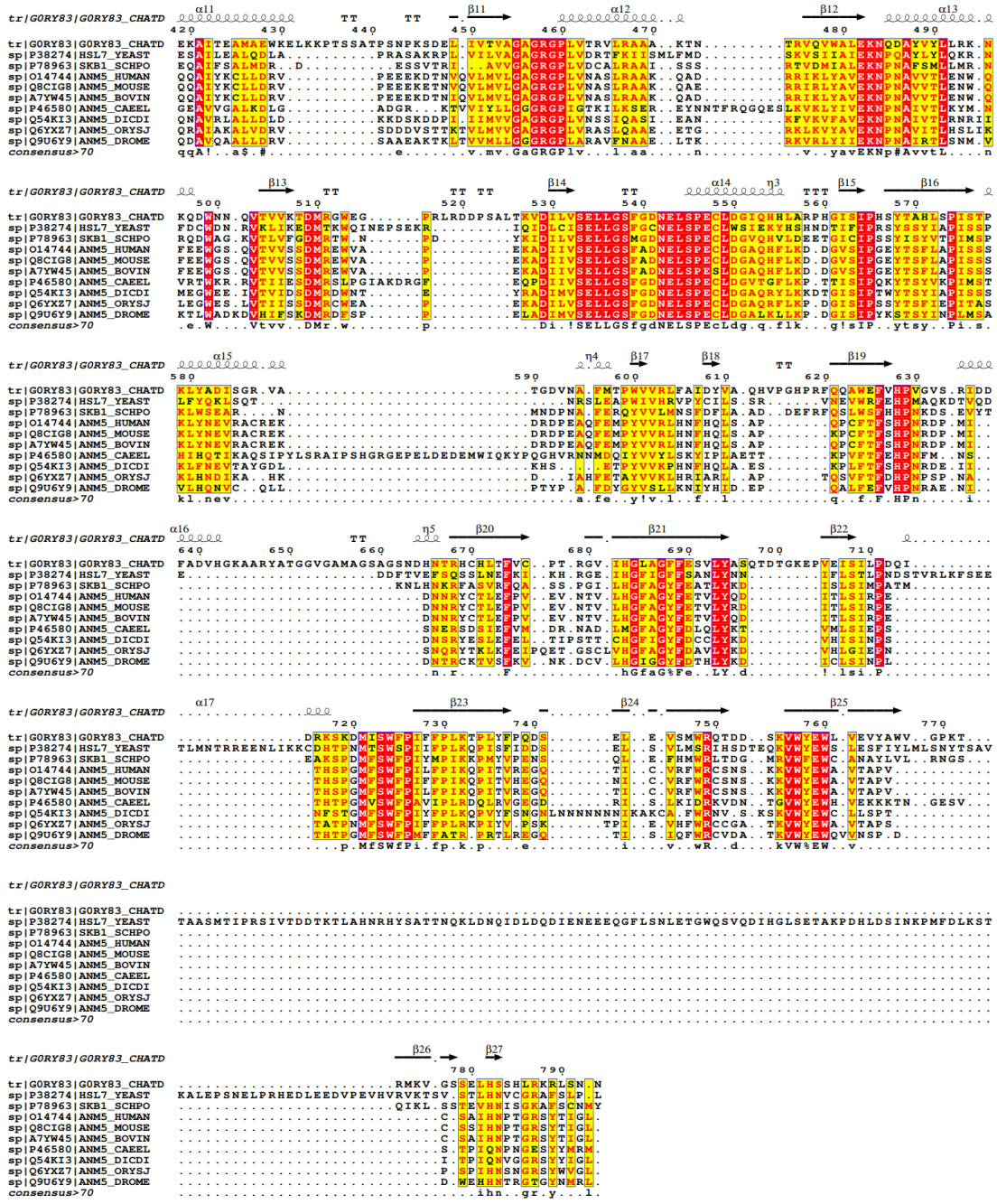

Figure 17. Multiple sequence alignment of ctPRMT5 against 9 other species.

Note. From top to bottom the Uniprot entry and associated origin species is as follows: G0RY83 (*C. thermophilum*), P38274 (Yeast), P78963 (*Schizosaccharomyces pombe*), O14744 (*H. sapiens*), Q8CIG8 (*M. musculus*), A7YW45 (*B. taurus*), P46580 (*C. elegans*), Q54KI3 (*D. discoideum*), Q6YXZ7 (*Oryza sativa subsp. Japonica*), Q9U6Y9 (*D. melanogaster*). MSA uses the secondary structure of ctPRMT5 for the analysis, highly conserved residues are highlighted in red, followed by semi-conserved residues in yellow.

The core structure of PRMT's have remained relatively unchanged throughout different species consisting of a N-terminal TIM barrel domain and a C-terminal Rossman fold containing a dimerization arm that interacts with another PRMT monomer in a head-to-tail fashion. Where the structural conservativity diverges at the N-terminal TIM barrel domain, here each type of PRMT may have minute changes to allow proper interactions for dimerization of substrate recognition. *C. Thermophilum* not only lacks an obligatory MEP50 adaptor protein homolog, but the dimerization residues change from K586G and D587T. Formation of the salt bridge formation within the dimerization arms and $\alpha 2$ withdrawing back into the TIM barrel for proper MEP50 interaction may be how higher order species have adapted to facilitate more efficient substrate binding and methyltransferase activity.

Chapter 3.2.c. Catalytic Activity of ctPRMT5

To assess the effects RioK1 had on PRMT5 methyltransferase activity in yeast, an investigation into the methylation activity of ctPRMT5 was performed using fluorometric detection of methyl transfer by-product, s-adenosylhomocysteine (SAH) generation. The primary objective was to ascertain the enzymatic activity of ctPRMT5 in the presence/absence of RioK1 and to see if ATP facilitated methyl transfer. The secondary objective was to determine if ctPRMT5 possessed the capacity for dimethylation, a characteristic commonly associated with type II PRMTs. To accomplish this, a coupled enzyme assay that capitalizes on the by-product of SAM methylation, SAH, that undergoes rapid conversion to resorufin. Measurement of resorufin production was conducted by exciting the sample at a wavelength of 530-

540nm and monitoring the emitted light at 585-595nm and SAH production was calculated using a resorufin standard curve.

SAH production was observed at two different concentrations of ctPRMT5, 1.5 µM and 4.5 µM and at two different ratios of ctRioK1 at a 1:1 or 2:1, ctRioK1 to ctPRMT5, respectively. Experiments were done under saturating conditions of SAM and H4 peptide. Notably, SAH production is dose dependent on ctPRMT5 and not affected by the addition of ctRioK1 (Figure 17). Interestingly, a discernible increase in methyltransferase activity was observed when ATP was added to the system, but only when in the absence of ctRioK1. Subsequent investigations are warranted to elucidate the underlying cause of this non-linearity.

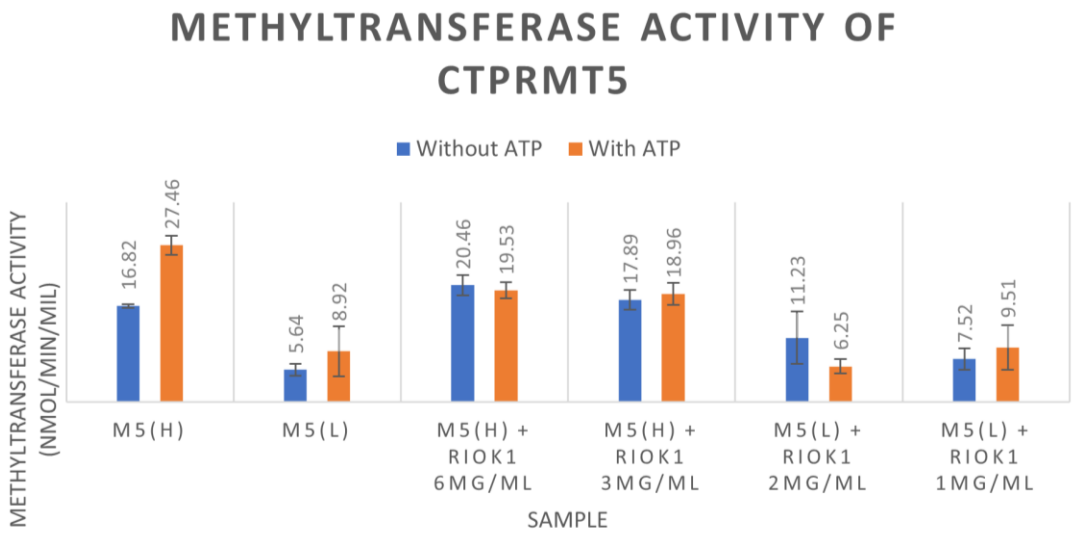

Figure 18. Methyltransferase activity of ctPRMT5.

Note. Methyltransferase activity was determined using High (4.5 µM, H) and Low (1.5µM, L) concentrations ctPRMT5 (M5) with ctRioK1 added at a 1:1 or 2:1 ratio, under saturating conditions of SAM and H4 peptide. Experiment was done in the presence or absence of ATP to determine the effects on ctPRMT5 methyltransferase activity. SAH production increase with ctPRTM5 concentration in a dose-dependent manner.

PRMT5, is classified as a type II methyltransferase with the capability for mono- and di-methylation, and we wanted to see if the *c. thermophilum* ortholog was capable of dimethylation as well. ctPRMT5 was subjected to an incubation period with SAM and H4 peptide under saturating conditions for a duration of 3 hours, and matrix-assisted laser desorption/ionization mass spectrometry (MALDI) was used to analyze methylation. A sample containing pure H4 peptide was used as a control to determine if MALDI could accurately detect its molecular weight at 2465 Da (Figure 18A). The magnified results from MALDI indicated the presence of a significant peak at 2465 m/z and 2480 m/z, signifying successful mono-methylation (Figure 18B, 18C). However, notably absent from the results was a peak at 2495 m/z, which would have indicated the occurrence of dimethylation. According to existing literature references (e.g., Antonysamy, S. et al.), dimethylation is typically observed after the concentration of monomethylated peptide surpasses that of the non-methylated counterpart. In Figure 17C, it is evident that this state was not attained, further underscoring the absence of dimethylation activity in ctPRMT5.

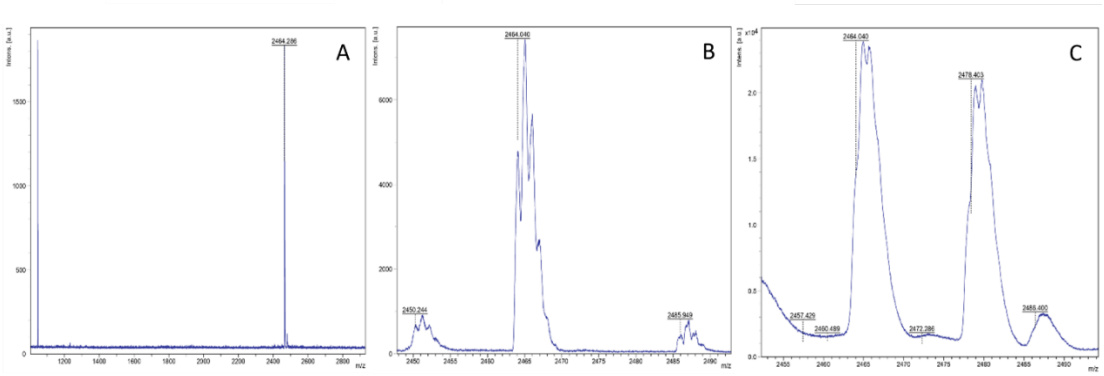

Figure 19. Mass Spectra of ctPRMT5 monomethylation.

Note. (A) MALDI-MS spectrogram of H4 peptide, with peak at 2464 m/z matching the MW of the H4 peptide. (B) MADLI-MS spectrogram of time point 0 for a 3-hour incubation with ctPRMT5, SAM, and H4 peptide with a clear peptide peak at 2464 m/z. (C) MALDI-MS spectrograph at the end of a 3-hour incubation period with a clear H4 peptide peak at 2464 and a monomethylation peak 2479 m/z. Peak heights are roughly 1:1 for native and monomethylated peptide, respectively, conditions for demethylation were not reached.

Chapter 3.3. Methods

Chapter 3.3.a. Cloning and Purification of PRMT5

The proteins were expressed employing a pET-28α (+) vector, which featured an N-terminal His-Tag, a T7 promoter, and a lac operon. In this process, a mixture containing the ctPRMT5 plasmid (at a concentration of 10 ng/µl) was heat shocked at 42°C for 60 seconds. Following this, 500 µl of Luria-Bertani (LB) medium was added, and the mixture was allowed to cool on ice for 5 minutes before being incubated at 37°C with agitation at 250 rpm. Subsequently, 100 µl of this mixture was spread onto an LB agar plate with resistance to Kanamycin (50 µg/ml) and Chloramphenicol (34 µg/ml) at 37°C, where it was left to incubate overnight.

The colonies that formed on the agar plate were then introduced into 250 ml cultures containing LB medium (20 mg/ml), Kanamycin (50 µg/ml), and Chloramphenicol (34 µg/ml). These cultures were maintained at 37°C with constant

agitation at 250 rpm for a period of 4 hours. After this incubation, the culture was evenly divided into four 1-liter flasks, each containing LB medium and the appropriate antibiotics. These cultures were then incubated until the optical density (OD) reached a value of 0.6. At an OD of 0.6, 1 ml of 1 M IPTG (Isopropyl β-D-1-thiogalactopyranoside) was added, and the 1-liter cultures were allowed to incubate overnight at 18°C with constant agitation at 250 rpm. On the following day, the cultures were subjected to centrifugation at 5,000 rpm, maintaining a temperature of 4°C, for a duration of 50 minutes using an SLC-4000 rotor. Following centrifugation, the supernatant was carefully decanted, and the cell pellets were collected in sterile 50 ml Falcon tubes, which were then stored in a -80°C freezer.

Two distinct buffers were prepared for subsequent steps: Buffer A (100 mM Tris, 300 mM NaCl, pH 8.0, 0.1% β-mercaptoethanol, and 5% glycerol) and Buffer B (100 mM Tris, 300 mM NaCl, pH 8.0, 0.1% β-mercaptoethanol, 1 M Imidazole, and 5% glycerol). The frozen protein pellets were thawed on ice and subsequently lysed for 50 minutes, employing constant agitation at 100 rpm on ice. Lysis was facilitated using a 50 ml lysis buffer containing 1 Pierce™ protease inhibitor pill (Thermo Scientific), 3 ml of 3X Bugbuster (EMD Millipore), 2 ml of DNase I (10 mg/ml), and 1 ml of RNase I (10 mg/ml), which was brought to a final volume of 50 ml using Buffer A. The lysate was subsequently subjected to centrifugation using an SS-34 rotor at 16,000 rpm for 50 minutes at 4°C, following which the supernatant was carefully transferred to 50 ml Falcon tubes, taking care not to discard the more viscous portion of the supernatant.

The supernatant was then loaded onto a pre-equilibrated 5 ml HisTrap column (GE Healthcare) at a loading rate of 2 ml/min. Protein elution was achieved through a gradient program, utilizing both Buffer A and Buffer B, with the final step involving 100% Buffer B. Throughout the elution process, the buffers were maintained at low temperatures. The fractions of interest were subjected to protein content and purity validation via 5%-10% SDS-PAGE. When required, protein fractions were combined and diluted 4-fold with Buffer A, followed by another round of purification utilizing a HisTrap column. Fractions containing the protein of interest were then dialyzed overnight in 3 liters of dialysis buffer (50 mM Tris, 150 mM NaCl, pH 8.0, 0.1% β-mercaptoethanol, and 5% glycerol), employing dialysis tubing with an appropriate molecular weight cut-off (MWCO) ranging from 12,000 to 14,000.

Size exclusion chromatography was used a third round of purification, if needed. The size exclusion buffer consisted of 50 mM Tris, 150 mM NaCl, 0.1% β-mercaptoethanol, and 5% glycerol. The injector and pump were thoroughly washed with 100 ml of size exclusion chromatography (SEC) buffer at a flow rate of 5 ml/min. A pre-equilibrated HiLoad 16/60 column packed with Superdex 75 prep-grade beads was loaded with 5 ml of concentrated sample. The elution was performed using 133 ml of SEC buffer, and 1 ml fractions were collected and subsequently assessed via SDS-PAGE for protein content. The fractions meeting the desired criteria were stored in 1 ml aliquots at -80°C for future use.

Chapter 3.3.b. Size Exclusion Chromatography

Superdex 200 10/300 GL (GE healthcare) column was used to perform analytical size exclusion chromatography in order to investigate the oligomeric state

of ctPRMT5. 250ul of protein standards (Bio-rad, 1511901) was injected and eluted with buffer (50mL Tris-HCl pH8.0, 150mM NaCl, 0.1% β-mercaptoethanol and 5% glycerol). Plot of elution volume and UV absorbance was used to generate a standard curve to determine molecular weight based on elution volume. 250ul ctPRMT5 protein sample at 1.6mg/mL concentration was injected and elution with buffer containing 50mL Tris-HCl pH8.0, 150mM NaCl, 0.1% β-mercaptoethanol and 5% glycerol.

Chapter 3.3.e. Crystallization

Crystallization screens were set up for the ctPRMT5 protein sample, at a concentration of 8 mg/mL and supplemented with 2 mM S-adenosylmethionine (SAM), at room temperature. ctPRMT5 samples were plated on an Art Robbins Intelliplate 3 well drop, which employs the sitting drop method. Crystals began to form around the end of one week, and crystals of diffraction quality were successfully obtained from condition No. 61 from the Index HT (Hampton Research, HR2-134) screen. This specific condition contains 0.2 M L-Proline, 0.1 M HEPES at pH 7.5, and 10% w/v Polyethylene glycol 3350. In preparation for data collection, the ctPRMT protein crystals were cryoprotected by direct transfer into the corresponding reservoir solution supplemented with 20% (v/v) glycerol and then flash frozen using liquid nitrogen and stored onto pucks.

Chapter 3.3.f. MALDI-MS Detection of ctPRMT5 Mono-/Di- Methylation

MALDI was used to determine the nature of the methylation activity exhibited by ctPRMT5. In this assay, 5 μM ctPRMT5, 25 μM H4 peptide, and 125 μM SAM were incubated in a Tris-buffered saline (TBS) solution (50 mM Tris, 150 mM NaCl,

and a pH of 8.0) for 3 hours. Following incubation, the samples underwent centrifugation using mini centrifuge tubes with a molecular weight cut-off of 10,000 (10k MWCO). This centrifugation step was carried out at 5000 rpm for 2 minutes. Prior to MALDI-MS, the sample flowthrough was prepared using Ziptip columns from Millipore, to get rid of salt. The Ziptip equilibration/elution buffer consisted of 50% acetonitrile (ACN) with 0.1% trifluoroacetic acid (TFA), while the wash solution used contained 0.1% TFA.

For the MALDI mass spectrometry analysis of the H4 peptide, a mixture of DHB (2,5-dihydroxybenzoic acid) and CHCA (α-cyano-4-hydroxycinnamic acid) was used as the MALDI matrix in a 1:1 ratio. The loading of the sample onto the MALDI plate was carried out as follows: 1 µl of DHB, 1 µl of the H4 peptide sample, and 1 µl of CHCA.

Chapter 3.3.g. SAM 510: SAM Methyltransferase Assay and SAMfluoro: SAM Methyltransferase Assay

Colorimetric and Fluorometric assay kits (G-Biosciences) were used in this study, and the reagents were prepped in accordance with the kit instructions before use. Before assay use, proteins underwent dialysis using Slide-A-Lyzer dialysis cassettes (Thermo Fisher) with a 10,000 MWCO. ctPRMT5 was dialyzed in 3 liters of dialysis buffer (50 mM Tris and 150 mM NaCl) for 4 hours at room temperature. ctRioK1 was dialyzed in the same manner as ctPRMT5, but at a constant temperature of 18°C. Subsequently, the proteins were concentrated to the desired concentration using mini concentrator tubes with a molecular weight cut-off (MWCO) of 10,000.

The concentration of proteins was determined via the nanodrop method using the Bradford technique.

The predetermined volume of the master mix was prepared based on numbers of samples. Stoichiometric amounts of Histone 4 (H4) peptide and ctPRMT5 were carefully pipetted into each designated well, followed by the addition of master mix (100 ul), initiating the reaction. Plate reader specifics for the colorimetric assay were as follows: absorbance reading at 510nm, wells read at every 20s for a duration of 70 minutes, plate read from the bottom. For the fluorescence assay plate reader specifics were as follows: Excitation 535nm, Emission 590nm, wells read every 30s for a duration of 70 minutes, plate read from the bottom, special fluorescence 96-well plates used.

Chapter 4. Determining the Structure Activity Relationship of RioK1 as a Kinase and Adaptor Protein

Understanding how RioK1 can function as both an ATPase and a kinase, while also serving as an adaptor protein, can be achieved by elucidating the structures of RioK1 complexes with small molecule inhibitors and biomolecules. This approach offers valuable insights into the multifaceted activities of RioK1 and potentially uncover novel regulatory mechanisms for RioK1. Chapter 2 introduced a novel inhibitor for RioK1 that utilizes a triazole ring to make an additional interaction in the active site, while chapter 3 characterized the relationship between PRMT5 and RioK1 acting as an adaptor protein. Building upon chapter 2 and 3, chapter 4 focuses on structural determination of RioK1 complexes to better understand its activity and presents future directions based on preliminary findings.

Chapter 4.1. Modification of the 1,2,4-triazole scaffold on KPSH02

The 1,2,4-triazole moiety at the end of KPSH02, boasts as a promising scaffold for inhibition for proteins that use metal ion-dependent nucleotide alignment. Every atom in the triazole ring is customizable allowing for further r-group additions to increase selectivity. In the case of RioK1 and KPSH02, despite the additional interaction KPSH02 creates, the thermal shift and preliminary kinetic data suggest that toyocamycin is a better inhibitor/interactor with Rio1 (Figures 7 & 8). Examination of the afRioK1 thermal curves reveals that toyocamycin exhibits a one-degree increment higher thermal stability than KPSH02. Our objective is to refine the triazole scaffold to preserve the interaction with D212, but also expand its spatial occupancy inside that pocket to enhance binding affinity and selectivity. To achieve

this, we propose to preserve the thiol group and replace the triazole with an adenosine-like moiety that will fit into the metal ion site and extend outward to potentially increase Rio1 specificity.

Conceptual inhibitor KPSH06 utilizes the adenosine backbone to conserve important interactions with afRioK1, but the triazole moiety resembles a modified purine ring (6-amino-1H-[1,2,4]triazolo[1,2-a]pyridazin-7(8H)-one) that can extend outward potentially making additional interactions with afRioK1 (Figure 19). When modelling the new compound, KPSH06, into the pocket of afRioK1, all interaction with the adenosine-backbone is conserved as well as the interaction with D212, however 2 new possible interactions are created with glutamate 60. One possible interaction with E60 is with the peptidyl amine and the side chain carbonyl group, these interactions are highlighted in red. Possible interaction with this residue is interesting as its non-conserved residue that is essential for ATP and phospho-aspartate positioning, which may enhance selectivity.

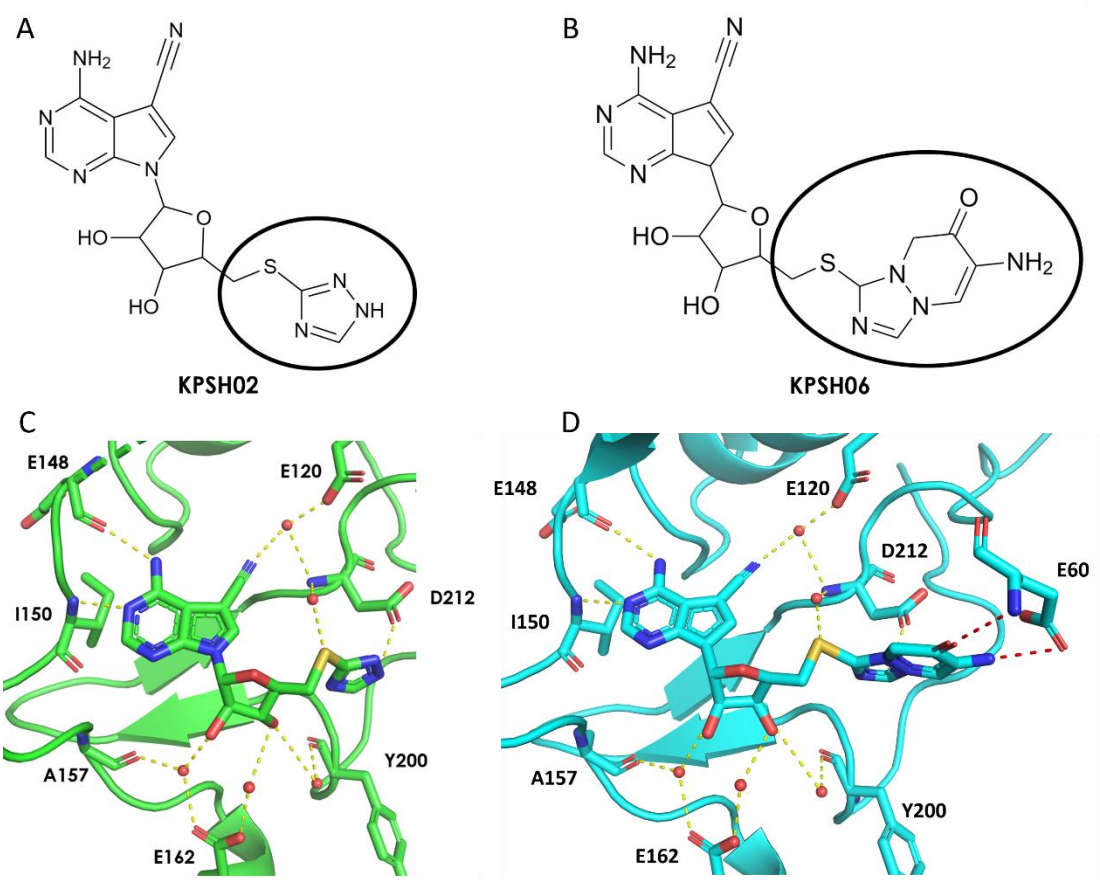

Figure 20. Differences between compound KPSH02 and theoretical compound KPSH06 and their interactions with afRioK1.

Note. Structure comparison between KPSH02 (A) and KPSH06 (B) with the triazole scaffold highlighted. Comparison of the interactions formed from KPSH02 (C) and KPSH06 (D) with afRioK1. Potential bidentate interaction formed by KPSH06 with residue E60 is shown in red.

This scaffold can be modified to select for other proteins as well not just those from the Rio family. For example, NAD kinase (NADK) converts nicotinamide adenine dinucleotide (NAD^+) into $NADP^+$ through phosphorylation of the NAD^+ coenzyme and has been shown to be very selective towards NAD and ATP.[104, 105] KPSH02 may have enough structural similarity to bind to NADK through nucleobase recognition allowing the 1,2,4-triazole ring to settle into the metal cation site, which

is observed in both the *a. Fulgidus* (PDB:1Z0S) and human NADK (PDB:7R4K) structures. When modelling KPSH02 into the active site of NADK the triazole ring appears to be able to displace the magnesium ion, while the adenosine base occupies and maintains the same interactions as ATP would (Figure 20). However, the nitrile group on C7 of KPSH02, makes an additional interaction with S161 through side chain hydrogen bonding. As with afRioK1, KPSH02 will have to be modified to increase selectivity and enhance binding.

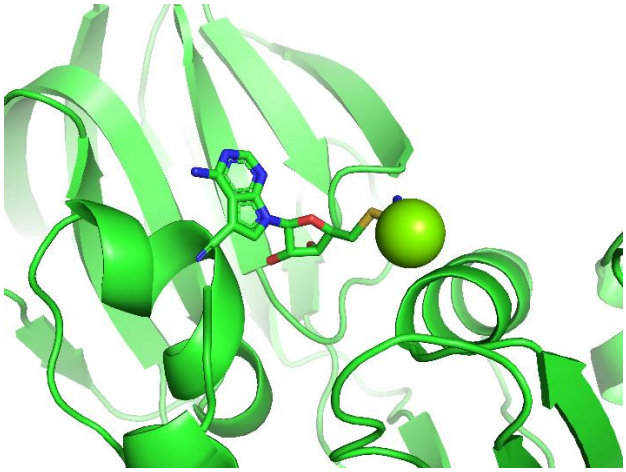

Figure 21. KPSH02 modelled into NADK (1Z0S) showing the triazole ring occupying the metal cation space.

As with conceptual inhibitor KPSH06, which was modified to target a less conserved residue in afRioK1, the 5'C R-group can be modified to target residues on NADK or any other enzyme that uses ATP-like substrates. What makes this scaffold highly customizable is the thiol moiety off the 5'C. The sulfur allows for easy substitution of r-groups via alkyl halide reactions if the synthon for the desired r-group is known. Alternatively, triazole derivatives can be synthesized using many different reaction mechanisms, albeit harder to make.

Chapter 4.2. Crystal Structures in Progress

Chapter 4.2.a. afRioK1 and SILCS Screen Compounds

Most of the compounds from the afRioK1 SILCS screening did not crystallize; surprisingly, compounds 5004, 46552, and 46336 were able to. According to the TSAs, compound 5004 had a slight destabilizing effect and compounds 46552 and 46336 had a destabilizing effect; however, these compounds exhibit r-group structures that greatly differ from KPSH02. Compound 5004 has its r-group addition off the 5'C on the adenosine sugar, while compounds 46552 and 46336 have their r-group addition off the N7 on the adenine. Deciphering the complex of these compounds bound to afRioK1 may provide insight on different drug scaffolds for afRioK1.

Data collection for compound 5004 was done at the Stanford Synchrotron Radiation light source (SSRL), while data was collected for compounds 46552 and 46336 from the National Synchrotron Light Source II at the Brookhaven National Laboratory. Table 7 outlines the lowest resolution each crystal diffracted at as well as the possible space group and unit cell parameters from integrating, scaling, and merging intensities. To solve the crystallography phase problem each of the three datasets used a "bare" coordinate file of afRioK1 (PDB:3RE4), that contained no waters, no ligands, no metal ions for molecular replacement using Phaser.

Compound	Resolution (Å)	Space Group	Unit Cell Parameters (a b c α β γ)
5004	3.31	P 1 2 1	53.0 73.4 61.4 90 89.9 90

Table 6. Data collection statistics for the three crystals structures in progress.

Note. Compounds 5004, 46336, and 46552 all have similar unit cell parameters. Interestingly, the 5004 complex falls within the monoclinic space group while the 46336 and 46552 complexes both fall within the orthrombic space groups considering both complexes are more likely to contain ATP in the active site.

46336	2.3	P 2_1 2 2_1	53.1 60.9 76.4 90 90 90
46552	2.5	P 2 2 2	53.4 79.2 121.2 90 90 90

Chapter 4.2.b. afRioK1 and Compound 5004

Compound 5004 is unique compared to synthesized molecule KPSH02 as both compound share the same adenosine moiety, but 5004 more resembles two adenosine monophosphates (AMP) joined together at the phosphate ends (Figure 6). The electron density acquired from molecular replacement highlighted an unmodeled "blob" in the active site of afRioK1. Initially, the unmodeled blob (>1.8 RMSD) looked promising as it had a relatively clear shape where you could see where the adenosine backbone would fit, as well as extra density for a potential R-group to extend from the 5'C. However, the extra density fits an ED "motif" commonly seen in enzymes that bind ATP. The electron density motif is 4 spherical blobs arranged in an upside down trigonal pyramidal geometry, where 3 of the spherical densities on the same plane are occupied by the alpha, beta, and gamma phosphates of ATP, while the 1 spherical density is out-of-plane with the others and is usually occupied by a metal ion to coordinate the position of the three phosphates (Figure 23A). A second round of refinement was done after ATP and Mg^{2+} were fitted into the unmodeled space and merged with the overall molecule. Including ATP into the active site lowered r-free from 0.3088 to 0.3003 and most of the positive density in the f_o-f_c (difference) map was accounted for.

Interestingly, there were two unmodeled densities found in both the initial refinement without ATP and with ATP. However, after the second refinement with ATP more density was found extending beneath the alpha phosphate position (Figure

23B). Additional density appearing after consecutive rounds of refinement is not uncommon, as refinement goes on the ED map quality improves allowing for more details to appear. Using the refinement model with ATP, ATP was edited out and compound 5004 was fit into the new density. Another round of refinement was performed using the same refinement methods as before.

The additional density highlighted in Figure 23B was sharpened when fitting compound 5004 into the density. As expected, the density where the gamma phosphate was in, when fitting in ATP, now appears a positive density in the difference map. This is usually an indication of a partial occupancy issue, as two ligands appear to compete for the active site and within the afRioK1 protein crystal some of the afRioK1 are bound to ATP and some are bound to compound 5004.

To better ascertain whether the additional density found in Figure 23B is indeed formed because of a partial occupancy of compound 5004, another round of refinement of done adjusting the occupancy of 5004 within the active site. Adjusting the occupancy of the active site showed that the density favored ATP instead of the r-group of compounds 5004. Positive density consistently showed up where the gamma phosphate of ATP would go, but not for the side chain of compound 5004. As the crystal diffracted at a low resolution of 3.4Å, it is hard to interpret the results accurately and co-crystallization with compound 5004 needs to be optimized (Figure 23C).

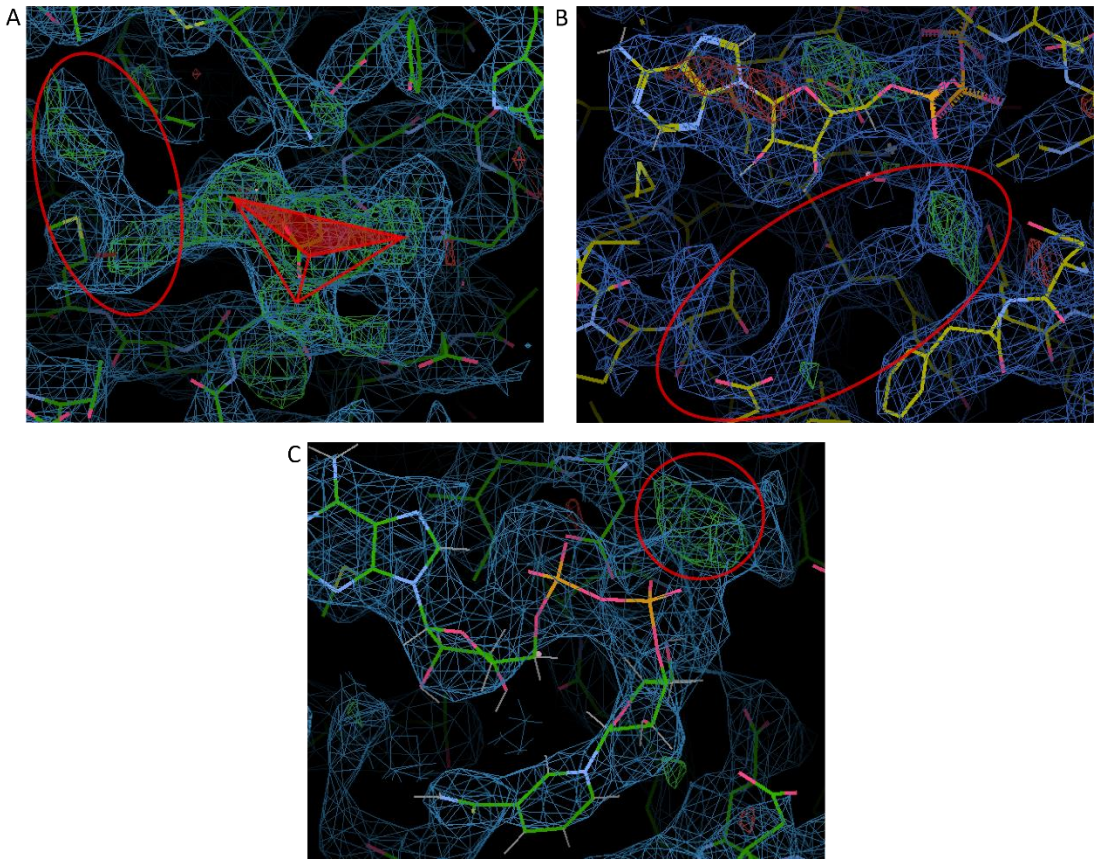

Figure 22. Electron density of afRioK1 + 5004 sample.

Note. (A) Unmodeled density within the active site of afRioK1. Highlighted in the red circle is density showing where the adenosine would fit. Highlighted by the red trigonal pyramidal shape is the r-group extending past the adenosine sugar. (B) ATP fitted into the unmodelled density, with new density highlighted by a red circle. (C) Compound 5004 fits into the additional density seen in the middle panel. Density where the gamma phosphate was, In ATP, shows up in the difference map.

Additional steps can be taken to increase the likelihood of afRioK1 binding to 5004 over ATP. During the initial phases of the purification process, apyrase can be added to the lysis buffer to break down any free ATP. Apyrase is an ATPase that breaks down nucleoside tri- and diphosphates. The afRioK1 construct has an intrinsic His-tag that can be used to separate afRioK1 in the purification steps. The addition of the apyrase enzyme should drastically reduce ATP and ADP binding.

Chapter 4.2.c. afRioK1 and Compound 46552

Despite the unfavorable position of the r-group in scaffolds-R1, compound 46552 managed to crystallize with afRioK1. Diffracting at 2.5Å, the electron density shows a relatively clear outline of the adenosine backbone (Figure 24A). Compound 46552 was fit into the observable density in the active site and much like compound 5004, the electron density sharpened around the compound. However, there is evidence of partial occupancy seen in figure 24B. Notably, the positive density near D212 and the negative density near the ether oxygen in the adenosine sugar moiety. The green density appears in the same location that a γ-phosphate would be if ATP was in the active site. The negative density could be contributed to a few factors namely poor positioning/orientation of the sugar moiety within the density. Multiple refinements were done with the sugar in different orientations; however, no configuration was found that would allow for full occupancy of the sugar without negative density in the omit map.

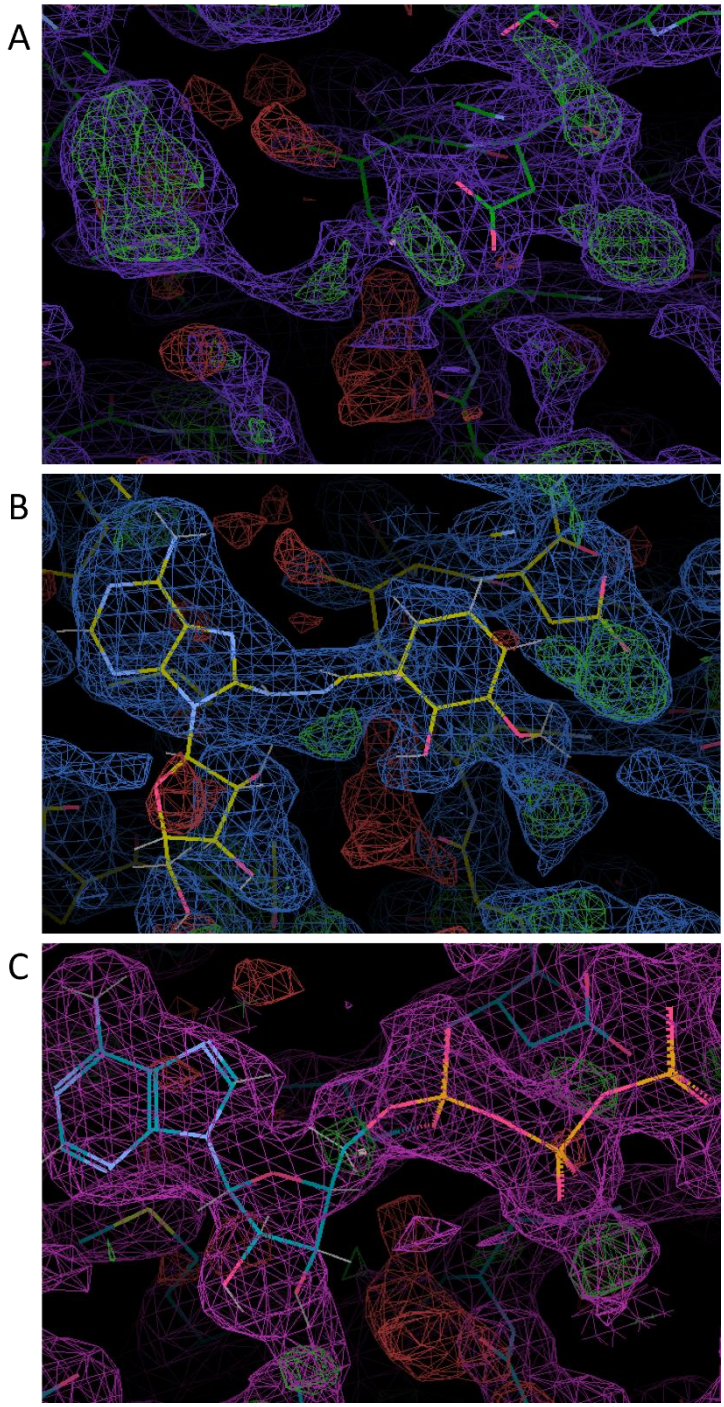

Figure 23. Examination of unmodelled electron density inside the active site of afRioK1-46552 complex.

Note. (A) Unmodelled density observed around catalytic residue D212. (B) Compound 46552 fitted into the density at the active site with some extra density still unmodelled near D212. (C) Compound 46552 was replaced with ATP. Unmodelled density prior to refinement is fully covered, albeit r-values spiked.

Positive density near residue D212 suggested that ATP could be in the active site in place of 46552. Refining ATP inside the ED showed that ATP fits well within the map and the omit map doesn't show any negative density. The refinement strategy used for 46552 was used for ATP with the only difference being the ligand bound at the active. Despite this, the R-values increased, and the local and environmental b-factors stayed nearly the same. The dataset for 46552 suffers the same affliction as the dataset for compound 5004, which is that the initial crystallization screens were contaminated with afRioK1 that was already bound to ATP. As discussed above, during the lysis step adding apyrase or any active ATPase should help reduce ATP binding to afRioK1.

Chapter 4.3. Elucidating the PRMT5-MEP50-RioK1 Protein Complex

At the time of the ctPRMT5 study was underway, other articles have discovered a secondary binding site on PRMT5 that can be occupied by adaptor proteins like RioK1, PICln, or COPR5 in a competitive manner. This led to the identification of conserved sequence that would allow binding to the secondary binding site on PRMT5, called the PRMT5 binding motif (PBM). Researchers were then able to synthesize small molecule inhibitors that mimic the PBM and were able to inhibit substrate adaptor proteins from binding to PRMT5. [65, 68, 77, 106, 107] Despite the amazing advancements towards controlling PRMT5s activity, it's still unclear how substrate arginine's are presented to the active site of PRMT5.

The focus of the future work is to engineer a recombinant PRMT5 where the PBM residues are optimized to enhance binding towards PRMT5. PRMT5's prolonged engagement with RioK1's PBM could allow for the structure to be

captured on Cryo-EM. The current PBM sequence that is shared among PRMT5 adapter proteins is GQF[D/E]DA[D/E] and is conserved among chordates (Figure 21).[66]

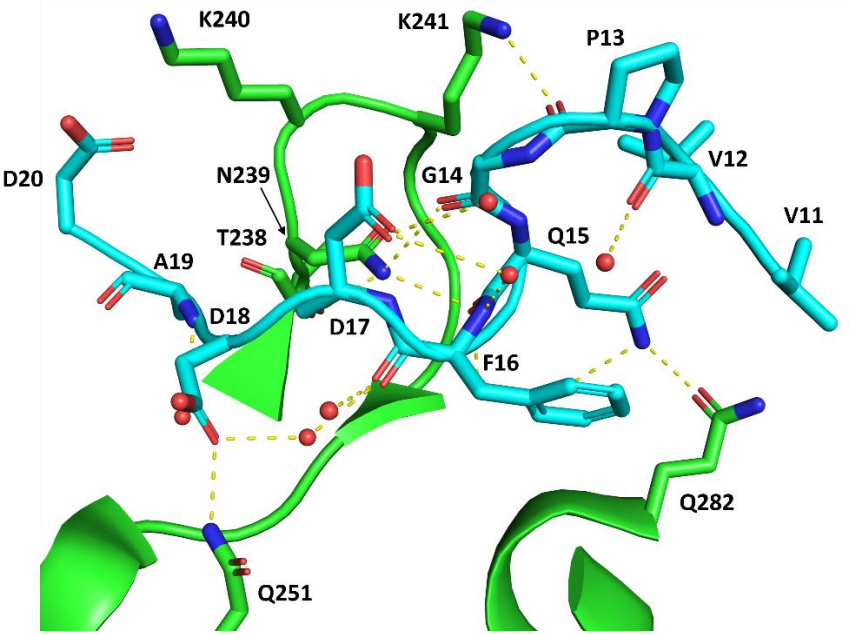

Figure 24. Interactions between RioK1 PBM sequence (Cyan) and PRMT5 (Green).

Typically, protein crystals only form when there is a single lowest stable energy point. Often two proteins in a complex don't meet at a singular lowest stable energy point, this can be from a wide range of factors like optimal buffer conditions and crystallization components all being unique to different proteins in a complex, which can make crystallizing protein complexes difficult and, in some cases, impossible. Alternatively, Cryo-EM can allow for a protein complex to be characterized in its native state forgoing a lot of the optimization process, although some optimization is always needed.

Using cryo-EM to visualize the PRMT5-RioK1 complex may be easier than trying to crystallize it. The discovery of the PRMT5 PBM yielded many

crystallography and cryo-EM structures of the PRMT5-PBM peptide complex, but none with full length RioK1 and PRMT5. One thing to consider is the promiscuous nature of PRMT5 binding to many different protein partners at the same site. Each adaptor protein was shown to bring a different substrate to PRMT5, meaning binding at PBM site can't be too tight otherwise PRMT5 would be limited to one adaptor protein and one substrate, contrary to what is in the literature. However, as mentioned above, by residue optimizing the RioK1-PBM and PBM binding site on PRMT5, the complex may be stable enough to be recorded with cryo-EM. The crystal structure of RioK1-PBM bound to the TIM barrel of PRMT5 (PDB:6V0N) shows that many of the residues participate in interactions with PRMT5 (Table 6). Upon closer inspection, there are 3 residues that don't interact with PRMT5 residue V11, A19, and D20. A V11D mutation on the PBM may allow it to interact with Q282 on PRMT5 because of the hydrogen bonding potential from the aspartate side chain. An A19S mutation might allow for hydrogen bonding to the peptidyl carbonyl from T238. Currently, D20 is 4.5Å away from K240 which may not allow for hydrogen bond formation, the extra carbon from a D20E mutation might bring the side chains closer together to enable stable hydrogen bonding.

Peptide Residue	PRMT5 Residue	Interaction Type	Distance (Å)
V11	N/A	N/A	N/A
V12	F243	Hydrophobic	N/A
P13	K241	H-bond	2.78
G14	N239	H-bond	3.41
Q15	N239	H-bond	2.99
Q15	Q282	H-bond	2.95
F16	Y286	Pi-stacking	N/A
D17	N239	H-bond	2.82
D18	Q251	H-bond	2.79
A19	N/A	N/A	N/A
D20	N/A	N/A	N/A

Table 7. Interactions between the RioK1-PBM peptide and PRMT5 TIM barrel.

Note. The category "interaction type" indicates how the residues interact with each other.

The mutant peptide sequence, DVPGQFDDSE, was created *in silico* using the peptide builder feature from Avogadro and was given chemical restraints using the Grade Web Server 2.0, which access the Cambridge structural database (CSD) of small molecules crystal structures to provide restraints and where the CSD fails to provide, it will generate restraints using the Universal Force Field (UFF).[108, 109] The mutant PBM was modeled into using the High Ambiguity Driven protein-protein DOCKing (HADDOCK) program where 11 clusters were used to generate the peptide-protein models.[110, 111] Multiple models were generated and the top models were able to accurately show the correct area of binding on PRMT5; however, the free base version of HADDOCK that was used did not account for the flexibility of the peptide and thus only fit the peptide as a rigid model (Figure 22).

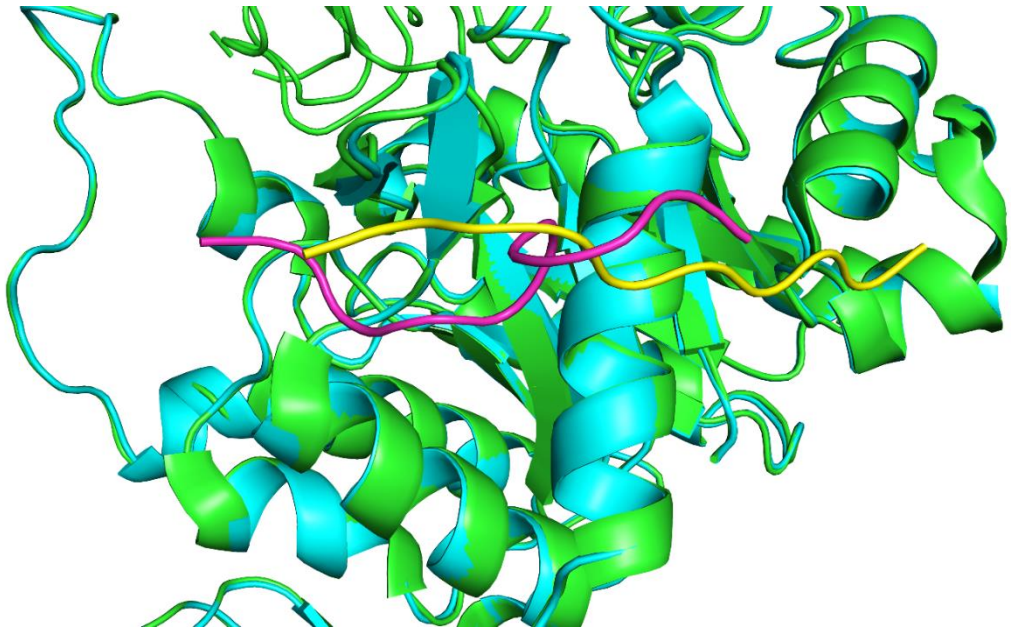

Figure 25. Docking simulation of wild type and mutant RioK1 PBM to PRMT5.

Note. Wild type RioK1 PBM (Magenta) bound to PRMT5 (Green) overlayed with the HADDOCK docking model of PRMT5 (Blue) complexed with mutant PBM (Yellow). The HADDOCK docking model was able to correctly identify the location on PRMT5 that would interact with the mutant PBM. However, the mutant PBM model appears to have been treated as a rigid model with minimal flexibility.

Chapter 5. Conclusion

Characterization of the structure and functional activity of afRioK1 and its interactions with PRMT5 were examined here. Previous work done by fellow colleague Dr. Minkyung Kim laid the foundation for the compound similarity search directed towards RioK1. Using the afRioK1-toyocamycin (PDB 3RE4) structure, Dr. Kim simulated toyocamycin inside the ADP-Mg^{2+}-RioK1 structure (PDB 4OTP) and observed an unutilized space around the 5'C on toyocamycin. This finding lead to our work on trying to exploit this free space to find small molecule inhibitors that were more selective towards RioK1 over other kinases, unlike toyocamycin.

A similarity search was done across the enamine and molport small molecule databases to identify compounds that contained an adenosine backbone, similar to

that of ATP and toyocamycin. Taking the ADP-Mg^{2+}-RioK1 structure, a FragMap was generated to identify any functional groups that could be targeted and simulations were run to predict the binding strengths of each compound to narrow down the list of compounds to test. The top 21 compounds were chosen to proceed with lead compound testing. Aside from the similarity search, a compound synthesized by fellow colleague Dr. Purushottamachar Puranik, KPSH02, was included in the study. KPSH02 closely mimics toyocamycin with two major differences at thiol group replaces the 5'C and a 1,2,4-triazole group is attached to the thiol group. A thermal shift assay was used on the compounds, and it was determined that KPSH02 had the highest stability shift on afRioK1. Furthermore, KPSH02 was found to inhibit afRioK1 enzymatic activity in a dose-dependent inhibition, despite the relatively low specific activity observed for afRioK1 identified in these enzyme preparations. X-ray crystallography was conducted on the top compounds from the thermal shift assays, and the structure of the afRioK1-KPSH02 complex is reported here.

Studies here were shown to define the role of afRioK1 as an adaptor protein that recruits Nucleolin as a substrate PRMT5 methylation. The discovery of the RioK1-PRMT5 interaction led to the discovery of several small molecule inhibitors targeting PRMT5's adaptor protein binding site. However, there remains a lack of information on exactly how RioK1-PRMT5 complex formation occurs. To explore this further, the activity of these proteins was tested to see if the activity changed in the presence of the other protein (i.e., co-activation). The goal was to determine whether RioK1 recruits other proteins to PRMT5, such as histone H4. As was expected, methyltransferase activity was found to be solely dependent on the

ctPRMT5 concentration. Additionally, the structure of ctPRMT5 tetramer is reported, which may provide insight into how arginine residues are presented to the active site of PRMT5.

There are numerous avenues to explore to further characterize RioK1 and its interaction with PRMT5. Despite the promising results from KPSH02 and the other top similarity search compounds, when compared to toyocamycin they underperformed in the TSA and kinetic assay. However, KPSH02 was designed with optimizations in mind. Every position on the 1,2,4-triazole ring is customizable that can have additional r-group added on, increasing selectivity towards not only RioK1, but many proteins that may use metal ions to coordinate ATP. The RioK1-PRMT5 complex remains to be solved. Elucidating the structure of this complex can shed new light on how target arginine's are presented to the active site of PRMT5. The sheer size of the full-length complex would require cryo-EM for structure determination.

Appendices

A. ^{13}H NMR of compound 41000

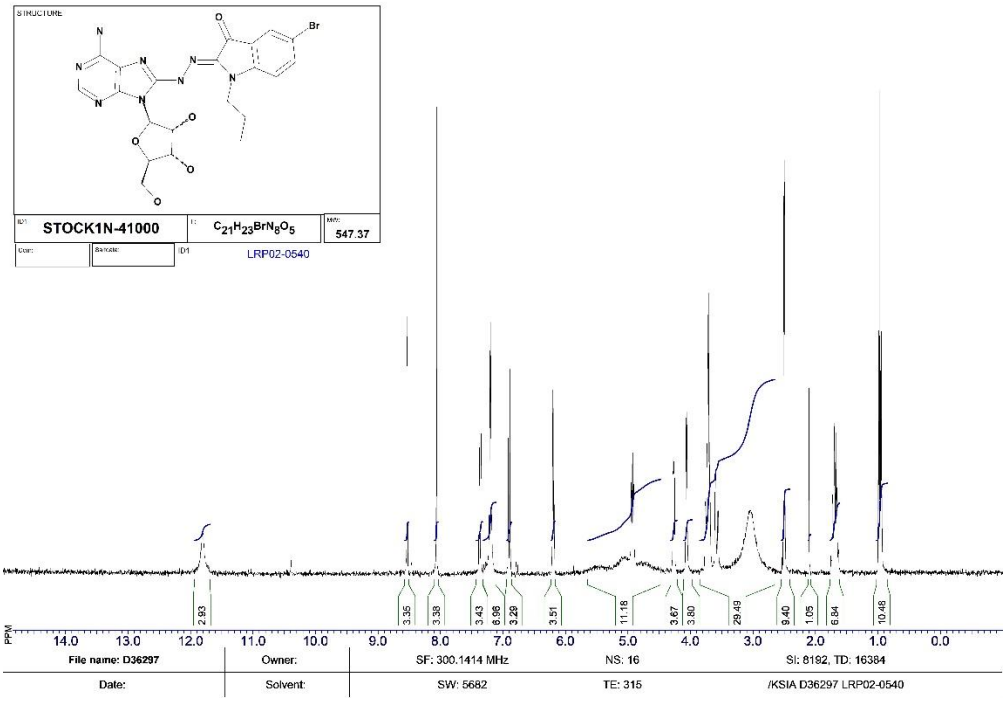

B. ^{13}H NMR of compound 42116

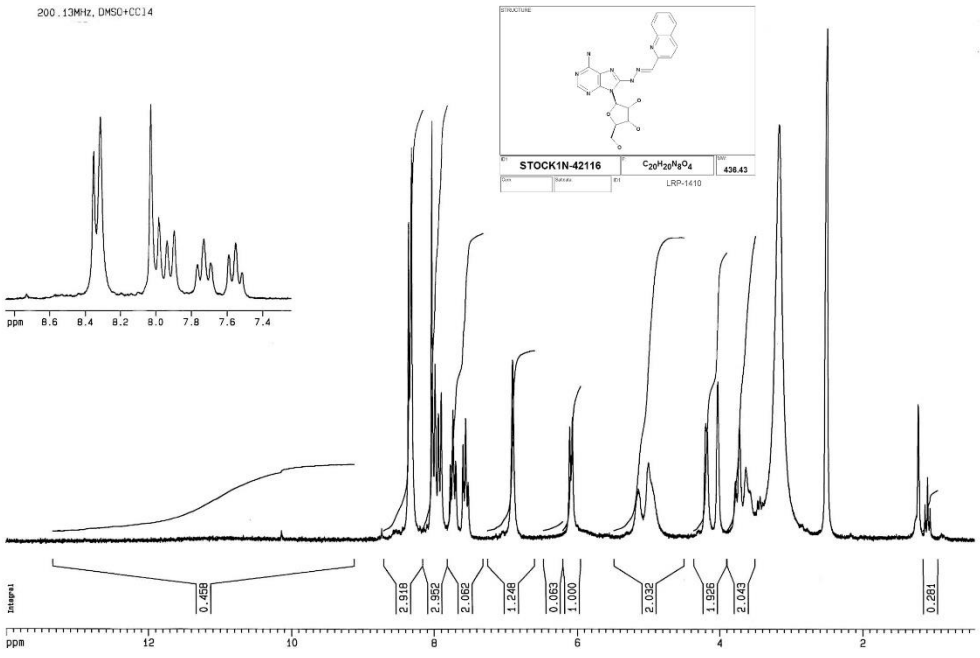

C. ^{13}H NMR of compound 42960

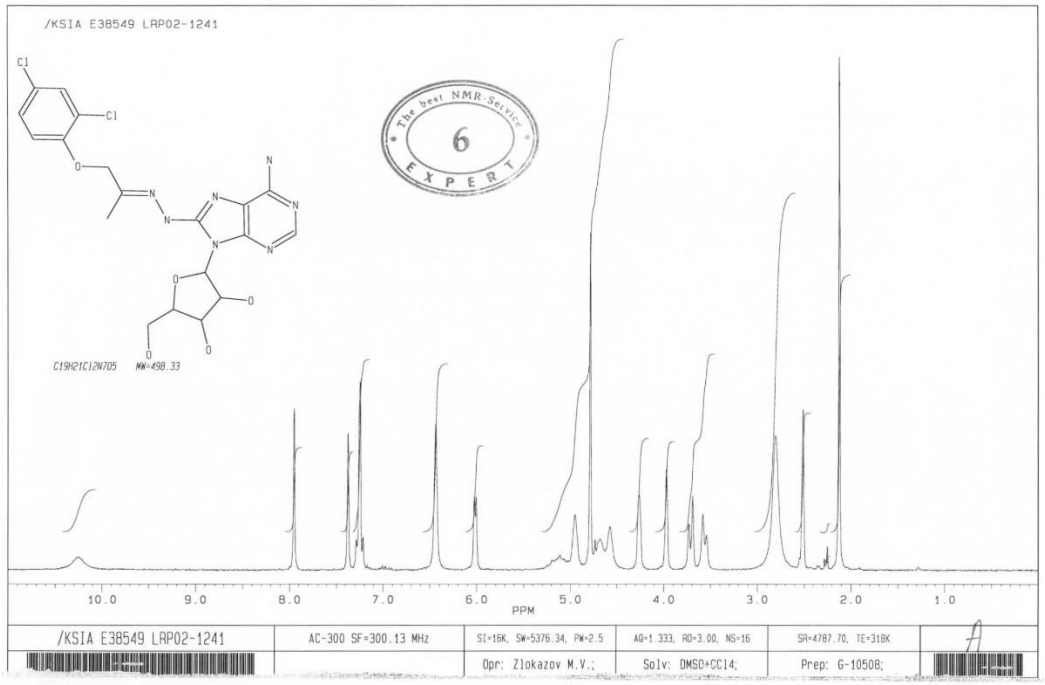

D. ^{13}H NMR of compound 46336

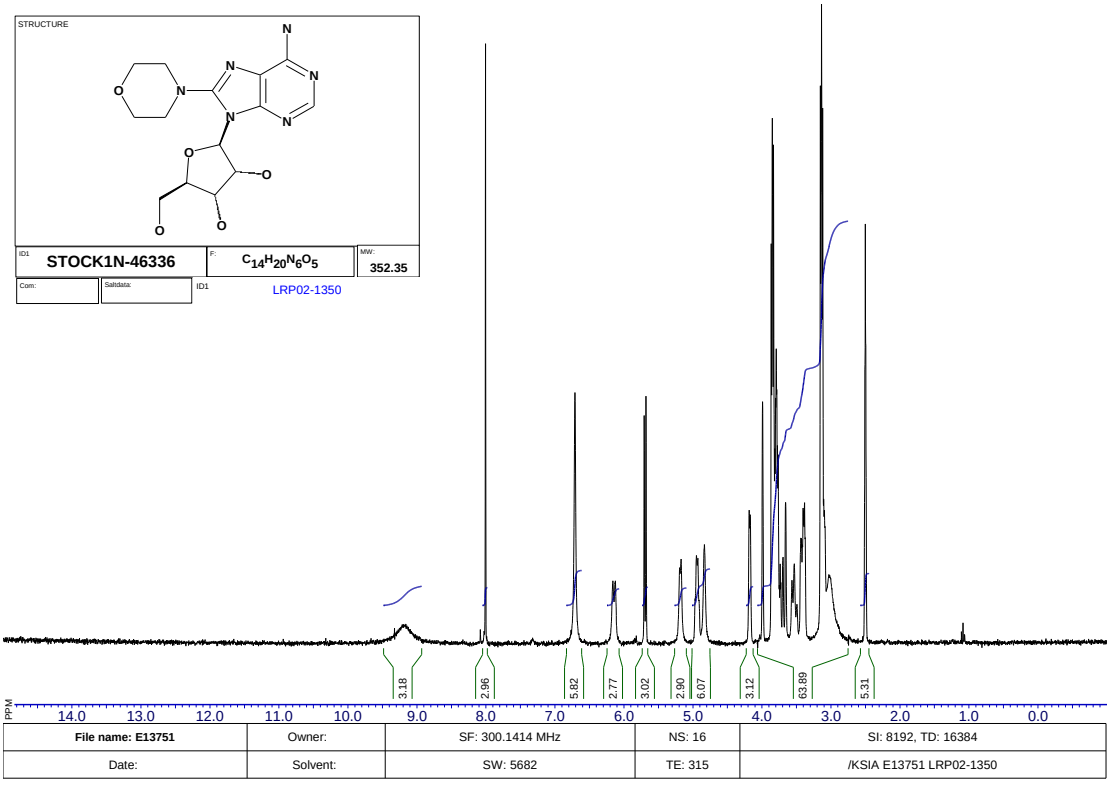

E. ^{13}H NMR of compound 46501

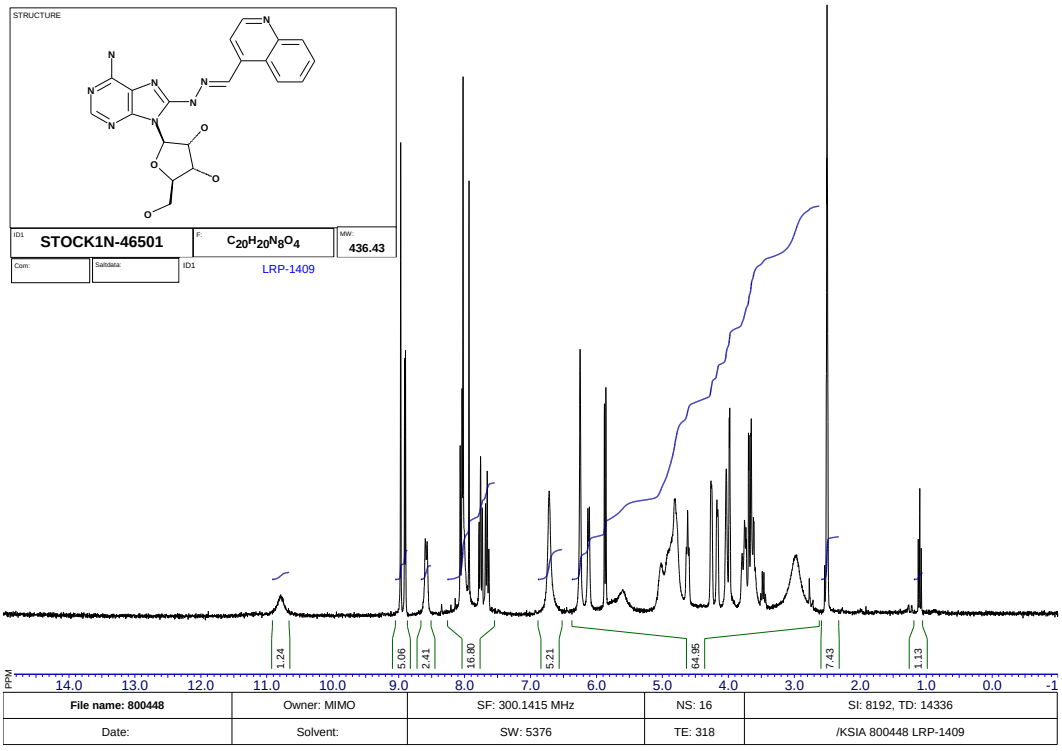

File name: 800448	Owner: MIMO	SF: 300.1415 MHz	NS: 16	SI: 8192, TD: 14336
Date:	Solvent:	SW: 5376	TE: 318	/KSIA 800448 LRP-1409

F. ^{13}H NMR of compound 46552

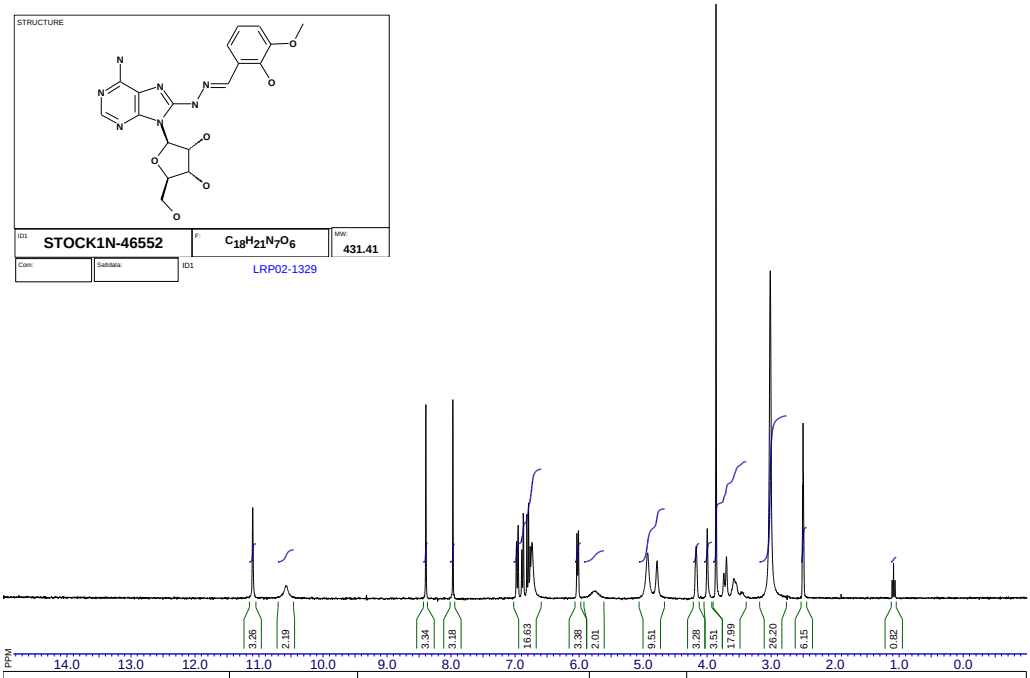

File name: E13749	Owner:	SF: 300.1414 MHz	NS: 16	SI: 8192, TD: 16384
Date:	Solvent:	SW: 5682	TE: 315	/KSIA E13749 LRP02-1329

G. ^{13}H NMR of compound 528300

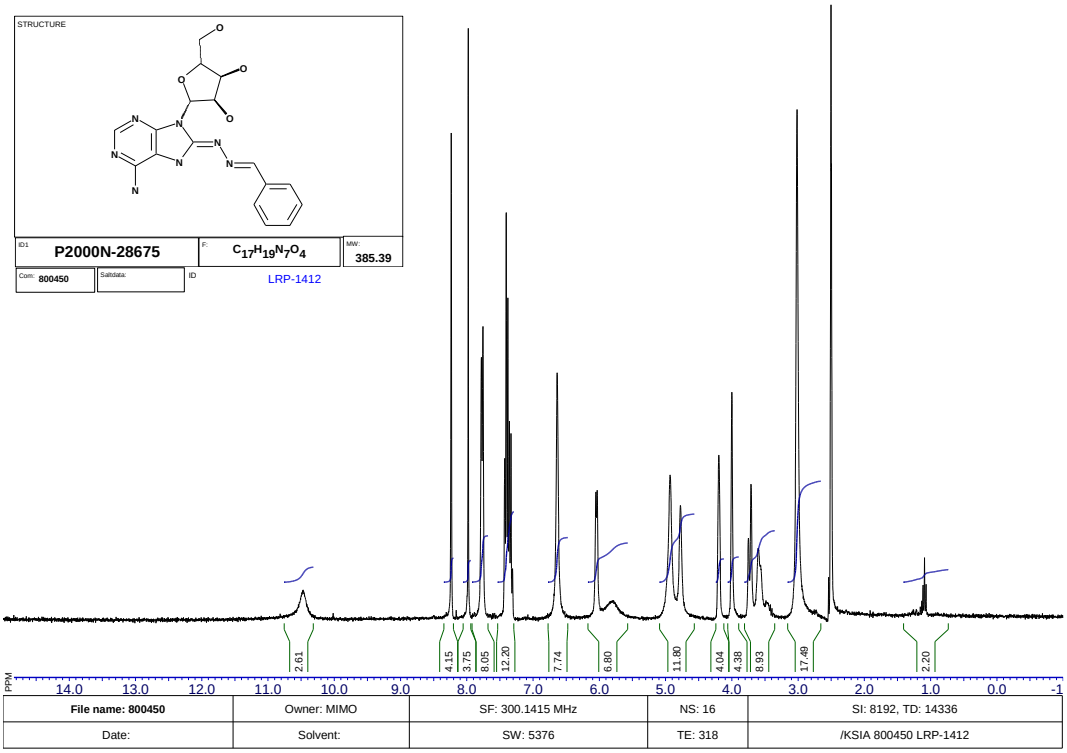

File name: 800450	Owner: MIMO	SF: 300.1415 MHz	NS: 16	SI: 8192, TD: 14336
Date:	Solvent:	SW: 5376	TE: 318	/KSIA 800450 LRP-1412

H. ^{13}H NMR of compound 528379

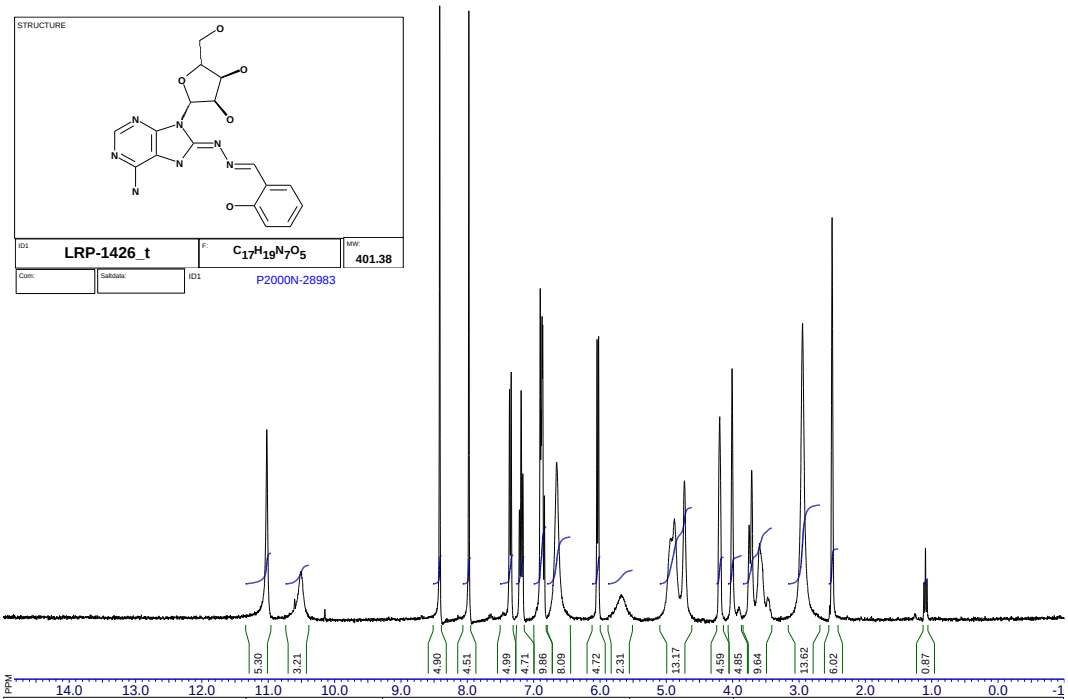

File name: C54328	Owner:	SF: 300.1415 MHz	NS: 16	SI: 8192, TD: 16384
Date:	Solvent:	SW: 5319	TE: 308	/KSIA C54328 LRP-1426

I. ^{13}H NMR of compound 528560

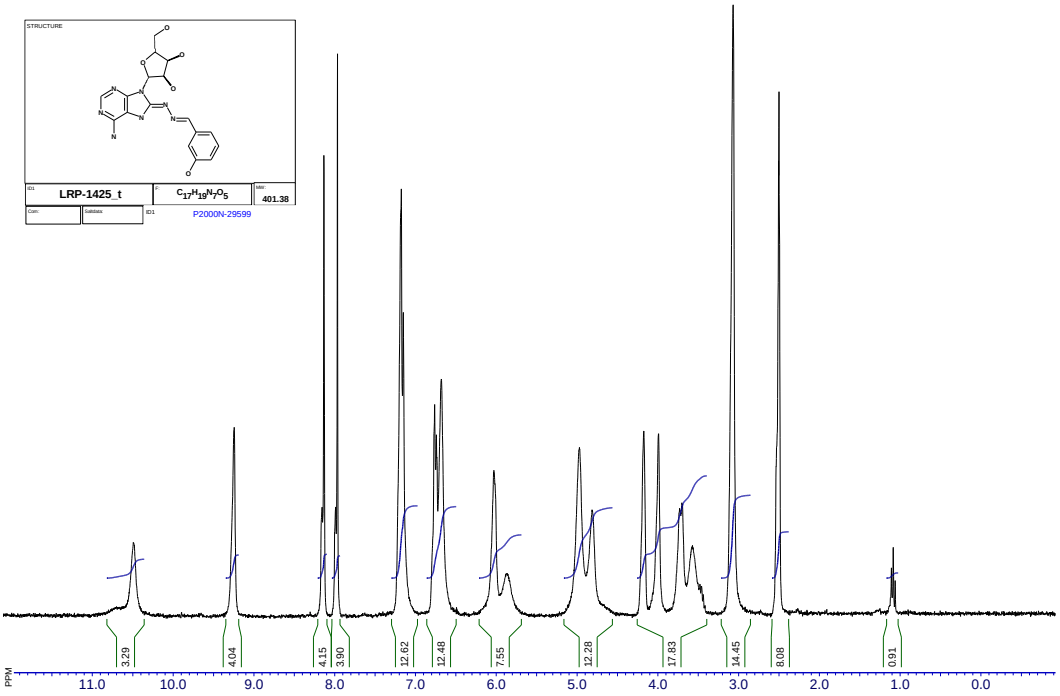

J. ^{13}H NMR of compound 528578

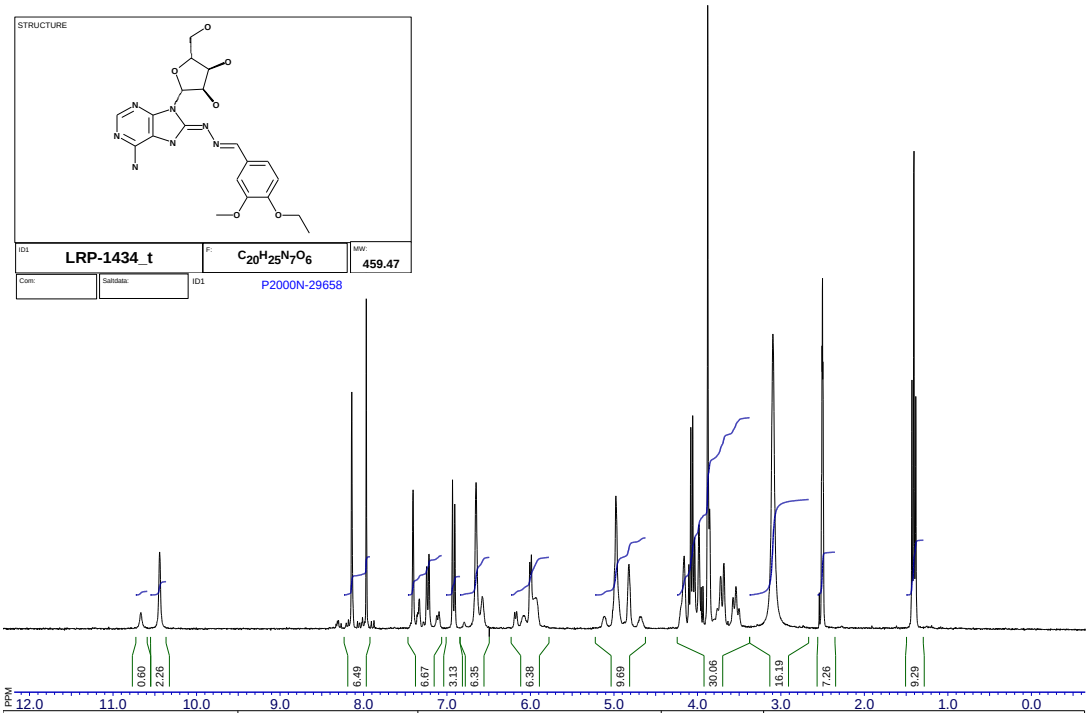

File name: 807379	Owner: MIMO	SF: 300.1415 MHz	NS: 16	SI: 8192, TD: 16384
Date:	Solvent:	SW: 5319	TE: 308	/KSIA 807379 LRP-1434

K. ^{13}H NMR of compound 540732

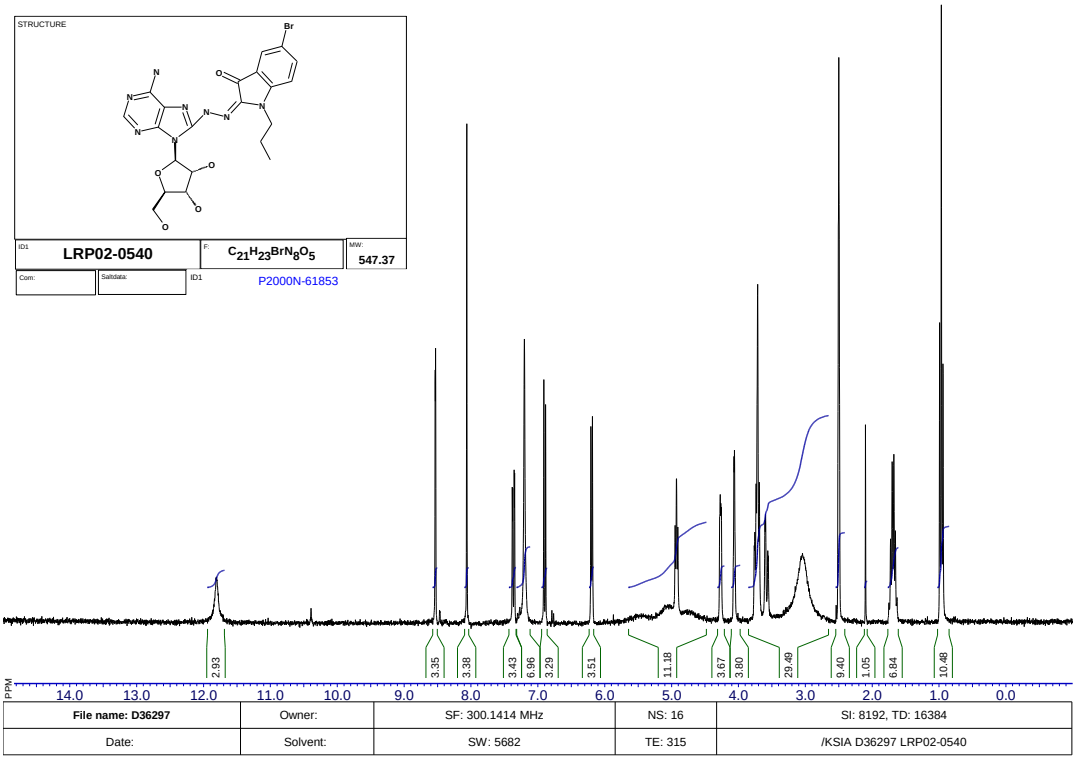

L. ^{13}H NMR of compound 541151

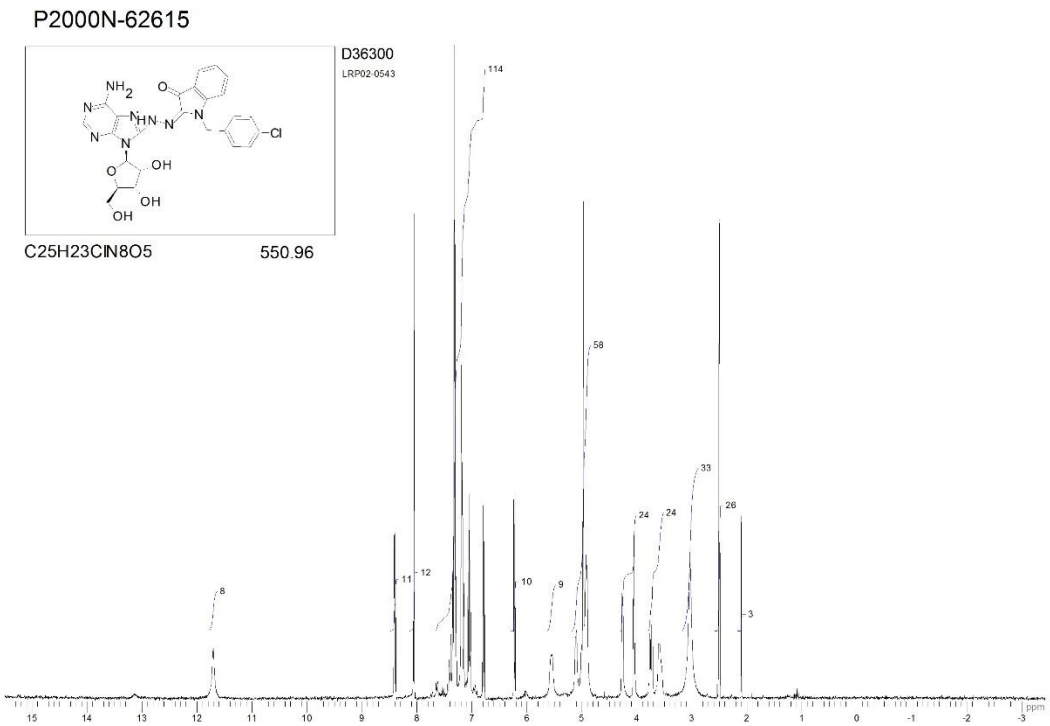

M. Certificate of Analysis of Compound 5004

Apollo Scientific Ltd

Whitefield Road, Bredbury,
Stockport, SK6 2QR, UK.
Tel:44(0)161 406 0505 Fax:44(0)161 406 0506
e-mail: sales@apolloscientific.co.uk

-CERTIFICATE OF ANALYSIS-

Product: beta-Thionicotinamide adenine dinucleotide, oxidised form

Code No: BIB5004

CAS No: 4090-29-3

Batch No: AS433469

	Specification	Result
Purity	≧92%	97.2 %
Thio-NAD^+ contents	—	93.1 %
Water contents	＜10%	4.2 %
Spectral analysis		
Ratio at pH 7.5		
A_{250} / A_{260}	0.89±0.03	0.87
A_{280} / A_{260}	0.36±0.02	0.35

N. Certificate of Analysis for Compound 18157

CERTIFICATE of ANALYSIS

5'-(N-Cyclopropyl)carboxamidoadenosine
1-(6-amino-9H-purin-9-yl)-N-cyclopropyl-1-deoxy-β-D-ribofuranuronamide
Item No. 18157 • Batch No. 0602924

Purity Specification: ≥95%
Molecular Formula : C13H16N6O4
CAS Number: 50908-62-8 **Formula Weight : 320.3** **Expiry date: 20NOV2022**

Overview

Tests	Results
HPLC	Purity: 98.0 %
IR	Conforms
Mass spec	M+Na: 343.4 MH+: 321.7
TLC	Purity: 100 %
UV	λ max: 259 nm
NMR	Conforms

Reviewed and approved by: Libby Perry

Libby Perry

CAYMAN CHEMICAL
1180 EAST ELLSWORTH RD
ANN ARBOR, MI 48108 · USA
PHONE: [800] 364-9897
[734] 971-3335
FAX: [734] 971-3640
CUSTSERV@CAYMANCHEM.COM
WWW.CAYMANCHEM.COM

O. Certificate of Analysis for Compound 21420

CERTIFICATE of ANALYSIS

5'-N-Ethylcarboxamidoadenosine (hydrate)
1-(6-amino-9H-purin-9-yl)-1-deoxy-N-ethyl-β-D-ribofuranuronamide, hydrate
Item No. 21420 • Batch No. 0608322

Purity Specification: ≥98%
Molecular Formula : C12H16N6O4 • XH2O
CAS Number: (unspecified) **Formula Weight: 308.29348** **Expiry date: 14OCT2023**

Overview

Tests	Results
HPLC	Purity: 99.6 %
IR	Conforms
Mass spec	MH+: 309.5
TLC	Purity: 100 %
UV	λ max: 260 nm
NMR	Conforms

Reviewed and approved by: Jennifer LaBrecque

WARNING
THIS PRODUCT IS FOR RESEARCH USE - NOT FOR HUMAN OR VETERINARY DIAGNOSTIC OR THERAPEUTIC USE. IT IS THE RESPONSIBILITY OF THE PURCHASER TO DETERMINE SUITABILITY FOR OTHER APPLICATIONS.

SAFETY DATA
This material should be considered hazardous until further information becomes available. Do not ingest, inhale, get in eyes, on skin, or on clothing. Wash thoroughly after handling. Before use, the user must review the complete Safety Data Sheet, which has been sent via email to your institution.

WARRANTY AND LIMITATION OF REMEDY
Buyer agrees to purchase the material subject to Cayman's Terms and Conditions. Complete Terms and Conditions including Warranty and Limitation of Liability information can be found on our website.

CAYMAN CHEMICAL
1180 EAST ELLSWORTH RD
ANN ARBOR, MI 48108 · USA
PHONE: [800] 364-9897
[734] 971-3335
FAX: [734] 971-3640
CUSTSERV@CAYMANCHEM.COM
WWW.CAYMANCHEM.COM

P. Certificate of Analysis for Compound 29476

CERTIFICATE of ANALYSIS

DS-437

5'-S-[2-[[(ethylamino)carbonyl]amino]ethyl]-5'-thio-adenosine

Item No. 29476 • Batch No. 0575635

Purity Specification: ≥98%
Molecular Formula : C15H23N7O4S
CAS Number: 1674364-87-4 Formula Weight : 397.4539 Expiry date: 24MAY2023

Overview

Tests	Results
HPLC	Purity: 98.9 %

Reviewed and approved by: Michelle Riley

CAYMAN CHEMICAL
1180 EAST ELLSWORTH RD
ANN ARBOR, MI 48108 · USA
PHONE: [800] 364-9897
[734] 971-3335
FAX: [734] 971-3640
CUSTSERV@CAYMANCHEM.COM
WWW.CAYMANCHEM.COM

Q. Certificate of Analysis for Compound 34684

CERTIFICATE of ANALYSIS

EB 47 (hydrochloride)

5′-deoxy-5′-[4-[2-[(2,3-dihydro-1-oxo-1H-isoindol-4-yl)amino]-2-oxoethyl]-1-piperazinyl]-5′-oxo-adenosine, dihydrochloride

Item No. 34684 • Batch No. 0621619

Purity Specification: ≥98%
Molecular Formula : C24H27N9O6 • 2HCl
CAS Number: 1190332-25-2 **Formula Weight:** 610.5 **Expiry date:** 14JAN2024

Overview

Tests	Results
Mass spec	M-2HCl: 538.2
HPLC	Purity: 99.7 %
NMR	Conforms

Reviewed and approved by: Michelle Riley

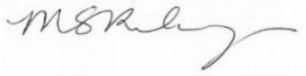

WARNING
THIS PRODUCT IS FOR RESEARCH USE - NOT FOR HUMAN OR VETERINARY DIAGNOSTIC OR THERAPEUTIC USE. IT IS THE RESPONSIBILITY OF THE PURCHASER TO DETERMINE SUITABILITY FOR OTHER APPLICATIONS.

SAFETY DATA
This material should be considered hazardous until further information becomes available. Do not ingest, inhale, get in eyes, on skin, or on clothing. Wash thoroughly after handling. Before use, the user must review the complete Safety Data Sheet, which has been sent via email to your institution.

WARRANTY AND LIMITATION OF REMEDY
Buyer agrees to purchase the material subject to Cayman's Terms and Conditions. Complete Terms and Conditions including Warranty and Limitation of Liability information can be found on our website.

CAYMAN CHEMICAL
1180 EAST ELLSWORTH RD
ANN ARBOR, MI 48108 · USA
PHONE: [800] 364-9897
[734] 971-3335
FAX: [734] 971-3640
CUSTSERV@CAYMANCHEM.COM
WWW.CAYMANCHEM.COM

R. Certificate of Analysis for Compound 5062

Building Blocks, Pharmaceutical Intermediates, Chemical Reagents, Catalysts & Ligands
www.ChemScene.com

Certificate of Analysis

Product Name:	SIBA
Cat. No.:	CS-5062
CAS No.:	35899-54-8
Batch No.:	17757
Chemical Name:	Adenosine, 5'-S-(2-methylpropyl)-5'-thio-

PHYSICAL AND CHEMICAL PROPERTIES

Molecular Formula:	$C_{14}H_{21}N_5O_3S$
Molecular Weight:	339.41
Storage:	Storage temp. 2-8°C
Chemical Structure:	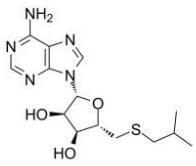

ANALYTICAL DATA

Appearance:	Off-white to gray (Solid)
LCMS:	Consistent with structure
Purity (LCMS):	99.66%
Conclusion:	The product has been tested and complies with the given specifications.

Caution: Product has not been fully validated for medical applications. For research use only.

Tel: 610-426-3128 Fax: 888-484-5008 E-mail: sales@ChemScene.com
Address: 1 Deer Park Dr, Suite Q, Monmouth Junction, NJ 08852, USA

S. Certificate of Analysis for Compound 020335

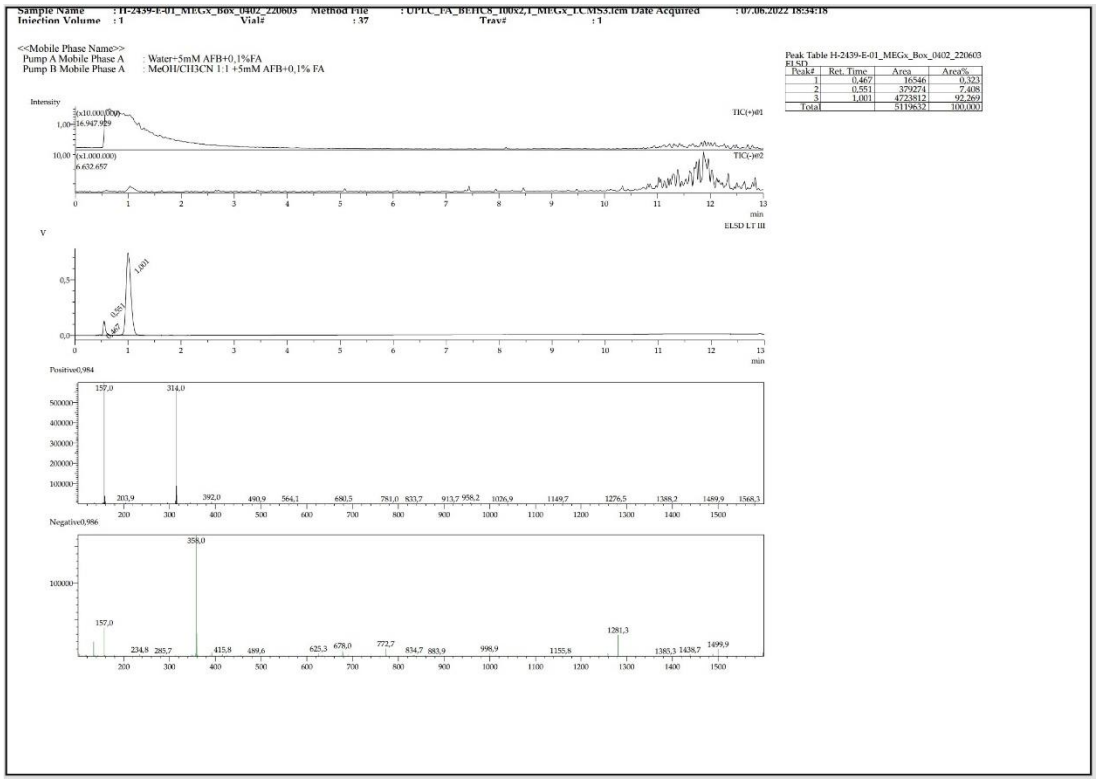

T. Certificate of Analysis for Compound 110862

TimTec, LLC
414 Churchmans Rd
New Castle, DE 19720

TimTec – Tampa
9720 Bay Plaza Blvd
Suite 606
Tampa, FL 33619
Phone: 1-302-292-8500 Fax: 1-302-292-8520
http://www.timtec.net e-mail timtec@timtec.net

Certificate of Analysis

Product Name:	8-(4-Chlorophenylthio)adenosine 3′,5′-cyclic monophosphate sodium salt

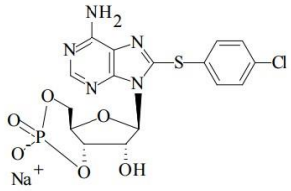

IDNUMBER(s)	ST110862
Molecular Formula	C16H14ClN5NaO6PS
Molecular Weight	493.8
Appearance:	Solid
Original Storage Container	Glass vial, crew top
Storage temperature	Minus 7 Celsius
Lot number	AL012
Purity by HPLC	97.1%

10/1/2020

U. ^{1}H NMR for compound KPSH02

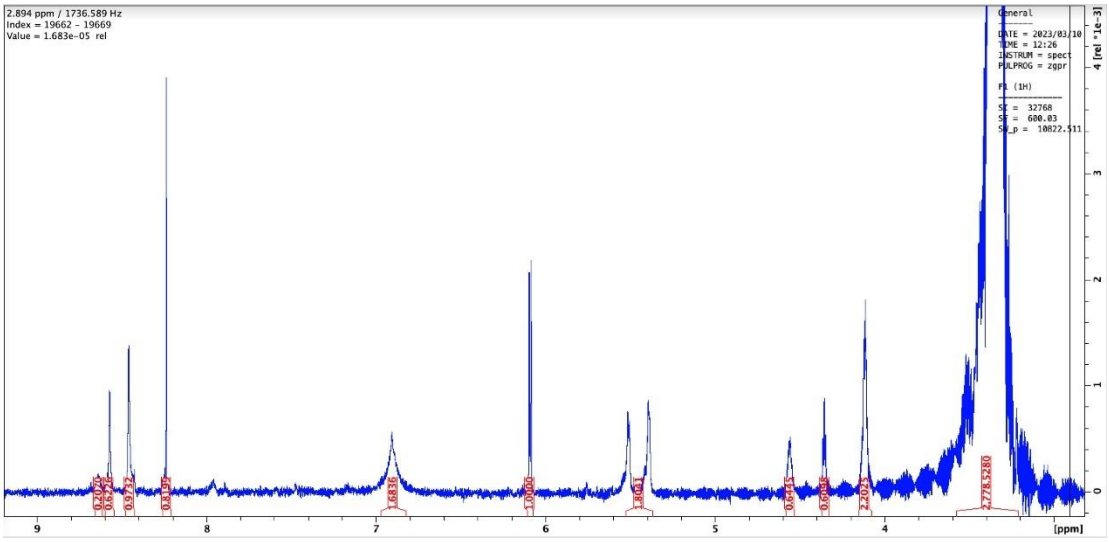

References

(1) Murphy, S. L. Mortality in the United States, 2020. Kochanek, K. D., Ed.; https://dx.doi.org/10.15620/cdc:112079: Hyattsville, MD, 2021.
(2) Collins, I.; Workman, P. New approaches to molecular cancer therapeutics. *Nature Chemical Biology* **2006**, *2* (12), 689-700. DOI: 10.1038/nchembio840.
(3) Fry, D. C.; Vassilev, L. T. Targeting protein–protein interactions for cancer therapy. *Journal of Molecular Medicine* **2005**, *83* (12), 955-963. DOI: 10.1007/s00109-005-0705-x.
(4) Liu, Y.; Gray, N. S. Rational design of inhibitors that bind to inactive kinase conformations. *Nature Chemical Biology* **2006**, *2* (7), 358-364. DOI: 10.1038/nchembio799.
(5) Noble, M. E. M.; Endicott, J. A.; Johnson, L. N. Protein Kinase Inhibitors: Insights into Drug Design from Structure. *Science* **2004**, *303* (5665), 1800-1805. DOI: 10.1126/science.1095920 (acccessed 2022/10/10).
(6) *An Update on Cancer Deaths in the United States.* Center for Disease Control and Prevention, 2020. https://www.cdc.gov/cancer/dcpc/research/update-on-cancer-deaths/index.htm (accessed 2022 10/4/2021).
(7) Kiburu, I. N.; Laronde-Leblanc, N. Interaction of Rio1 Kinase with Toyocamycin Reveals a Conformational Switch That Controls Oligomeric State and Catalytic Activity. *PLoS ONE* **2012**, *7* (5), e37371. DOI: 10.1371/journal.pone.0037371.
(8) Cohen, M. B.; Glazer, R. I. Comparison of the cellular and RNA-dependent effects of sangivamycin and toyocamycin in human colon carcinoma cells. *Molecular Pharmacology* **1985**, *27* (3), 349.
(9) Nishioka, H.; Sawa, T.; Hamada, M.; Shimura, N.; Imoto, M.; Umezawa, K. Inhibition of phosphatidylinositol kinase by toyocamycin. *The Journal of Antibiotics* **1990**, *43* (12), 1586-1589. DOI: 10.7164/antibiotics.43.1586.
(10) Park, S.-G.; Kim, S.-H.; Kim, K.-Y.; Yu, S.-N.; Choi, H.-D.; Kim, Y.-W.; Nam, H.-W.; Seo, Y.-K.; Ahn, S.-C. Toyocamycin induces apoptosis via the crosstalk between reactive oxygen species and p38/ERK MAPKs signaling pathway in human prostate cancer PC-3 cells. *Pharmacological Reports* **2017**, *69* (1), 90-96. DOI: 10.1016/j.pharep.2016.10.014.
(11) Ri, M.; Tashiro, E.; Oikawa, D.; Shinjo, S.; Tokuda, M.; Yokouchi, Y.; Narita, T.; Masaki, A.; Ito, A.; Ding, J.; et al. Identification of Toyocamycin, an agent cytotoxic for multiple myeloma cells, as a potent inhibitor of ER stress-induced XBP1 mRNA splicing. *Blood Cancer Journal* **2012**, *2* (7), e79-e79. DOI: 10.1038/bcj.2012.26.
(12) Fischer, P.; Lane, D. Inhibitors of Cyclin-Dependent Kinases as Anti-Cancer Therapeutics. *Current Medicinal Chemistry* **2000**, *7* (12), 1213-1245. DOI: 10.2174/0929867003374048.
(13) van Montfort, R. L. M.; Workman, P. Structure-based drug design: aiming for a perfect fit. (1744-1358 (Electronic)). From 2017 Nov 8.
(14) Berman, H. M.; Westbrook, J.; Feng, Z.; Gilliland, G.; Bhat, T. N.; Weissig, H.; Shindyalov, I. N.; Bourne, P. E. The Protein Data Bank. *Nucleic Acids Research* **2000**, *28* (1), 235-242. DOI: 10.1093/nar/28.1.235 (acccessed 9/20/2023).

(15) Sharma, V.; Wakode, S.; Kumar, H. Chapter 2 - Structure- and ligand-based drug design: concepts, approaches, and challenges. In *Chemoinformatics and Bioinformatics in the Pharmaceutical Sciences*, Sharma, N., Ojha, H., Raghav, P. K., Goyal, R. k. Eds.; Academic Press, 2021; pp 27-53.
(16) *Concepts and Applications of Molecular Similarity*; 1991.
(17) Akamatsu, M. Current state and perspectives of 3D-QSAR. (1568-0266 (Print)). From 2002 Dec.
(18) Yu, W.; Jo, S.; Lakkaraju, S. K.; Weber, D. J.; Mackerell, A. D. Exploring protein-protein interactions using the site-identification by ligand competitive saturation methodology. *Proteins: Structure, Function, and Bioinformatics* **2019**, *87* (4), 289-301. DOI: 10.1002/prot.25650.
(19) Guvench, O.; MacKerell, A. D., Jr. Computational Fragment-Based Binding Site Identification by Ligand Competitive Saturation. *PLOS Computational Biology* **2009**, *5* (7), e1000435. DOI: 10.1371/journal.pcbi.1000435.
(20) Best, R. B.; Zhu X Fau - Shim, J.; Shim J Fau - Lopes, P. E. M.; Lopes Pe Fau - Mittal, J.; Mittal J Fau - Feig, M.; Feig M Fau - Mackerell, A. D., Jr.; Mackerell, A. D., Jr. Optimization of the additive CHARMM all-atom protein force field targeting improved sampling of the backbone φ, ψ and side-chain χ(1) and χ(2) dihedral angles. (1549-9626 (Electronic)). From 2012 Sep 11.
(21) MacKerell, A. D.; Bashford D Fau - Bellott, M.; Bellott M Fau - Dunbrack, R. L.; Dunbrack Rl Fau - Evanseck, J. D.; Evanseck Jd Fau - Field, M. J.; Field Mj Fau - Fischer, S.; Fischer S Fau - Gao, J.; Gao J Fau - Guo, H.; Guo H Fau - Ha, S.; Ha S Fau - Joseph-McCarthy, D.; et al. All-atom empirical potential for molecular modeling and dynamics studies of proteins. (1520-6106 (Print)). From 1998 Apr 30.
(22) Ustach, V. D.; Lakkaraju, S. K.; Jo, S.; Yu, W.; Jiang, W.; MacKerell, A. D. Optimization and Evaluation of Site-Identification by Ligand Competitive Saturation (SILCS) as a Tool for Target-Based Ligand Optimization. *J Chem Inf Model* **2019**, *59* (6), 3018-3035. DOI: 10.1021/acs.jcim.9b00210 PubMed.
(23) LaRonde-LeBlanc, N.; Guszczynski, T.; Copeland, T.; Wlodawer, A. Structure and activity of the atypical serine kinase Rio1. *The FEBS Journal* **2005**, *272* (14), 3698-3713. DOI: 10.1111/j.1742-4658.2005.04796.x (acccessed 2019/04/20).
(24) LaRonde-LeBlanc, N.; Wlodawer, A. The RIO kinases: An atypical protein kinase family required for ribosome biogenesis and cell cycle progression. *Biochimica et Biophysica Acta (BBA) - Proteins and Proteomics* **2005**, *1754* (1), 14-24. DOI: https://doi.org/10.1016/j.bbapap.2005.07.037.
(25) Ferreira-Cerca, S.; Kiburu, I.; Thomson, E.; LaRonde, N.; Hurt, E. Dominant Rio1 kinase/ATPase catalytic mutant induces trapping of late pre-40S biogenesis factors in 80S-like ribosomes. *Nucleic Acids Research* **2014**, *42* (13), 8635-8647. DOI: 10.1093/nar/gku542 (acccessed 4/6/2019).
(26) Klinge, S.; Voigts-Hoffmann F Fau - Leibundgut, M.; Leibundgut M Fau - Arpagaus, S.; Arpagaus S Fau - Ban, N.; Ban, N. Crystal structure of the eukaryotic 60S ribosomal subunit in complex with initiation factor 6. (1095-9203 (Electronic)). From 2011 Nov 18.
(27) Klinge, S.; Woolford, J. L. Ribosome assembly coming into focus. *Nature Reviews Molecular Cell Biology* **2019**, *20* (2), 116-131. DOI: 10.1038/s41580-018-0078-y.

(28) Leary, D. J.; Huang, S. Regulation of ribosome biogenesis within the nucleolus. (0014-5793 (Print)). From 2001 Dec 7.
(29) Turowski, T. W.; Lebaron, S.; Zhang, E.; Peil, L.; Dudnakova, T.; Petfalski, E.; Granneman, S.; Rappsilber, J.; Tollervey, D. Rio1 mediates ATP-dependent final maturation of 40S ribosomal subunits. (1362-4962 (Electronic)). From 2014 Oct 29.
(30) Yusupova, G.; Yusupov, M. High-resolution structure of the eukaryotic 80S ribosome. (1545-4509 (Electronic)). From 2014.
(31) Berger, C. M.; Gaume, X.; Bouvet, P. The roles of nucleolin subcellular localization in cancer. *Biochimie* **2015**, *113*, 78-85. DOI: https://doi.org/10.1016/j.biochi.2015.03.023.
(32) Thomson, E.; Ferreira-Cerca, S.; Hurt, E. Eukaryotic ribosome biogenesis at a glance. *Journal of Cell Science* **2013**, *126* (21), 4815-4821. DOI: 10.1242/jcs.111948 (acccessed 12/31/2022).
(33) Fromont-Racine, M.; Senger B Fau - Saveanu, C.; Saveanu C Fau - Fasiolo, F.; Fasiolo, F. Ribosome assembly in eukaryotes. (0378-1119 (Print)). From 2003 Aug 14.
(34) Hector, R. D.; Burlacu, E.; Aitken, S.; Le Bihan, T.; Tuijtel, M.; Zaplatina, A.; Cook, A. G.; Granneman, S. Snapshots of pre-rRNA structural flexibility reveal eukaryotic 40S assembly dynamics at nucleotide resolution. (1362-4962 (Electronic)). From 2014 Oct 29.
(35) Rabl, J.; Leibundgut M Fau - Ataide, S. F.; Ataide Sf Fau - Haag, A.; Haag A Fau - Ban, N.; Ban, N. Crystal structure of the eukaryotic 40S ribosomal subunit in complex with initiation factor 1. (1095-9203 (Electronic)). From 2011 Feb 11.
(36) Parker, M. A.-O.; Collins, J. A.-O.; Korona, B.; Ghalei, H. A.-O.; Karbstein, K. A.-O. A kinase-dependent checkpoint prevents escape of immature ribosomes into the translating pool. (1545-7885 (Electronic)). From 2019 Dec.
(37) Orsolic, I.; Jurada, D.; Pullen, N.; Oren, M.; Eliopoulos, A. G.; Volarevic, S. The relationship between the nucleolus and cancer: Current evidence and emerging paradigms. (1096-3650 (Electronic)). From 2016 Jun.
(38) Truitt, M. L.; Ruggero, D. New frontiers in translational control of the cancer genome. (1474-1768 (Electronic)). From 2016 Apr 26.
(39) Bywater, M. J.; Poortinga G Fau - Sanij, E.; Sanij E Fau - Hein, N.; Hein N Fau - Peck, A.; Peck A Fau - Cullinane, C.; Cullinane C Fau - Wall, M.; Wall M Fau - Cluse, L.; Cluse L Fau - Drygin, D.; Drygin D Fau - Anderes, K.; Anderes K Fau - Huser, N.; et al. Inhibition of RNA polymerase I as a therapeutic strategy to promote cancer-specific activation of p53. (1878-3686 (Electronic)). From 2012 Jul 10.
(40) Drygin, D.; Rice Wg Fau - Grummt, I.; Grummt, I. The RNA polymerase I transcription machinery: an emerging target for the treatment of cancer. (1545-4304 (Electronic)). From 2010.
(41) Ferreira, R.; Schneekloth, J. S.; Panov, K. I.; Hannan, K. M.; Hannan, R. D. Targeting the RNA Polymerase I Transcription for Cancer Therapy Comes of Age. In *Cells*, 2020; Vol. 9.
(42) Schneider, D. A. RNA polymerase I activity is regulated at multiple steps in the transcription cycle: recent insights into factors that influence transcription elongation. (1879-0038 (Electronic)). From 2012 Feb 10.

(43) Sulima, S. O.; Hofman, I. J. F.; De Keersmaecker, K.; Dinman, J. D. How Ribosomes Translate Cancer. (2159-8290 (Electronic)). From 2017 Oct.
(44) Bastide, A.; David, A. The ribosome, (slow) beating heart of cancer (stem) cell. (2157-9024 (Print)). From 2018 Apr 20.
(45) Donati, G.; Montanaro L Fau - Derenzini, M.; Derenzini, M. Ribosome biogenesis and control of cell proliferation: p53 is not alone. (1538-7445 (Electronic)). From 2012 Apr 1.
(46) Li, D.; Wang, J. Ribosome heterogeneity in stem cells and development. LID - 10.1083/jcb.202001108 [doi] LID - e202001108. (1540-8140 (Electronic)). From 2020 Jun 1.
(47) McCool, M. A.; Bryant, C. J.; Baserga, S. J. MicroRNAs and long non-coding RNAs as novel regulators of ribosome biogenesis. *Biochemical Society Transactions* **2020**, *48* (2), 595-612. DOI: 10.1042/BST20190854 (acccessed 10/4/2023).
(48) Parks, M. A.-O.; Kurylo, C. M.; Dass, R. A.-O.; Bojmar, L.; Lyden, D. A.-O.; Vincent, C. T.; Blanchard, S. A.-O. Variant ribosomal RNA alleles are conserved and exhibit tissue-specific expression. (2375-2548 (Electronic)). From 2018 Feb.
(49) Elhamamsy, A. R.; Metge, B. J.; Alsheikh, H. A.; Shevde, L. A.; Samant, R. S. Ribosome Biogenesis: A Central Player in Cancer Metastasis and Therapeutic Resistance. *Cancer Research* **2022**, *82* (13), 2344-2353. DOI: 10.1158/0008-5472.CAN-21-4087 (acccessed 10/4/2023).
(50) Mauro, V. P.; Edelman, G. M. The ribosome filter hypothesis. (0027-8424 (Print)). From 2002 Sep 17.
(51) Drygin, D.; Lin A Fau - Bliesath, J.; Bliesath J Fau - Ho, C. B.; Ho Cb Fau - O'Brien, S. E.; O'Brien Se Fau - Proffitt, C.; Proffitt C Fau - Omori, M.; Omori M Fau - Haddach, M.; Haddach M Fau - Schwaebe, M. K.; Schwaebe Mk Fau - Siddiqui-Jain, A.; Siddiqui-Jain A Fau - Streiner, N.; et al. Targeting RNA polymerase I with an oral small molecule CX-5461 inhibits ribosomal RNA synthesis and solid tumor growth. (1538-7445 (Electronic)). From 2011 Feb 15.
(52) Haddach, M.; Schwaebe, M. K.; Michaux, J.; Nagasawa, J.; O'Brien, S. E.; Whitten, J. P.; Pierre, F.; Kerdoncuff, P.; Darjania, L.; Stansfield, R.; et al. Discovery of CX-5461, the First Direct and Selective Inhibitor of RNA Polymerase I, for Cancer Therapeutics. *ACS Medicinal Chemistry Letters* **2012**, *3* (7), 602-606. DOI: 10.1021/ml300110s.
(53) Peltonen, K.; Colis, L.; Liu, H.; Trivedi, R.; Moubarek, M. S.; Moore, H. M.; Bai, B.; Rudek, M. A.; Bieberich, C. J.; Laiho, M. A targeting modality for destruction of RNA polymerase I that possesses anticancer activity. *Cancer Cell* **2014**, *25* (1), 77-90. DOI: 10.1016/j.ccr.2013.12.009 PubMed.
(54) Peltonen, K.; Colis L Fau - Liu, H.; Liu H Fau - Jäämaa, S.; Jäämaa S Fau - Moore, H. M.; Moore Hm Fau - Enbäck, J.; Enbäck J Fau - Laakkonen, P.; Laakkonen P Fau - Vaahtokari, A.; Vaahtokari A Fau - Jones, R. J.; Jones Rj Fau - af Hällström, T. M.; af Hällström Tm Fau - Laiho, M.; et al. Identification of novel p53 pathway activating small-molecule compounds reveals unexpected similarities with known therapeutic agents. (1932-6203 (Electronic)). From 2010 Sep 27.
(55) Dauban, L.; Cerezo, E.; Henras, A.; Gadal, O. Meeting report from the first European OddPols meeting: Toulouse 2018. (1879-0038 (Electronic)). From 2019 Jun 20.

(56) Siegel, R. A.-O.; Miller, K. A.-O.; Goding Sauer, A.; Fedewa, S. A.; Butterly, L. F.; Anderson, J. C.; Cercek, A.; Smith, R. A.; Jemal, A. Colorectal cancer statistics, 2020. (1542-4863 (Electronic)). From 2020 May.
(57) Chen, Y.; Zhou, S.; Wan, K.; Yu, L.; Chongchong, Z.; Deng, H.; Ou, Q.; Qin, J.; Hu, J.; Hou, Z. RIOK1 mediates p53 degradation and radioresistance in colorectal cancer through phosphorylation of G3BP2. *Oncogene* **2022**, *41*, 1-12. DOI: 10.1038/s41388-022-02352-4.
(58) Hong, X.; Huang, H.; Qiu, X.; Ding, Z.; Feng, X.; Zhu, Y.; Zhuo, H.; Hou, J.; Zhao, J.; Cai, W.; et al. Targeting posttranslational modifications of RIOK1 inhibits the progression of colorectal and gastric cancers. *eLife* **2018**, *7*, e29511. DOI: 10.7554/eLife.29511.
(59) Gunic, E.; Girardet, J.-L.; Pietrzkowski, Z.; Esler, C.; Wang, G. Synthesis and cytotoxicity of 4′-C- and 5′-C-substituted toyocamycins. *Bioorganic & Medicinal Chemistry* **2001**, *9* (1), 163-170. DOI: https://doi.org/10.1016/S0968-0896(00)00221-2.
(60) Wang, G.; Tam, R. C.; Gunic, E.; Du, J.; Bard, J.; Pai, B. Synthesis and Cytokine Modulation Properties of Pyrrolo[2,3-d]-4-pyrimidone Nucleosides. *Journal of Medicinal Chemistry* **2000**, *43* (13), 2566-2574. DOI: 10.1021/jm000035+.
(61) Hinshaw, B. C.; Gerster, J. F.; Robins, R. K.; Townsend, L. B. Pyrrolopyrimidine nucleosides. V. Relative chemical reactivity of the 5-cyano group of the nucleoside antibiotic toyocamycin and desaminotoyocamycin. Synthesis of analogs of sangivamycin. *The Journal of Organic Chemistry* **1970**, *35* (1), 236-241. DOI: 10.1021/jo00826a049.
(62) Berto, G.; Ferreira-Cerca, S.; De Wulf, P. The Rio1 protein kinases/ATPases: conserved regulators of growth, division, and genomic stability. *Current Genetics* **2019**, *65* (2), 457-466. DOI: 10.1007/s00294-018-0912-y.
(63) Blanc, R. S.; Richard, S. Arginine Methylation: The Coming of Age. *Molecular Cell* **2017**, *65* (1), 8-24. DOI: https://doi.org/10.1016/j.molcel.2016.11.003.
(64) Burgos, E. S.; Wilczek, C.; Onikubo, T.; Bonanno, J. B.; Jansong, J.; Reimer, U.; Shechter, D. Histone H2A and H4 N-terminal Tails Are Positioned by the MEP50 WD Repeat Protein for Efficient Methylation by the PRMT5 Arginine Methyltransferase. *Journal of Biological Chemistry* **2015**, *290* (15), 9674-9689. DOI: 10.1074/jbc.m115.636894.
(65) Lacroix, M.; Messaoudi, S. E.; Rodier, G.; Le Cam, A.; Sardet, C.; Fabbrizio, E. The histone-binding protein COPR5 is required for nuclear functions of the protein arginine methyltransferase PRMT5. *EMBO reports* **2008**, *9* (5), 452-458. DOI: 10.1038/embor.2008.45.
(66) Mulvaney, K. M.; Blomquist, C.; Acharya, N.; Li, R.; Ranaghan, M. J.; O'Keefe, M.; Rodriguez, D. J.; Young, M. J.; Kesar, D.; Pal, D.; et al. Molecular basis for substrate recruitment to the PRMT5 methylosome. *Molecular Cell* **2021**. DOI: https://doi.org/10.1016/j.molcel.2021.07.019.
(67) Ho, M.-C.; Wilczek, C.; Bonanno, J. B.; Xing, L.; Seznec, J.; Matsui, T.; Carter, L. G.; Onikubo, T.; Kumar, P. R.; Chan, M. K.; et al. Structure of the Arginine Methyltransferase PRMT5-MEP50 Reveals a Mechanism for Substrate Specificity. *PLOS ONE* **2013**, *8* (2), e57008. DOI: 10.1371/journal.pone.0057008.

(68) Guderian, G.; Peter, C.; Wiesner, J.; Sickmann, A.; Schulze-Osthoff, K.; Fischer, U.; Grimmler, M. RioK1, a new interactor of protein arginine methyltransferase 5 (PRMT5), competes with pICln for binding and modulates PRMT5 complex composition and substrate specificity. *The Journal of biological chemistry* **2011**, *286* (3), 1976-1986. DOI: 10.1074/jbc.M110.148486 PubMed.
(69) Chan-Penebre, E.; Kuplast, K. G.; Majer, C. R.; Boriack-Sjodin, P. A.; Wigle, T. J.; Johnston, L. D.; Rioux, N.; Munchhof, M. J.; Jin, L.; Jacques, S. L.; et al. A selective inhibitor of PRMT5 with in vivo and in vitro potency in MCL models. *Nature Chemical Biology* **2015**, *11* (6), 432-437. DOI: 10.1038/nchembio.1810.
(70) Kim, H.; Ronai, Z. E. A. PRMT5 function and targeting in cancer. *Cell Stress* **2020**, *4* (8), 199-215. DOI: 10.15698/cst2020.08.228.
(71) Liu, X.; He, J.; Mao, L.; Zhang, Y.; Cui, W.; Duan, S.; Jiang, A.; Gao, Y.; Sang, Y.; Huang, G. EPZ015666, a selective protein arginine methyltransferase 5 (PRMT5) inhibitor with an antitumour effect in retinoblastoma. *Experimental Eye Research* **2021**, *202*, 108286. DOI: https://doi.org/10.1016/j.exer.2020.108286.
(72) Marjon, K.; Cameron, Michael J.; Quang, P.; Clasquin, Michelle F.; Mandley, E.; Kunii, K.; McVay, M.; Choe, S.; Kernytsky, A.; Gross, S.; et al. MTAP Deletions in Cancer Create Vulnerability to Targeting of the MAT2A/PRMT5/RIOK1 Axis. *Cell Reports* **2016**, *15* (3), 574-587. DOI: 10.1016/j.celrep.2016.03.043 (acccessed 2019/04/05).
(73) Shailesh, H.; Zakaria, Z. Z.; Baiocchi, R.; Sif, S. Protein arginine methyltransferase 5 (PRMT5) dysregulation in cancer. *Oncotarget* **2018**, *9* (94), 36705-36718. DOI: 10.18632/oncotarget.26404 PubMed.
(74) Stopa, N.; Krebs, J. E.; Shechter, D. The PRMT5 arginine methyltransferase: many roles in development, cancer and beyond. *Cell Mol Life Sci* **2015**, *72* (11), 2041-2059. DOI: 10.1007/s00018-015-1847-9.
(75) Teng, Y.; Girvan, A. C.; Casson, L. K.; Pierce, W. M.; Qian, M.; Thomas, S. D.; Bates, P. J. AS1411 Alters the Localization of a Complex Containing Protein Arginine Methyltransferase 5 and Nucleolin. *Cancer Research* **2007**, *67* (21), 10491. DOI: 10.1158/0008-5472.CAN-06-4206.
(76) Brehmer, D.; Beke, L.; Wu, T.; Millar, H. J.; Moy, C.; Sun, W.; Mannens, G.; Pande, V.; Boeckx, A.; van Heerde, E.; et al. Discovery and Pharmacological Characterization of JNJ-64619178, a Novel Small-Molecule Inhibitor of PRMT5 with Potent Antitumor Activity. (1538-8514 (Electronic)). From 2021 Dec.
(77) McKinney, D. A.-O.; McMillan, B. J.; Ranaghan, M. A.-O.; Moroco, J. A.-O.; Brousseau, M.; Mullin-Bernstein, Z.; O'Keefe, M.; McCarren, P.; Mesleh, M. F.; Mulvaney, K. M.; et al. Discovery of a First-in-Class Inhibitor of the PRMT5-Substrate Adaptor Interaction. (1520-4804 (Electronic)). From 2021 Aug 12.
(78) Angermayr, M.; Bandlow, W. RIO1, an extraordinary novel protein kinase. *FEBS Lett* **2002**, *524* (1-3), 31-36. DOI: 10.1016/s0014-5793(02)02993-9.
(79) Angermayr, M.; Roidl, A.; Bandlow, W. Yeast Rio1p is the founding member of a novel subfamily of protein serine kinases involved in the control of cell cycle progression. *Molecular Microbiology* **2002**, *44* (2), 309-324. DOI: 10.1046/j.1365-2958.2002.02881.x.
(80) Vanrobays, E.; Gelugne, J.-P.; Gleizes, P.-E.; Caizergues-Ferrer, M. Late Cytoplasmic Maturation of the Small Ribosomal Subunit Requires RIO Proteins in

Saccharomyces cerevisiae. *Molecular and Cellular Biology* **2003**, *23* (6), 2083-2095. DOI: 10.1128/mcb.23.6.2083-2095.2003.
(81) Vanrobays, E.; Gleizes, P.-E.; Bousquet-Antonelli, C.; Noaillac-Depeyre, J.; Caizergues-Ferrer, M.; Gélugne, J.-P. Processing of 20S pre-rRNA to 18S ribosomal RNA in yeast requires Rrp10p, an essential non-ribosomal cytoplasmic protein. *The EMBO Journal* **2001**, *20* (15), 4204-4213, https://doi.org/10.1093/emboj/20.15.4204. DOI: https://doi.org/10.1093/emboj/20.15.4204 (acccessed 2022/04/04).
(82) Widmann, B.; Wandrey, F.; Badertscher, L.; Wyler, E.; Pfannstiel, J.; Zemp, I.; Kutay, U. The kinase activity of human Rio1 is required for final steps of cytoplasmic maturation of 40S subunits. *Molecular biology of the cell* **2011**, *23*, 22-35. DOI: 10.1091/mbc.E11-07-0639.
(83) Weinberg, F.; Reischmann, N.; Fauth, L.; Taromi, S.; Mastroianni, J.; Köhler, M.; Halbach, S.; Becker, A. C.; Deng, N.; Schmitz, T.; et al. The Atypical Kinase RIOK1 Promotes Tumor Growth and Invasive Behavior. *EBioMedicine* **2017**, *20*, 79-97. DOI: https://doi.org/10.1016/j.ebiom.2017.04.015.
(84) Huang, Z.; Li, X.; Xie, T.; Gu, C.; Ni, K.; Yin, Q.; Cao, X.; Zhang, C. Elevated Expression of RIOK1 Is Correlated with Breast Cancer Hormone Receptor Status and Promotes Cancer Progression. *Cancer Research and Treatment* **2020**. DOI: 10.4143/crt.2020.187.
(85) Line, A.; Slucka, Z.; Stengrevics, A.; Silina, K.; Li, G.; Rees, R. Characterisation of tumour-associated antigens in colon cancer. *Cancer Immunology, Immunotherapy* **2002**, *51* (10), 574-582. DOI: 10.1007/s00262-002-0322-2.
(86) *SILCS--Site-Identification by Ligand Competitive Saturation*. 2022. https://silcsbio.com/platform-technology/ (accessed 2023.
(87) Kim, M. Discovery of a Potent and Selective RioK1 Inhibitor active in CRC cell lines using Structure-Based Drug Design. University of Maryland College Park, Digital Repository at the University of Maryland, 2021.
(88) Lakkaraju, S. K.; Raman, E. P.; Yu, W.; MacKerell, A. D. Sampling of Organic Solutes in Aqueous and Heterogeneous Environments Using Oscillating Excess Chemical Potentials in Grand Canonical-like Monte Carlo-Molecular Dynamics Simulations. *Journal of Chemical Theory and Computation* **2014**, *10*, 2281 - 2290.
(89) Vanommeslaeghe, K.; Hatcher E Fau - Acharya, C.; Acharya C Fau - Kundu, S.; Kundu S Fau - Zhong, S.; Zhong S Fau - Shim, J.; Shim J Fau - Darian, E.; Darian E Fau - Guvench, O.; Guvench O Fau - Lopes, P.; Lopes P Fau - Vorobyov, I.; Vorobyov I Fau - Mackerell, A. D., Jr.; et al. CHARMM general force field: A force field for drug-like molecules compatible with the CHARMM all-atom additive biological force fields. (1096-987X (Electronic)). From 2010 Mar.
(90) Yu, W.; He X Fau - Vanommeslaeghe, K.; Vanommeslaeghe K Fau - MacKerell, A. D., Jr.; MacKerell, A. D., Jr. Extension of the CHARMM General Force Field to sulfonyl-containing compounds and its utility in biomolecular simulations. (1096-987X (Electronic)). From 2012 Dec 5.
(91) Durell, S. R.; Brooks, B. R.; Ben-Naim, A. Solvent-Induced Forces between Two Hydrophilic Groups. *The Journal of Physical Chemistry* **1994**, *98*, 2198-2202.
(92) Hess, B.; Kutzner, C.; van der Spoel, D.; Lindahl, E. GROMACS 4: Algorithms for Highly Efficient, Load-Balanced, and Scalable Molecular Simulation. *Journal of Chemical Theory and Computation* **2008**, *4* (3), 435-447. DOI: 10.1021/ct700301q.

(93) Raman, E. P.; Yu W Fau - Lakkaraju, S. K.; Lakkaraju Sk Fau - MacKerell, A. D., Jr.; MacKerell, A. D., Jr. Inclusion of multiple fragment types in the site identification by ligand competitive saturation (SILCS) approach. (1549-960X (Electronic)). From 2013 Dec 23.
(94) Friesen, W. J.; Paushkin, S.; Wyce, A.; Massenet, S.; Pesiridis, G. S.; Van Duyne, G.; Rappsilber, J.; Mann, M.; Dreyfuss, G. The methylosome, a 20S complex containing JBP1 and pICln, produces dimethylarginine-modified Sm proteins. *Molecular and cellular biology* **2001**, *21* (24), 8289-8300. DOI: 10.1128/mcb.21.24.8289-8300.2001 PubMed.
(95) Antonysamy, S.; Bonday, Z.; Campbell, R. M.; Doyle, B.; Druzina, Z.; Gheyi, T.; Han, B.; Jungheim, L. N.; Qian, Y.; Rauch, C.; et al. Crystal structure of the human PRMT5:MEP50 complex. *Proceedings of the National Academy of Sciences of the United States of America* **2012**, *109* (44), 17960-17965. DOI: 10.1073/pnas.1209814109 PubMed.
(96) Sun, L.; Wang, M.; Lv, Z.; Yang, N.; Liu, Y.; Bao, S.; Gong, W.; Xu, R.-M. Structural insights into protein arginine symmetric dimethylation by PRMT5. *Proceedings of the National Academy of Sciences* **2011**, *108* (51), 20538. DOI: 10.1073/pnas.1106946108.
(97) Sayegh, J.; Clarke, S. G. Hsl7 is a substrate-specific type II protein arginine methyltransferase in yeast. *Biochem Biophys Res Commun* **2008**, *372* (4), 811-815. DOI: 10.1016/j.bbrc.2008.05.121 PubMed.
(98) Tina; Sayegh, J.; Frankel, A.; Jonathan; Miranda, M.; Clarke, S. Yeast Hsl7 (histone synthetic lethal 7) catalyses the in vitro formation of ω-NG-monomethylarginine in calf thymus histone H2A. *Biochemical Journal* **2006**, *395* (3), 563-570. DOI: 10.1042/bj20051771.
(99) Ryu, H.-Y.; Duan, R.; Ahn, S. H. Yeast symmetric arginine methyltransferase Hsl7 has a repressive role in transcription. *Research in Microbiology* **2019**, *170* (4-5), 222-229. DOI: 10.1016/j.resmic.2019.01.002.
(100) Shulewitz, M. J.; Inouye, C. J.; Thorner, J. Hsl7 Localizes to a Septin Ring and Serves as an Adapter in a Regulatory Pathway That Relieves Tyrosine Phosphorylation of Cdc28 Protein Kinase inSaccharomyces cerevisiae. *Molecular and Cellular Biology* **1999**, *19* (10), 7123. DOI: 10.1128/MCB.19.10.7123.
(101) Yamada, A.; Duffy, B.; Perry, J. A.; Kornbluth, S. DNA replication checkpoint control of Wee1 stability by vertebrate Hsl7. *Journal of Cell Biology* **2004**, *167* (5), 841-849. DOI: 10.1083/jcb.200406048 (acccessed 1/14/2021).
(102) Tewary, S. K.; Zheng, Y. G.; Ho, M.-C. Protein arginine methyltransferases: insights into the enzyme structure and mechanism at the atomic level. *Cellular and Molecular Life Sciences* **2019**, *76* (15), 2917-2932. DOI: 10.1007/s00018-019-03145-x.
(103) Cura, V.; Marechal, N.; Troffer-Charlier, N.; Strub, J. M.; Van Haren, M. J.; Martin, N. I.; Cianférani, S.; Bonnefond, L.; Cavarelli, J. Structural studies of protein arginine methyltransferase 2 reveal its interactions with potential substrates and inhibitors. *The FEBS Journal* **2017**, *284* (1), 77-96. DOI: 10.1111/febs.13953.

(104) Magni, G.; Orsomando G Fau - Raffaelli, N.; Raffaelli, N. Structural and functional properties of NAD kinase, a key enzyme in NADP biosynthesis. (1389-5575 (Print)). From 2006 Jul.
(105) Lerner, F.; Niere M Fau - Ludwig, A.; Ludwig A Fau - Ziegler, M.; Ziegler, M. Structural and functional characterization of human NAD kinase. (0006-291X (Print)). From 2001 Oct 19.
(106) Krzyzanowski, A.; Gasper, R.; Adihou, H.; Hart, P. t.; Waldmann, H. Biochemical Investigation of the Interaction of pICln, RioK1 and COPR5 with the PRMT5-MEP50 Complex. *Chembiochem : a European journal of chemical biology* **2021**, *22* (11), 1908-1914. DOI: 10.1002/cbic.202100079 PubMed.
(107) Jensen-Pergakes, K. A.-O.; Tatlock, J.; Maegley, K. A.; McAlpine, I. J.; McTigue, M.; Xie, T.; Dillon, C. A.-O.; Wang, Y.; Yamazaki, S. A.-O.; Spiegel, N.; et al. SAM-Competitive PRMT5 Inhibitor PF-06939999 Demonstrates Antitumor Activity in Splicing Dysregulated NSCLC with Decreased Liability of Drug Resistance. (1538-8514 (Electronic)). From 2022 Jan.
(108) Hanwell, M. D.; Curtis De Fau - Lonie, D. C.; Lonie Dc Fau - Vandermeersch, T.; Vandermeersch T Fau - Zurek, E.; Zurek E Fau - Hutchison, G. R.; Hutchison, G. R. Avogadro: an advanced semantic chemical editor, visualization, and analysis platform. (1758-2946 (Electronic)). From 2012 Aug 13.
(109) Rappe, A. K.; Casewit, C. J.; Colwell, K. S.; Goddard, W. A., III; Skiff, W. M. UFF, a full periodic table force field for molecular mechanics and molecular dynamics simulations. *Journal of the American Chemical Society* **1992**, *114* (25), 10024-10035. DOI: 10.1021/ja00051a040.
(110) van Zundert, G. C. P.; Rodrigues, J. P. G. L. M.; Trellet, M.; Schmitz, C.; Kastritis, P. L.; Karaca, E.; Melquiond, A. S. J.; van Dijk, M.; de Vries, S. J.; Bonvin, A. M. J. J. The HADDOCK2.2 Web Server: User-Friendly Integrative Modeling of Biomolecular Complexes. *Journal of Molecular Biology* **2016**, *428* (4), 720-725. DOI: https://doi.org/10.1016/j.jmb.2015.09.014.
(111) Honorato, R. V.; Koukos, P. I.; Jiménez-García, B.; Tsaregorodtsev, A.; Verlato, M.; Giachetti, A.; Rosato, A.; Bonvin, A. M. J. J. Structural Biology in the Clouds: The WeNMR-EOSC Ecosystem. *Frontiers in Molecular Biosciences* **2021**, *8*, Technology and Code.